UNIVERSITY OF CALIFORNIA

Los Angeles

Baryon Stopping and Charged Particle Production from Lead-Lead Collisions at 158 GeV per Nucleon

A dissertation submitted in partial satisfaction of the requirements for the degree Doctor of Philosophy in Physics

by

Milton Y Toy

1999

Contents

List of Figures

List of Tables

ACKNOWLEGEMENTS

Many thanks to the people and organizations who have given their generous support and encouragement. In particular, a special mention goes to Peter Jacobs, who has acted as my advisor and supervised my work here at Lawrence Berkeley National Laboratory over the years.

From a very long list:

At UCLA: Chuck Whitten, George Igo, Huan Huang, Vahe Ghazikhanian, Steve Trentalange, Chris Dulya, Brian Derro, and Brian Lasiuk.

My many friends and colleagues from NA49, including the spokespersons of the experiment, Reinhard Stock and Peter Seyboth.

From LBNL, people from the distant past to the present in no particular order: Peter Jacobs (again), Art Poskanzer, Hans Georg Ritter, Grazyna Odyniec, Jim Carroll, Nu Xu, Richard Morse, Matt Bloomer, Peter Jones, Detlef Irmscher, Heinrich Rudolph, Thomas Wienold, Isaac Huang, Fuqiang Wang, Dave Hardtke, Raimond Snellings, and Glenn Cooper.

And to those who I haven't mentioned, you are in my thoughts.

Berkeley, CA
1999

ABSTRACT OF THE DISSERTATION

Baryon Stopping and Charged Particle Production

from Lead-Lead Collisions at 158 GeV per Nucleon

by

Milton Y Toy

Doctor of Philosophy in Physics

University of California, Los Angeles, 1999

Professor G. Igo, Co-Chair

Professor C. Whitten, Co-Chair

Net proton (proton minus antiproton) and negative charge hadron spectra (h^-) from central Pb+Pb collisions at 158 GeV per nucleon at the CERN Super Proton Synchrotron were measured and compared to spectra from central collisions of the lighter S+S system. Net baryon distributions were derived from those of net protons and net lambdas. Stopping, or rapidity shift with respect to the beam, of net protons and net baryons increase with system size. The mean transverse momentum $\langle p_T \rangle$ of net protons also increase with system size. The h^- rapidity density scales with the number of participant nucleons for nuclear collisions, whereas their $\langle p_T \rangle$ is independent of system size. The $\langle p_T \rangle$ dependence upon particle mass and system size is consistent with larger transverse flow velocity at midrapidity for central collisions of Pb+Pb compared to that of S+S.

Chapter 1

Introduction

1.1 The Quark-Gluon Plasma

The existence of quark substructure in hadronic matter was experimentally verified several decades ago through evidence from deep inelastic scattering of electrons off nucleons [1]. However, quarks have not been observed outside of the confines of hadronic particles. In the gauge theory of strongly interacting matter, Quantum Chromodynamics (QCD), the energy needed to separate two quarks increases with distance. The energy put into pushing a single quark (q) out of a hadron will eventually create a new quark-antiquark ($q\bar{q}$) pair rather than freeing the bound quark.

The strong interaction is mediated by gluons that carry the color quantum number. At a short distance, which corresponds to high q^2 momentum transfer, the interaction between two quarks is calculable with QCD by a perturbative method because an expansion in the coupling constant α_s is dominated by a leading term that represents the primary process of a single gluon exchange. In collisions of hadrons, soft interactions at low q^2 have higher cross sections and are more common than the rare high q^2 transfer, but cannot be calculated by perturbative means.

Lattice QCD, a computational technique that places quarks on a lattice and simulates their interactions, is the best theoretical means to study hadronic properties such as mass and quark confinement that are rooted in soft processes [2]. One prediction from such calculations is that at a sufficiently high temperature or density of matter, hadronic matter undergoes a phase transistion and melts into a deconfined state called the quark gluon plasma (QGP) [3]. Lattice QCD also gives indications that chiral symmetry may be restored for the light (u, d) quarks under these conditions [4].

Lattice QCD predicts that in a system with two quark flavors, the transition to a QGP occurs at a critical temperature $T_c \sim 150$ MeV (10^{12} K). Not coincidentally, the scale parameter Λ of QCD at an asymptotically large momentum transfer, where quarks are quasi-free, has the same order of magnitude as T_c. If the system has a finite baryon density, then the transition occurs when the baryochemical potential μ_B is greater than the nucleon mass. The order of the transition is still an open

question. A first order transition is marked by an apparent increase in latent heat. It was proposed by van Hove [5] that for an equilibrated system, an increase of entropy can result in a sharp rise in the number of observed particles without a corresponding increase in the mean transverse momentum of particles. This effect has not yet been seen in experimental data.

A naïve, but instructive, model of a deconfined state is based on the scenario where hadronic matter is compressed or heated to a point where the interparticle spacings are smaller than hadronic radii. The high density of quarks results in a Debye-like color screening for any single quark from long distance interactions with other quarks. Using the charge radius of hadrons, the critical temperature of a thermalized fermion gas of pions is 170 MeV. For a system of nucleons, the transition point occurs when the baryon density is at least three times that of normal nuclear matter ($\rho_N = 0.17$ nucleons/fm^3).

Far from being an academic novelty, a QGP may have a place in the universe. It is thought that at around 10^{-6} seconds after the Big Bang, before the universe had expanded and cooled enough for the formation of hadronic matter that exists today, the dominant state of matter was a quark gluon plasma [6]. It has been proposed that at the center of some neutron stars, the extreme gravitational pressure may result in a QGP core that affects their rotational behavior, which can then be observed by radio astronomy [7].

Even without a QGP, the properties of dense and highly energetic matter show new and interesting phenomena. Hadronic masses and interaction cross sections may be modified from those observed in smaller, simpler hadronic systems [8]. Collective behavior such as particle and energy flow has been observed [9, 10]. The current state of experimental and theoretical research on the properties of "quark matter" and the search for the QGP can be found in the proceedings from several recent conferences [11, 12, 13].

1.2 Nucleus+Nucleus Collisions

A state of matter with the high energy density favorable for the creation of a quark-gluon plasma is studied in the laboratory with high energy nucleus+nucleus (A+A) collisions. Inelastic hadronic collisions dominate the reaction and the significant energy loss by the incoming nuclear matter is transformed to new degrees of freedom.

Microscopically, the nucleons interact, lose energy, and fragment; their remnants and newly created particles reinteract. Leptons pairs and photons are produced throughout the reaction and escape without reinteracting with the surrounding matter because of the small electroweak cross section. As this occurs, the system expands and the energy density drops. Whether thermal or chemical equilibration is achieved is an still open question. Highly energetic particles can decouple from the system while the system is still evolving. The hadronization process when the system freezes out is not understood, and it may not be possible to experimentally study freezeout

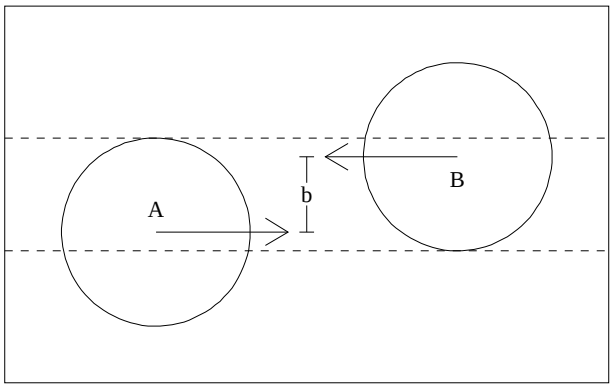

Figure 1.1: A drawing of nuclei A and B colliding with at an impact parameter b. The maximum value of b is the sum of the nuclear radii. The dashed lines indicate the region of overlap between the two nuclei. For simplicity, the nuclei are drawn in the center-of-mass frame as hard spheres with no Lorentz contraction.

in detail [14].

1.2.1 The Role of System Size and Energy

There are two controllable features in a laboratory experiment: the amount of interacting nuclear matter, or system size, and the system energy, as determined by the energy in the center-of-mass frame. System size is determined by the atomic number of the colliding nuclei and the centrality of the collision. Figure 1.1 contains a drawing that defines impact parameter b. The total system energy is determined by the momenta of the nuclei before the collision and the system size.

It is preferable to use the heaviest nuclei available in order to maximize the initial size of the system and to reduce surface effects. The surface to volume ratio of a nucleus decreases with growing atomic number. The number of nucleons that are contained within the common overlapping region[1] of the two nuclei and interact inelastically is called the number of participants, which is a measure of the system size. Those nucleons that do not participate in the collision continue along the initial beam direction and are called spectators. Note that while a central collision of light nuclei and a non-central collision of heavy nuclei may have the same number of participants, the geometrical shape of the interaction region is not the same. The effective nuclear thickness that each nucleon encounters is not the same in these two cases.

A list of the heaviest beam nuclei available for experiment from current and future high energy particle accelerators at Brookhaven National Laboratory (BNL) and the

[1] This quantity depends on the nuclear model used for the calculation. Typically, a Woods-Saxon density distribution is used.

Accelerator Facility	Heaviest Beam Nucleus	Beam Energy (GeV/N)	N+N $\sqrt{s}$ (GeV/N)	Beam-Target Rapidity Gap
AGS (BNL)	Au	$\sim$ 10–14	~ 5	~ 3
SPS (CERN)	Pb	158	17	5.8
RHIC (BNL)	Au	100	200	11
LHC (CERN)	Pb	~ 3000	~ 6000	17

Table 1.1: High energy, heavy-ion beams available from existing (AGS, SPS) and future (RHIC, LHC) particle accelerators. Beam energy and nucleon+nucleon $c.m.$ energy $\sqrt{s}$ are given in units of GeV per nucleon.

European Particle Physics Laboratory (CERN) is given in Table 1.1. Lighter nuclei are also available at similar energies. Increasing system energy means increasing the available energy for particle production. With this comes a greater Lorentz-invariant beam-target rapidity[2] gap, which means that more phase space is kinematically available.

The heavy-ion acclerators under operation today deliver beams for collisions with a fixed target. The new accelerators being built will collide counter circulating beams together at a much higher center-of-mass ($c.m.$) energy ($\sqrt{s}$) per nucleon-nucleon pair at a given beam energy.

1.2.2 Experimental Search for a QGP

Nucleus+nucleus collisions are studied in the laboratory through measurements of the final state particles. The relationship between $\sqrt{s}$ and the midrapidity rapidity density of particles per event (dn/dy_{cm}) from proton+proton collisions was extrapolated to central nucleus+nucleus collisions by Satz [15] as

$$\frac{dn}{dy} = 0.8\mathrm{A}^{\alpha} \ln \sqrt{\mathrm{s}} \tag{1.1}$$

where $\alpha \geq 1.1$. This formula predicts a dn/dy of 480 from Au+Au collisions at the AGS and 790 from Pb+Pb collisions at the SPS. These numbers roughly agree with what has been seen by experiment [16, 17].

Because of the large number of participants in a central A+A collision, there will be many different interactions occuring simultaneously that contribute to particle production. In the past, it was hoped that there would exist a definitive signal to mark the creation of a QGP, such as a sharp increase in particle multiplicity as a

[2] In this work, the phase space variables used in addition to three-momentum (p_x, p_y, p_z) are rapidity y and transverse momentum p_T. The definitions of these variables are given in Appendix A.

function of transverse energy. For some time now, it has been realized that from the available data, there are ambiguities of what constitues a QGP "signature" and what observables can be explained by known phenomena [18]. Among the proposed signatures that have been observed by experiment are enhanced production of strangeness [19, 20, 21] and the supression of observed J/ψ mesons [22] relative to a superposition of nucleon+nucleon collisions. The current belief is that a careful examination of many different observables is necessary in order to discern whether or not a QGP has been formed.

In addition to the observables already mentioned, there are a multitude of other experimental signals that reflect some aspect of the system's dynamics. To mention but a few, the space-time evolution of the system is studied through an interferometry technique using particle momentum correlations [23]. Leptons are produced at every stage of the system's evolution and can escape out of the system cleanly because they interact only through the electroweak force [24]. A new area of study is based on the characteristics of individual collisions, called event-by-event physics (EBE), which is feasible because of the large particle multiplicity from each event. The focus has been on particle momentum distribution fluctuations [25] and the search for a disordered chiral condensate manifested through fluctuations in charged and neutral pion multiplicities [26].

For this work, data taken by the NA49 experiment at the CERN-SPS from central ($b < 5$ fm) Pb+Pb collisions were analyzed to create inclusive, event-averaged charged particle spectra for the study of baryon stopping and the production of negative charge hadrons. Baryon stopping is a measure of the transport of baryon number from the nuclei before the collision to the final state net baryons $(B-\bar{B})$[3], which is closely related to energy loss. The negative charge hadrons (h^-) are a measure of the total particle production. The transverse momentum spectra of net protons and negative charge hadrons will be examined in the context of a collective transverse radial flow of hadrons [27, 28]. The results presented here have been published in reference [16].

Baryon stopping is measured through the rapidity distribution at freezeout and is related to the spatial baryon density. In order to determine baryon density, information about the space-time evolution of the system is also needed, but this discussion is beyond the scope of this work. The baryon phase space density plays a role in shaping the hadrochemistry of the system. Simply put, the number of light (u,d) quarks in the system relative to the produced strange quark pairs ($s\bar{s}$) has an effect on the number of strange hadrons formed at freezeout. If the system has a high density of light quarks and the Fermi level of the light quarks is above twice the s quark mass, then by the Pauli principle, s-$\bar{s}$ production may be favored over an excitation of a light quark.

Baryon stopping and negative hadron production are not viewed now as potential

[3] Net baryons are baryons minus antibaryons. For an inclusive, event-averaged phase space distribution, the contribution from baryon-antibaryon pair production cancels out.

signatures of QGP formation at CERN-SPS energies, but rather as indicators of the colliding system's conditions. The data will be compared to existing data from lighter systems at a similar energy per participant nucleon. Data of S+S collisions at 200 GeV per nucleon from the NA35 experiment at CERN [29, 30, 31, 32] will serve as the main points of reference. A further discussion on baryon stopping and h^- production will follow in Section 1.3.

There are two complementary approaches towards interpreting the data. One is phenomenological and its goal is to find a change in the observables at some system size and energy beyond what is expected from a superposition of elementary hadronic interactions, thus indicating a phase transition. The other is to compare the data to predictions made with models of A+A collisions. These models are often based on interactions of simpler hadron+hadron systems as well as additional processes that may result in a QGP. (Section 1.4 contains descriptions of various models.)

1.2.3 The NA49 Experiment

The Super Proton Synchrotron (SPS) at CERN delivers a beam of ^{208}Pb at 158 GeV per nucleon that is guided into a fixed nuclear target. If a lead target is used, then the total system energy is $\sqrt{s} = 3.6$ TeV.

Before the first Pb beam was delivered in 1994, ^{16}O and ^{32}S at 200 GeV per nucleon[4] were the available heavy-ion beams in the late 1980's to early 1990's. A central S+S collision produces around 10 charged and neutral hadrons per nucleon participant pair [29]. An extrapolation to a central Pb+Pb collision based on atomic number scaling indicates that on the order of 2×10^3 particles should be produced.

This is an unprecedented particle multiplicity in nuclear and particle physics, and imposes new technical challenges for experiments. The NA49 experiment (Chapter 2) was designed to detect a large fraction of all charged hadrons in the phase space region around midrapidity and forward of midrapidity.

1.3 Baryon Stopping and Negative Charge Hadron Production

1.3.1 Proton+Proton Collisions

The significance of baryon stopping can be better understood after a brief introduction to the phenomenon of the leading proton from proton+proton collisions. A high energy $p+p$ collision at CERN-SPS energies (where a proton with 100 to 450 GeV of energy strikes a stationary proton in the laboratory frame) has two typical features: a fast leading baryon that carries away the conserved net baryon number, and the

[4] The charge to mass ratio of a beam projectile affects the energy to which it can be accelerated.

appearance of a few produced hadrons that are mostly pions. While the leading baryon may not be a proton because the interaction may be isospin or flavor changing, the difference in energy between the projectile proton and leading baryon is balanced by particle production and the momentum of the struck target baryon. Also, while baryons and antibaryons may be produced in pairs, it is the single fastest baryon that is conceptually associated with the projectile proton.

The focus will be on protons because there are comprehensive data of leading proton distributions. The leading proton rapidity distribution from $p+p$ collisions at SPS energies falls off from beam rapidity as $\sim \exp^{\Delta y}$ ($\Delta y = y - y_{beam} < 0$) [33, 34].

The collision imparts transverse momentum to the proton. The momentum transfer is greatest around midrapidity, where the projectile can be thought of as being fully stopped. From a beam energy of 200 GeV in the laboratory, or $\sqrt{s}$ of around 18 GeV, the mean transverse momentum ($\langle p_T \rangle$) of a midrapidity proton is around 450 MeV [35]. In the *c.m.* frame, this proton has no longitudinal momentum, but retains 10% of the beam energy just with its mass and only 1% by its transverse motion.

While the relative number of pions, kaons, and other produced particles may vary depending on the colliding system or $\sqrt{s}$, overall multiparticle production can be estimated from the number of negative charge hadrons. Charged particles are normally easier to measure by most experimental techniques and the positive charge particles may include two protons because of baryon number conservation.

The total h^- multiplicity from $p + p$ collisions at SPS energies is around 3, with a weak energy dependence that has a $ln(s)$ leading term [36]. It has been seen that an increase in produced particle multiplicity or system energy is accompanied by a slight increase in $\langle p_T \rangle$ [35]. For an increase of $\sqrt{s}$ by a factor of 10, the $\langle p_T \rangle$ of pions increases by about 10%.

1.3.2 Proton+Nucleus Collisions

When the target is a nucleus, multiple interactions will occur within the nucleus. Baryon stopping takes on additional meaning here because the projectile has the chance to interact multiple times, greatly increasing its energy loss. As the proton strikes the nucleus, secondary particles are produced. These particles reinteract, creating more particles, and a cascade is formed. Recent p+A collision experiments date from the 1980s and typically use beams at an energy of 100 to 200 GeV colliding into fixed nuclear targets [33, 37, 38, 39, 40].

The centrality of the collision plays an important role in determining baryon stopping. A proton that bores through the center of a nucleus encounters much more nuclear material than one that only clips the edge. The average number of scatterings $\bar{\nu}$ that an incident proton undergoes is defined as the ratio of inelastic interaction cross sections

$$\bar{\nu} = A\frac{\sigma_{pp}}{\sigma_{pA}} \tag{1.2}$$

where A is the atomic number of the nucleus [38]. Ignoring any trigger biases, the

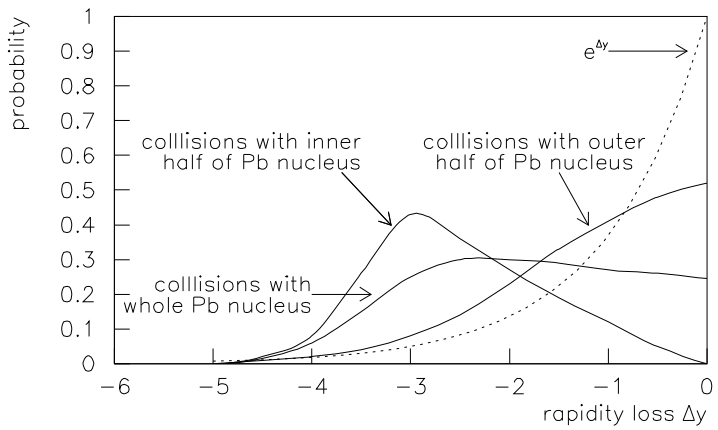

Figure 1.2: A schematic drawing from reference [42] of the rapidity loss Δy probability distribution of leading protons from $p+p$ ($\exp(\Delta y)$) and p+Pb collisions when the incident proton strikes the inner half, outer half, and entire Pb nucleus.

p+A cross section is weighted by impact parameter as b^2 ($d\sigma \sim bdb$). The number of scatterings has a target dependence that is proportional to $A^{1/3}$.

For a single event, the low momentum protons ($p < 1$ GeV) that are knocked out of the nucleus have been used to determine the number of collisions through the relationship $\bar{\nu_p} \propto \sqrt{n_p}$. The number of produced particles has been observed to increase linearly with $\bar{\nu_p}$, which is consistent with "wounded nucleon" scaling [41]. To compare their p+A results with $p+p$ data, DeMarzo *et al.* [38] divided their data into three sets based on the leading proton rapidity rather than n_p. For the set of events where the proton is found near beam rapidity, also called the beam fragmentation region, the h^- multiplicity per collision is lower than that from $p+p$. Those events with the largest projectile rapidity losses had an h^- yield per collision greater than that from $p+p$.

Busza and Goldhaber [42] compiled p+A data from Barton *et al.* [33] and calculated the probability distribution of the leading proton rapidity loss when the proton strikes either the inner half or outer half of a target Pb nucleus. Figure 1.2 shows a schematic drawing based on their work. As expected, the typical rapidity loss of the leading proton is much greater in a p+Pb collision than in a $p+p$ collision. It is clear that the amount of target matter that the projectile encounters has a dramatic effect on its stopping.

1.3.3 Nucleus+Nucleus Collisions

As was shown in Figure 1.2, the centrality of a p+Pb collision plays a strong role in baryon stopping. The participants in a central Pb+Pb collision can encounter a significant amount of nuclear matter. Figure 1.3 is a sketch of the net baryon rapidity distribution before and after the collision. Full stopping occurs when the nuclei are

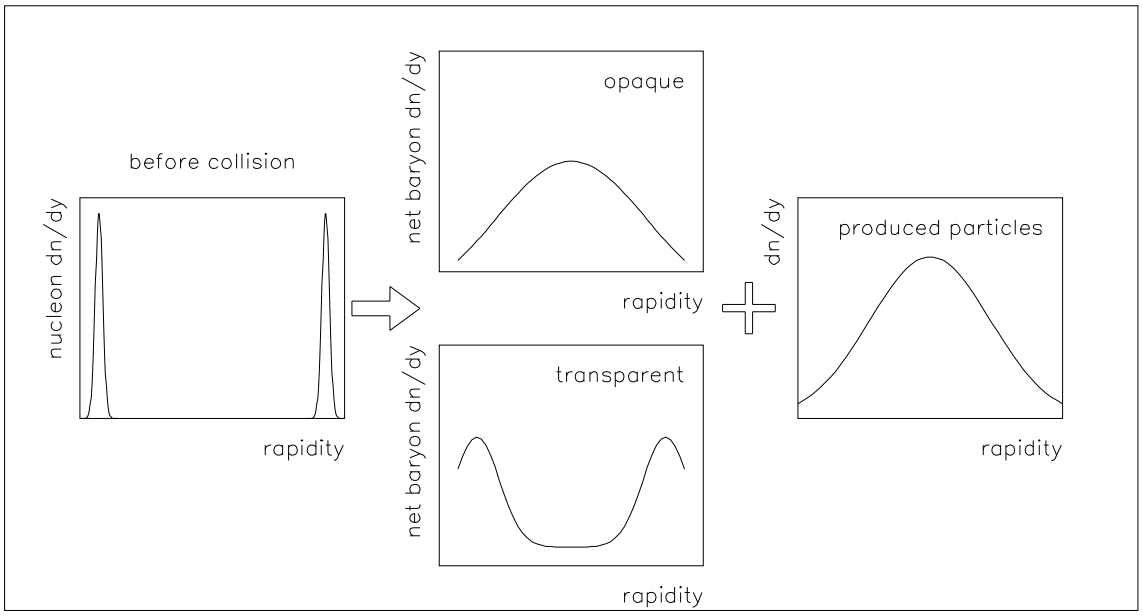

Figure 1.3: A drawing of the rapidity distribution of net baryons before and after the collision. The transport of baryon number from the nucleons at beam and target rapidities before the collision to the net baryon distribution after the collision is the baryon stopping of the system. Accompanying the net baryon rapidity shift and energy loss is the creation of new particles.

opaque to each other and baryons are piled up around midrapidity. Transparency is the opposite case, where the midrapidity baryon density is low because the baryons are shifted by only a small fraction of the beam-target rapidity gap. However, a clear observation of a fully stopped system may not be possible because the subsequent longitudial expansion of the system causes in a broadening of the final state particle rapidity distributions [43].

The effect of increasing beam energy on proton distributions can be seen in Figure 1.4. Data of protons and net protons ($p-\bar{p}$) from the Bevalac[5] [44], AGS [17], and SPS [29] show that as the rapidity gap between the beam and target increases, the available phase space is filled in by the protons. Therefore, the overall scale of the proton rapidity density is set by the system energy. It is expected that the baryon rapidity distribution is not strongly influenced by the amount of interacting nuclear matter at SPS energies because of longitudinal expansion and so it is unlikely that protons from a heavy system such as Pb+Pb will be piled up dramatically around midrapidity, in constrast to the relatively wide distribution from the lighter S+S system.

[5] Approximately half of the protons from Bevalac energy ($\sim$ 1 GeV) collisions are found in heavier fragments such as deuterons and tritons. These bound protons are properly included in the rapidity distribution.

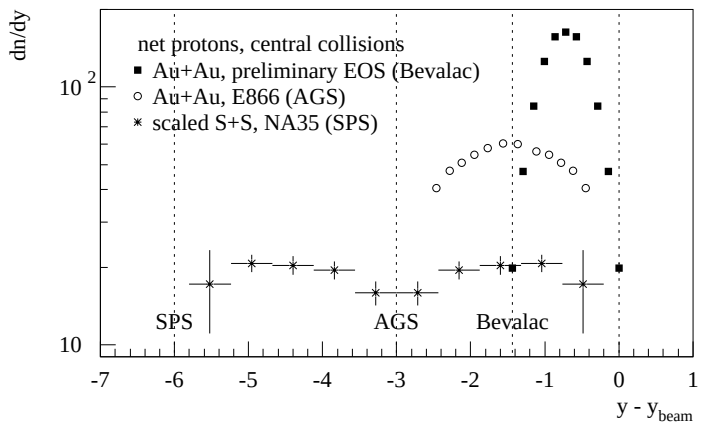

Figure 1.4: Proton distributions relative to beam rapidity in the laboratory frame. The data are from Au+Au collisions at the Bevelac (y_b = 1.5) and AGS (y_b = 3), and S+S collisions from the SPS (y_b = 6). The SPS data are net protons, $p-\bar{p}$, and are scaled by the ratio of protons in gold to that in sulfur (79/16). The dashed lines show the phase space limits for the three systems.

There is an unanswered question of whether the initial collisions, as the beam nucleus first penetrates the target, alters the target matter for the following projectile nucleons. The intranuclear cascade of particles in a p+A collision always encounters cold, unexcited nuclear matter, but this is not the case in an A+A collision.

Relative to nucleon+nucleon collisions, there are more negative charge hadrons created per participant baryon in central S+S collisions at CERN-SPS energies [29]. This is not surprising because of the multiple collisions that occur. However, from central S+S, S+Au, and O+Au collisions, baryon stopping increases with the amount of interacting nuclear matter, but the number of h^- per participant is nearly the same [29]. The projectile nucleons lose the bulk of their energy after losing just one unit of rapidity. Further stopping may not result in greater particle production, but can influence the transverse momentum spectra of particles.

From A+A data at the lower BNL-AGS energies, it has been noted that the p_T spectra shapes follow a mass-based systematic trend that is consistent with a radial transverse flow velocity that is common for all particles [45, 46]. The mean p_T of protons and pions from p+p collisions are similar. From A+A collisions, the mean p_T difference between pions and protons is larger than that from $p+p$ collisions, and this difference grows for larger system sizes. S+S data from the CERN-SPS have been shown to be consistent with this picture of transverse flow as well [27], and it is expected that this behavior will be evident in the Pb+Pb data.

1.4 Models of A+A Collisions

1.4.1 Microscopic Models

Microscopic non-equilibrium models attempt to predict the interactions that occur during the collision and the formation of final state particles. Nearly every existing model starts with a colliding system of partons that forms and then fragments color strings based on formulations similar to the Lund string dynamics model [47]. Additional features incorporated into these models include multiple interactions and the creation and decay of resonances.

The models that will be used in this work are VENUS version 4.12 [48] and RQMD version 2.03 [49]. These two models have open source code and are widely used. VENUS features string breaking based on the Dual Parton Model (DPM) [50] with minimal final state interactions. RQMD uses a similar combination of color string formation and hadronic resonances from elementary collisions, but in contrast to VENUS incorporates a classical propagation of particles. Multiple scattering and mean-field interactions are also important features of this model.

1.4.2 Thermal Models with Flow

Unlike the microscopic models, thermal models are built upon arguments that the system is in local equilibrium and behaves as a hydrodynamic fluid. System parameters (temperature, chemical potentials, flow velocities, and pressure) are extracted from single particle spectra and correlation data. A simple isotropic thermal source cannot accurately describe the data from S+S collisions from the CERN-SPS [32], and it is not expected that this model will have any better success with data from the Pb+Pb system. It has been observed that the shapes of transverse momentum distributions from A+A collisions are consistent with the existence of a common radial transverse flow velocity for all particles [45, 46].

Heinz *et al.* developed a thermal hydrodynamic model with transverse flow that was able to reproduce the shape of the p_T spectra from S+S collisions [27, 51, 52]. Resonances play an important role in shaping the p_T spectra, especially below $p_T < 200$ MeV. The latest refinements to this idea are to incorporate additional information of the source size from momentum correlation measurements and the longitudinal expansion of the system from rapidity distributions [28, 53, 54]. The result is a multiparameter formula that is used to fit many different particle distributions simultaneously. NA49 data from central Pb+Pb collisions have been studied in this context and show a system temperature of 120±12 MeV and a flow velocity of $\beta = 0.55$ [55].

1.4.3 Bjorken's Boost Invariant Model

Bjorken's model [56] deserves mention because its simple and elegant formulation is an appealing view of the space-time evolution of the system around midrapid-

ity. However, no current experimental result has yet met its conditions. The model assumes that matter is free-streaming and equilibrated, and that there is a central plateau region in the particle rapidity distribution. The evolution of this energetic fluid looks the same in all reference frames near the center-of-mass. The longitudinal and transverse expansion of the system are decoupled.

The model's predictions include an estimate of the central energy density

$$\epsilon \approx \frac{\mathcal{N}}{\mathcal{A}} \frac{d\langle E \rangle}{dy} \frac{1}{2\tau}. \tag{1.3}$$

The effective number of incident nucleons per unit cross-sectional area $\mathcal{N}/\mathcal{A}$ is based on the radius and atomic number of the nuclei. The energy density in rapidity can be determined from the particle rapidity density dn/dy and mean transverse momentum. The least well determined part of this formula is the formation time of the system τ, which is commonly set to 1 fm/c.

Another characteristic of the central region is a transverse momentum distribution that is independent of rapidity. If the system is equilibrated, this means that the temperature is constant across the central region.

The net baryon density in the central region is assumed to be negligible. A very large rapidity gap must exist between the projectile and target in order for the conditions of the model to be met. Given that the typical baryon rapidity loss is 2 to 3 units of rapidity from a high beam rapidity ($y_{beam} > 6$), the Bjorken model may be applicable only to the data that will come from the RHIC and LHC experiments.

1.4.4 Baryon Stopping

Unlike other observables from A+A collisions, baryon stopping has not been predicted by theory with good success [57]. Lately, interest has been renewed in an old model of the baryon by Rossi and Veneziano [58]. They proposed that a baryon is constructed of three valence quarks connected by color strings that meet at a common point called a junction. Recent theoretical work have used new mechanisms of baryon stopping incorporating this junction model and show good promise [59, 60, 61, 62].

Chapter 2

The NA49 Experiment

2.1 Introduction

2.1.1 Design Considerations and the TPC

The NA49 experiment [63] was designed to meet the ambitious goal of simultaneously measuring most of the 10^3 charged hadrons from a central Pb+Pb collision at 158 GeV per nucleon. Time projection chambers (TPCs) [64] (Section 2.3.1) were selected to be the primary charged particle tracking detectors because large acceptance detectors were required and because of the demands imposed by the high particle multiplicity environment.

The TPC essentially consists of a volume of gas in a weak electric field (typically up to a few hundred V/cm). Charged particles that pass through the detector ionize gas atoms and leave behind tracks of ionization in three dimensions that are transported by the electric drift field to a multiwire proportional chamber (MWPC) [65] for readout by a segmented cathode pad plane. The TPC provides particle identification through the measurement of specific energy loss (Section 2.3.2) combined with the momentum measurement. The typical energy losses do not correspond to momentum transfers that are large enough to cause any significant deflection or slowing of particles at relativistic velocities.

The large number of charged particles that emerges from a central Pb+Pb collision can produce a substantial background from secondary interactions with the detector material. Ideally, the detector should be built from as little material as possible in the path of the particles to minimize the background. This is possible with TPCs, which can be made of a light frame with thin windows to hold in the fill gas.

The two track spatial resolution requirement of the NA49 TPCs is driven by two particle momentum correlation measurements. The detector must be able to simultaneously measure two particles with a small momentum difference down to $\Delta p_T \sim 10$ MeV. For single particle spectra, two track resolution is not as important; losses due to merged particle tracks from heavy ion collisions for the NA49 experiment are relatively small (around a few percent compared to the total number of particles)

and a correction for this effect can be reliably calculated (Section 3.3.3).

A large detector with a large phase space coverage, or acceptance, is not needed to comprehensively measure one and two particle event-inclusive charged particle spectra. A small angle spectrometer can be moved around so that different regions of phase space can be covered. Other data analyses besides one and two particle spectra do demand a design with large acceptance. Neutral strange hadrons are found through the detection of their charged decay daughter particles. The detector should be positioned to measure both daughter tracks that point back to a decay vertex that is distinguishable from the primary vertex in the target. The wide range of possible decay vertex positions and trajectories of the daughter particles can only be covered with a large size detector located near the target. For an event shape or event-by-event analysis, acceptance effects need to be ruled out as the cause of any observed signal.

All of these issues can be addressed with TPCs. The TPC can be designed as a large solid angle detector with excellent pattern recognition ability for tracking with particle identification capability. The readout of the TPC can be highly segmented to give good spatial tracking resolution. A constraint imposed by the TPC design is a substantial dead time due to the potentially large event size, signal readout and digitization time, and bandwidth limitations that ultimately restricts the data taking rate.

Because of the fixed target geometry of particle collisions at the CERN-SPS, particles are emitted at very small angles relative to the beam because of the momentum of the system's center of mass. The experimental design must include a strong magnetic field to spread the charged particles apart for detection and also to provide momentum analysis. Particles with transverse momentum less than the p_T kick of the magnetic field will always be deflected to one side of the beam depending upon charge. The small deflection and therefore small track angle of high momentum particles means that detectors have to be placed close to the beam axis and far enough downstream of the target so that the particles can spread apart sufficiently to be measured separately. Lower momentum particles below midrapidity are substantially deflected and can be measured with detectors closer to the target.

2.1.2 Experimental Apparatus

As shown in Figure 2.1, the apparatus consists of two dipole magnets and several subdetector systems, most notably four time projection chambers for charged particle tracking, several time of flight detectors (TOF), and two calorimeters that measure both hadronic and electromagnetic energy. The laboratory coordinate system used by NA49 has the $\hat{z}$ axis coinciding with the beam axis and pointing downstream. Upwards vertically is the $\hat{y}$ direction, and $\hat{x}$ points to the left of $\hat{z}$.

The two dipole magnets VM1 and VM2 separate the charged particles and provide momentum analysis through the deflection of the particles in the field. The magnets

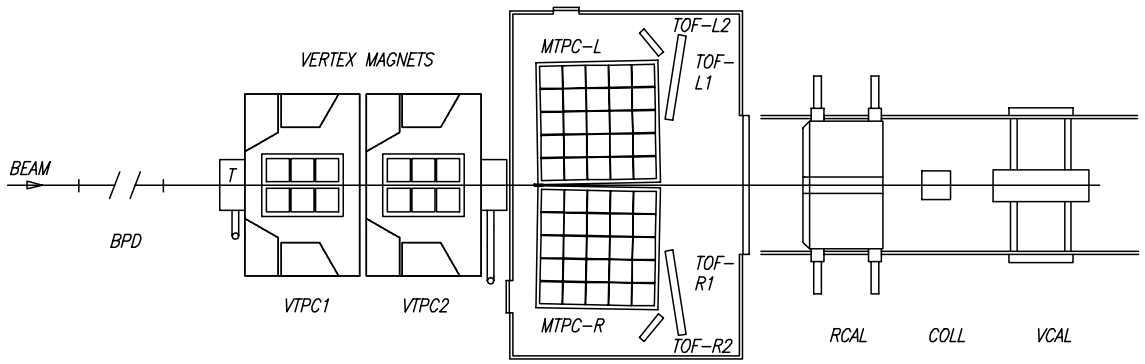

Figure 2.1: A schematic diagram of the NA49 experiment. The beam comes in from the left and passes through two beam position detectors (BPD) before striking the target T. The primary detectors are time projection chambers (TPC) and are supplemented by time of flight detectors (TOF). Two TPCs are placed between the poles of the vertex magnets (VM). The segmented ring calorimeter (RCAL) is used only in special experimental runs, while the veto calorimeter (VCAL) is used in the trigger. A collimator (COLL) shields the VCAL from particles that are outside of $\sim 0.3°$ of the beam.

are operated with their fields parallel. The standard setting (STD) has field strengths of 1.5 T and 1.1 T for VM1 and VM2 respectively, for a total bending power of about 9 T-m. This is equivalent to a p_T kick of 2.5 GeV/c. In the case of the $STD+$ setting, the field points in the $-\hat{y}$ direction and therefore positive charge particles are deflected to the left ($+\hat{x}$).

The particles passing through each Main TPC (MTPC) are predominantly of a single charge sign because of the p_T kick from the magnets. MTPC tracks are reconstructed as straight lines, in contrast to the helical tracks found in the Vertex TPCs (VTPC) that are located in the magnetic field. Momentum can be determined from the curvature of VTPC tracks, whereas in the MTPC an iterative procedure is performed that projects tracks back to the target using a map of the magnetic field and the constraint of a starting point near the target. Nearly 80% of all charged particles from hadron+hadron or nucleus+nucleus collisions at SPS energies enter at least one of the TPCs. The approximate rapidity coverage of the VTPC for pions is around $1 < y < 3$ while the MTPC has coverage forward of midrapidity. Additional details and performance figures are given in Section 2.3.1.

The combination of the large size and fine pad plane segmentation (Section 2.3.1) of the TPCs results in an extremely large number of readout channels (over 182,000) and an uncompressed event size approaching 100 MB. Specialized readout electronics and data aquisition (Section 2.3.1) were designed to make the TPC application feasible. Figure 2.2 shows the NA49 TPC readout of a central Pb+Pb event.

A midrapidity particle has a specific energy loss near minimum ionizing, requiring supplementary information for particle identification by TOF detectors placed

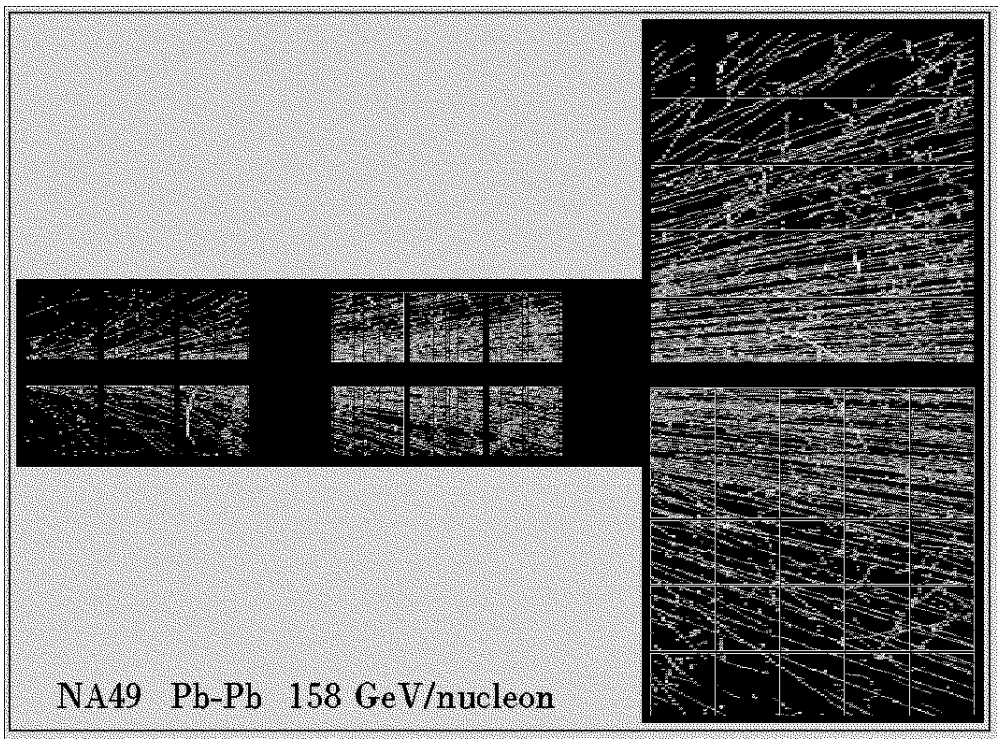

Figure 2.2: Actual NA49 TPC readout of a central Pb+Pb collision event as viewed from above. The data shown are from a 7 mm slice around the beam plane.

behind the MTPC. The TOF walls are made of plastic scintillator slats connected to phototubes. Given the TOF momentum acceptance and the flight path of around 14 m from the target, a timing resolution of 60 to 80 ps is needed for an accurate determination of particle mass from the time of flight (which is related to velocity) and the MTPC track momentum.

The ^{208}Pb beam at 158 GeV/nucleon from the CERN-SPS accelerator is identified and counted by quartz wafer Cerenkov detectors. The beam position is found with small $ArCH_4$ filled multiwire proportional chambers. The beam comes from the SPS in bunches, or "spills", of around 10^{10} ions spread over 5 seconds within the total machine cycle of 20 seconds. The CERN-SPS heavy-ion running period is typically four to six weeks a year. Because of the statistical needs for the event-by-event analysis program, a goal of accumulating a data set of 10^6 events per year was set. In contrast, only 10^5 events are needed for most inclusive single particle measurements.

The beam intensity is limited upstream of NA49 to 10^5 ions per spill because of the relatively slow data-taking rate due to the TPC dead time and data aquisition speed limitations. The fixed target is a natural Pb foil of thickness 224 mg/cm^2 that has an interaction length of 0.5%. For each beam cycle, 20 to 25 events are recorded.

Besides limiting the event rate, the thin target reduces the level of e^+e^- pairs from π^0 conversions. The collision vertex position in the plane transverse to the beam axis can be determined to a precision of hundreds of microns by virtue of the sheer number of TPC tracks that point back to the interaction point.

The Ring calorimeter (RCAL) was used for a dedicated transverse energy measurement [66], but not for normal operation. The Veto calorimeter measures the forward going energy that is mainly spectator matter and is used to select events based on collision centrality (Section 2.2).

The position of the detectors and beam line are determined through a combination of optical surveys, field-off data from multitarget heavy-ion collisions, and the "halo" of muons from the accelerator. The optical survey fixes the external TPC positions down to 200 μm. The internal alignment of the TPC readout is tested with the straight line tracks in all TPCs from field-off runs of multiple targets set along the beam line and from muons created upstream of the apparatus that travel parallel to the beam line. Track distortions due to misalignments can be corrected offline to a precision better than 200 μm. The magnetic field is measured with Hall probes over a three dimensional grid with a spacing of 4 cm in each direction. A calculation of the field based on the magnet material and configuration produced a field map that agreed with the measured field to within 0.5%.

Because the VTPCs are placed within the magnetic fields, the combination of the electric drift field and the fringe components of the magnetic field create an $E \times B$ deflection of the ionization that causes track distortions of up to several centimeters at the edges of the detectors. A 4 mJ pulsed Nd-YAG laser is used to create straight tracks in the TPCs when the magnetic field is on.

The analysis presented in this work comes from data taken with the two MTPCs of central, head-on collision events that make up 5% of the total inelastic interaction cross section. The data were taken during the six week heavy ion running period of the SPS in the Fall of 1995.

2.2 Event Trigger and Selection

The amount of forward going energy near zero degrees indicates how central the collision is. If the beam nucleus does not interact hadronically within the target, the entire Pb nucleus, with its 33 TeV of energy, continues downstream into the Veto calorimeter. Any reaction will result in some energy transverse to the beam axis, reducing the amount of longitudinal spectator energy measured in the veto calorimeter. With a valid beam particle signal from the quartz detectors in front of the target, the VCAL will veto the event if it measures energy above a set threshold. Otherwise, the event is judged to be sufficiently central and is taken.

The correlation between the veto energy and transverse energy is shown in Figure 2.3 with data from a dedicated Ring and Veto calorimeter run [67]. With a Pb foil target in place, a linear relationship between the two types of energy is seen. The

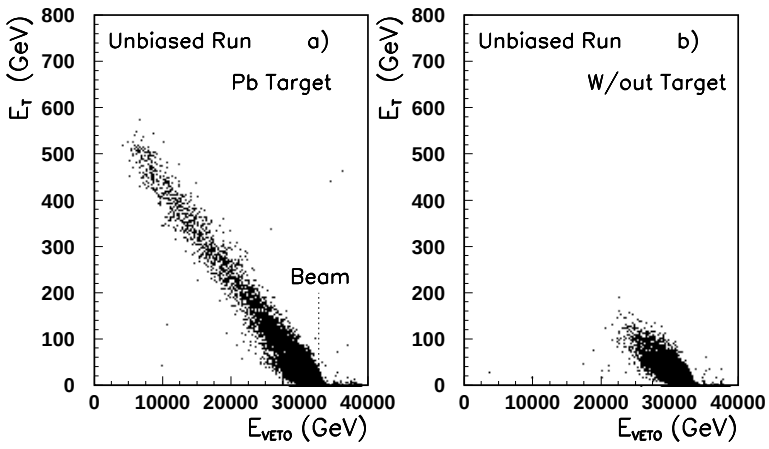

Figure 2.3: The correlation between transverse energy E_T and zero degree energy E_{veto} as measured by the RCAL and VCAL, respectively for events with a Pb foil target (left) and no target (right). The total beam energy of ^{208}Pb is 33 TeV.

target-out data shows the combination of beam only events and background from beam interactions with air, helium in the beam line, and the TPC gas.

The (VCAL), made of layers of lead, iron, and plastic scintillator, is located 20 m downstream from the target. Its aperture is collimated to an opening of 43×10 cm^2 so that only the spectators (protons, neutrons, and nuclear fragments) to the collision can enter. The horizontal opening is wider than the vertical opening because the magnetic field spreads out the charged particles in the horizontal plane. Fermi motion also contributes to the spatial distribution of particles.

The central collision trigger was set to take events with a Veto energy less than 25% of the total beam projectile energy of 33 TeV. Figure 2.4 shows the Veto energy distribution from the central and minimum bias triggers. Calorimeter gain corrections slightly reduce the value of the energy measurement.

A simulation of the central trigger [68] estimated the selected impact parameters to be $b < 3.3$ fm for a Glauber model of the nucleus (the radius of a Pb nucleus is approximately 7 fm), which corresponds to 5% of the Pb+Pb total inelastic cross section. Even with the small collimated aperture of the VCAL, as much as 50% of the measured energy is from non-spectator matter. The simulation indicated that the veto energy includes both hadronic background from interactions away from the target and produced particles from the target (neutral particles are unaffected by the magnets and can enter the VCAL even at low momentum). The simulation results can be seen in Figure 2.4, where the impact parameter distribution has a tail of events larger than $b = 3.3$ fm.

Because a valid trigger is based on the absence of signal in the VCAL, unwanted

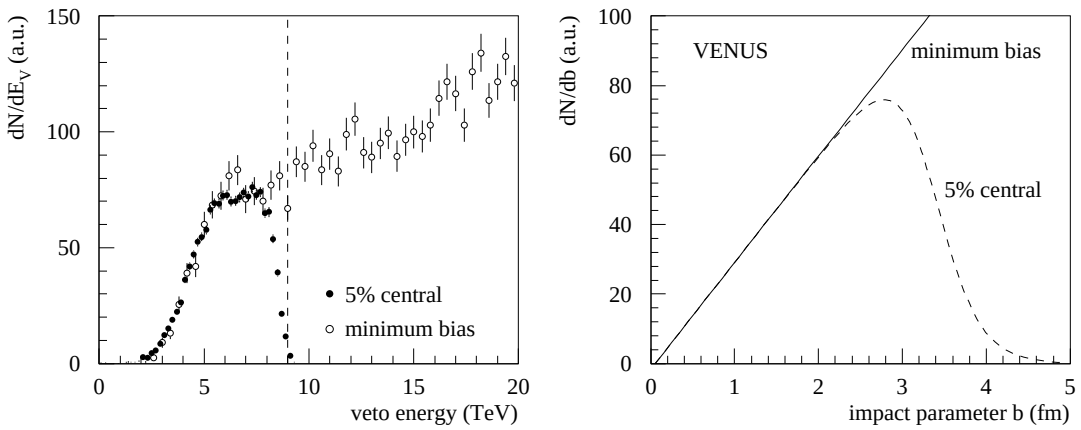

Figure 2.4: (Left) Veto energy E_{veto} from 5% central and minimum bias triggers after calorimeter gain and background corrections. The 5% central trigger energy threshold is indicated by the dashed line. Beam energy (33 TeV) is off scale. (Right) Calculated impact parameter b distributions from simulation. Due to nuclear density and background effects, the 5% central trigger has limited precision, resulting in the tail in the b distribution.

events may be taken such as a peripheral collision followed by an interaction between the beam fragment and a gas molecule or some other material. These events are rare and can be easily rejected by the TPC track multiplicity. Around 2% of low E_{veto} events have less than half the number of TPC tracks expected from a typical central collision.

2.3 The Time Projection Chamber

2.3.1 The NA49 TPC

General Features

The TPCs are rectangular in shape, of dimension $3.9\times3.9\times1.8$ m^3 ($l\times w\times h$) for the MTPC and $2.5\times2.0\times1.0$ m^3 for the VTPC. The TPC gas box frame is made of G-10 fiberglass and the gas is contained by two 125 μm mylar windows. N_2 is flushed between the windows to prevent water vapor and oxygen contamination of the gas. Additional materials include a cage made of 25 μm thick aluminized mylar strips encircling the gas volume to define the electric drift field. The strips are located inside the windows and are held in place by friction on ceramic rods. A rigid aluminum support frame on top of the gas box also holds the TPC readout sectors. The VTPCs have a split field cage so that the beam can pass through the detectors in a region without readout instrumentation. Otherwise, δ electrons produced by the beam could create a spark in the readout chambers or saturate the electronics. A particle passing through both VTPCs and one MTPC is presented with an integrated interaction

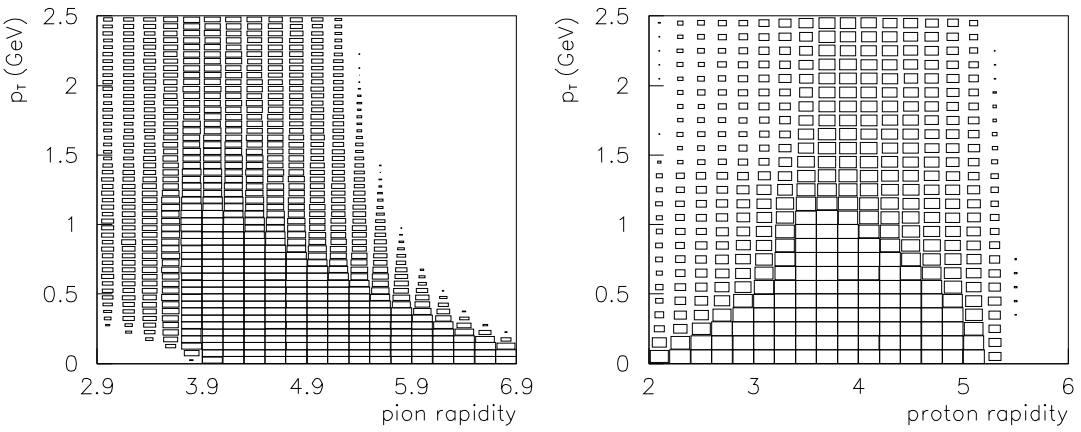

Figure 2.5: Rapidity and transverse momentum coverage in the MTPC for pions (left) and protons (right) integrated over all transverse azimuthal angles. The box size relative to the bin size grows with increasing coverage.

length from the windows and field cage strips of 0.3%.

A nearly continuous trail of ionization is measured by the TPC readout. The MWPC readout is divided into sectors of area 72×72 cm^2 separated by a gap approximately 2 cm wide. Two dimensions (x and z in the NA49 coordinate system) are defined by the cathode readout plane, which is segmented into pads to provide position measurements. The third dimension (y) is orthogonal to the readout plane, and is divided into discrete timeslices defined by the electron drift velocity in the gas and the time sampling rate of the readout electronics. The connected group of pad-time pixels that register signal from a particle crossing the gas volume subtended by a transverse row of pads in the $\hat{x}-\hat{y}$ plane is called a charge cluster. The TPC track is formed from the set of clusters along the particle path and the cluster positions are fit to a curve or straight line to determine the trajectory.

Because this work is based on data from the MTPC, the focus will be on the properties of that detector. A discussion on the TPC gas and pad readout properties will follow in this section. Detailed descriptions of the NA49 TPCs along with performance reports can be found in [63, 69].

Phase Space Acceptance

The phase space coverage, or acceptance, of pions and protons in the MTPCs is shown in terms of rapidity and transverse momentum in Figure 2.5. The center of mass rapidity in the laboratory frame is $y_{lab} = 2.9$. The symmetry of the MTPC setup results in identical acceptances from both left and right detectors. In each MTPC, acceptance is defined only for particles of a single charge sign. When the magnet setting is $STD+$, positive charge is deflected towards the Left MTPC.

The p_T coverage is integrated over all azimuthal angles ϕ (defined by p_x and p_y).

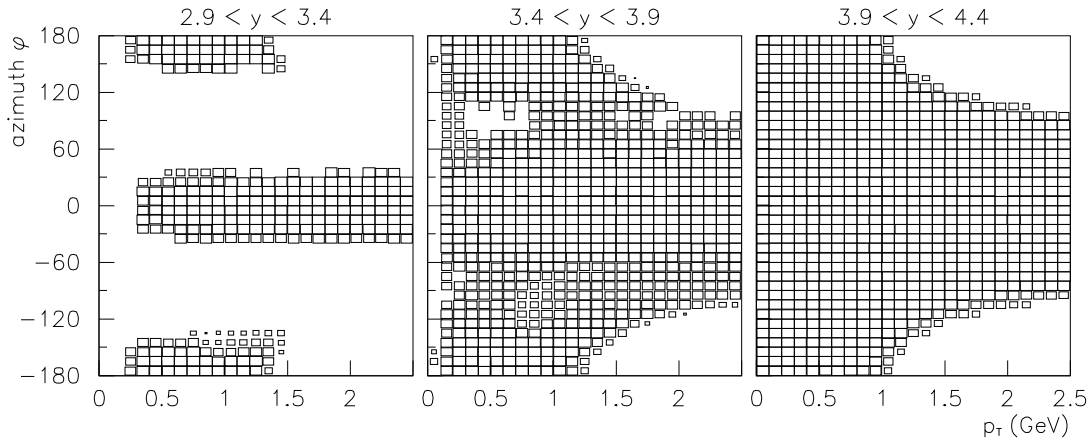

Figure 2.6: MTPC acceptance of pions as a function of transverse momentum p_T and azimuthal angle ϕ in three rapidity intervals. The box size relative to the bin size grows with increasing coverage.

In each MTPC, $\phi = 0°$ is in the same direction ($\pm\hat{x}$) as the magnetic field p_T kick. For the $STD+$ setting, $\phi = 0$ in the left MTPC coincides with $+\hat{x}$. $\phi = 90°$ is always in the $+\hat{y}$ direction. Particles with $|\phi| < 90°$ have "right side" p_T, while $|\phi| > 90°$ have "wrong side" p_T. (The range of ϕ is between $+180°$ and $-180°$.)

Acceptance in terms of p_T and ϕ is shown in Figure 2.6 for pions in three rapidity intervals. Particles with rapidities $2.9 < y < 3.4$ and $\phi \sim \pm 90°$ pass above or below the MTPC and are not accepted at all. This does not occur at higher rapidities because the larger longitudinal momentum results in a smaller angular deflection from the magnetic field and p_T. With sufficiently high wrong side p_T (> 1 GeV, $\phi \sim \pm 180°$), a particle can travel through the gap between the MTPCs or even end up as a "wrong charge" track in the opposite MTPC.

Gas Selection

The driving concerns for the gas used in a TPC involve its diffusion, drift velocity, and ionization loss properties. The choice of TPC gas was based on detailed studies of various gases in a TPC environment that can be found in [70, 71].

The transport of ionization to the readout region results in a spatial diffusion of the electrons from elastic electromagnetic collisions with the gas. The magnitude of the charge cluster spread and movement of the cluster centroid depends on the number of electrons forming the cluster. The transverse width of a cluster has a major impact on the two track resolution of the detector. Roughly speaking, a track separation around twice the average cluster radius is needed to resolve the tracks.

$ArCH_4$ is frequently used in TPCs because its drift velocity is relatively fast, at around 5 cm/μs, and nearly constant for drift fields in the range of 100 to 200 V/cm. However, its transverse diffusion constant is large, at 600 μm per $\sqrt{cm}$ of drift, and

will contribute to a poor two track resolution of over 2 cm for tracks at the beam height.

Ar-CH_4-CO_2 in a $90-5-5\%$ mixture was selected to be the gas for the MTPCs. It is called a cool gas mixture because its drift velocity is slow, around $v_d = 2.4$ cm/μs, and the diffusion constant is only $c_D = 270$ μm/$\sqrt{\text{cm}}$ for a drift field of 175 V/cm. The drift length from beam height to the MTPC readout plane is 60 cm and the maximum drift length 1.12 m. The VTPCs has a shorter drift length, but comparable solid angle relative to the target, and therefore uses a slower gas, Ne-CO_2 ($90-10\%$, $v_d = 1.4$ cm/μs, $c_D = 220$ μm/$\sqrt{\text{cm}}$).

Unfortunately, cool gases have a substantial variation in drift velocity with drift field of about 0.016 cm/μs per V/cm for the Ar-CH_4-CO_2 mixture. To ensure a sufficiently uniform drift velocity along the entire drift length and in time, the field cage must be adequately stable and precise. Temperature and atmospheric pressure also affect the drift velocity. While temperature can be stabilized through air conditioning, nothing can be done about the pressure changes from day to night and changes in weather. Water in the gas can slow the drift velocity by 2% per 100 ppm. The drift velocity is determined for each event through a separate test monitor in the gas circulation system and through a measurement of the "charge step", which is the timeslice where the TPC readout ends because the bottom of the TPC is encountered. (The total drift readout time is fixed at 51.2 μs and corresponds to nearly 123 cm.)

Charge losses occur during drift due to recombination and electron attachment. Contaminants such as water vapor and oxygen are electronegative and can also alter the electron drift velocity. The speed and stability of the drift velocity affects the measurement of the vertical y coordinate.

The Ar-CH_4-CO_2 mixture has a level of electron affinity an order of magnitude greater than that of Ar-CH_4.[1] The loss over the maximum drift length of 1.12 m is 0.6% per ppm of oxygen contamination. No loss could be attributed to water vapor at up to a concentration of several hundred ppm. Filters and fresh gas circulation help reduce the level of O_2 to 2-4 ppm and H_2O to 20 ppm. Gas flow is achieved by operating the TPC at a slight 0.5 mbar overpressure and new gas is introduced at a rate of 2% by volume per hour.

Drift Field, Pad and Wire Planes

The homogeneous electric field used to transport ionization up to the top of the MTPC for collection is defined by a conducting plane at the bottom of the chamber and a wire plane called the Frisch grid near the top that are held at a voltage difference of around 20 kV for a drift field of 175 V/cm. The uniformity of the field is defined by

[1] While Ar has a negative electron affinity, CH_4 and CO_2 are electronegative. However, the primary cause of charge loss is not the electron affinity of CO_2, but rather its ability to deexcite O_2^{-*} into a stable state [72]. Otherwise, the captured electron would be released within 10^{-10} seconds.

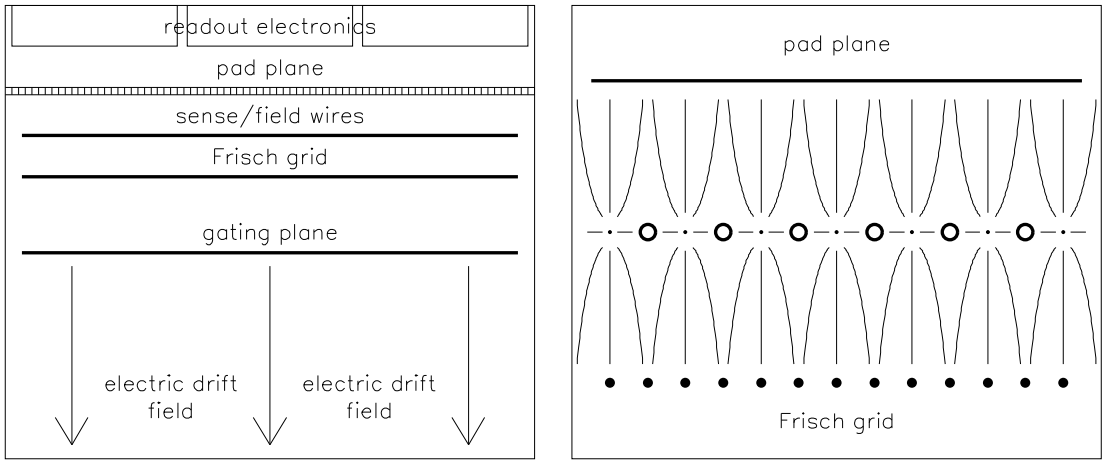

Figure 2.7: (Left) An illustration of the pad and wire planes of the MTPC, not drawn to scale. (Right) The electric field lines in the MWPC section of the MTPC.

strips of aluminized mylar encircling the chamber. These strips are connected with a resistor chain and are at intermediate voltages between the zero voltage of the Frisch grid and negative high voltage of the bottom plane.

At the top of the MTPC is a multiwire proportional chamber (MWPC) formed by wire planes and a segmented conducting surface called a pad plane. A schematic drawing of these components, not to scale, is given in Figure 2.7. The Frisch grid and the pad plane act as cathodes at zero voltage. In between, there is a plane of alternating anode (sense) and cathode (field) wires. The pad plane floats electrically and is capacitively coupled to the anode sense wires that are held at around 1 kV. The spacing between sense and field wires is 2 mm, which balances spatial resolution and difficulty of construction. It is important for the Frisch grid to mimic a constant voltage plane for field uniformity, and so its wire spacing is only 1 mm. The electric field inside the MWPC section is also uniform except in the immediate vicinity of the sense wires. Electrons approaching the sense wires are rapidly accelerated, triggering an amplifying ionization avalanche. In the NA49 TPCs, signal readout is from the induced signals in the pads. The positively charged ions that are moving away from the sense wires have corresponding image charges in the conducting pad plane.

One additional wire plane, the gating grid, is used to shield the MWPC from ionization in the chamber when there is no event trigger so that the readout electronics are not saturated. The gating grid is held at ground when closed so that it is at the same potential as the Frisch grid. When the gate is opened, the voltage is dropped to a negative value so that a drift field is defined between the gate and the Frisch grid and the ionization can continue towards the amplification region.

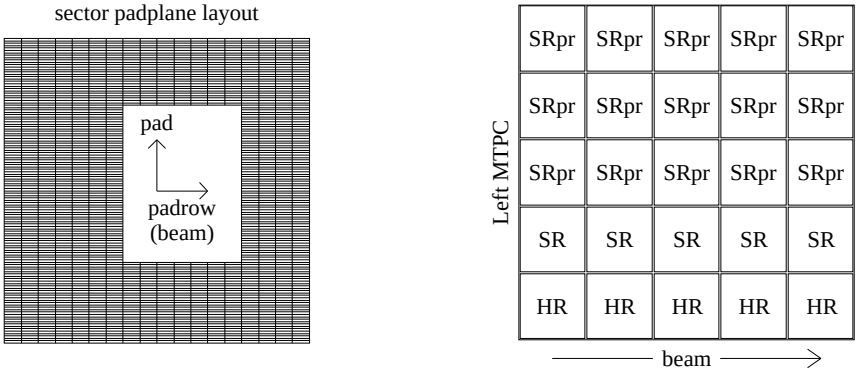

Figure 2.8: (Left) Each TPC sector contains a pad plane. The padrow and pad directions are as indicated. (Right) The layout of the 25 Left MTPC readout HR, SR, and SR-prime sectors. The Right MTPC is the mirror image of the Left across the beam line.

Readout Sector Layout

Each TPC is divided into modules of pad and wire planes of dimension 72×72 cm^2 called sectors. There is an uninstrumented gap of approximately 2 cm between each sector. Each pad plane is divided into a grid of pads along two directions where padrow refers to the line of pads at the same longitudial coordinate (z_{tpc}) relative to the TPC walls. The pad direction (x_{tpc}) is orthogonal to the padrow direction. The padrow and pad directions are indicated in Figure 2.8. The division of the vertical y_{tpc} direction is determined by the drift velocity, time sampling rate (10 MHz), and number of time samples (512).

To achieve a similar solid angle granularity for all pad-time pixels, the VTPC drift velocity is slower than the MTPC drift velocity. The VTPC pad widths are are also narrower than that of the MTPC for the same reason. Near the beam line, narrow pads are needed in the MTPC to resolve close tracks in the high density environment. Away from the beam, wider pads can be used because the track density decreases due to the dispersion resulting from the magnetic field.

The pad width and charge cluster size need to be matched to optimize the spatial resolution. A Gaussian distribution is a good approximation of the cluster shape because there are many electrons created in the ionization avalance around the sense wires. If the signal is spread across at least three pads, then the charge distribution can be fit to a Gaussian to calculate its position. The resolution should be much smaller than the pad width. In contrast, if the charge were limited to a single pad, then the cluster position would be assigned to the center of the pad and the resolution would be $1/\sqrt{12}$ of the pad width.

A point charge distribution diffuses over 60 cm of drift distance to a width of 2 mm in the MTPC gas. Neglecting other effects, the pad widths should be on the order of

Main TPC Left and Right					
Sector Type	Sectors	Rows	Pads	Pad Pitch	Pad Angle
HR	5	18	192	3.63 mm	0
SR	5	18	128	5.45 mm	0
SR-prime	15	18	128	5.45 mm	15°

Vertex TPC						
	Sectors	Rows	Row Pitch	Pads	Pad Pitch	Pad Angle
VTPC1	6	24	1.6, 2.8 cm	192	3.5 mm	12-55°
VTPC2	6	24	2.8 cm	192	3.5 mm	3-20°

Table 2.1: In all TPCs, there is a gap of 0.5 mm between pads in both padrow and pad directions. Angled pads are aligned away from the beam axis to reduce the padrow crossing angle. The row pitch is 3.95 cm for all MTPC sectors.

the diffusion. (Due to capacitive coupling, the pad readout has an intrinsic response that convolutes with the diffusion effect, resulting in a wider observed cluster. A slightly wider pad can be used for cost efficiency. Section B.2.2 contains a discussion on a parameterization of the TPC readout, called the pad response function.)

Particles crossing padrows at non-normal incidence spread out their signal in a non-Gaussian manner. While a uniform distribution across several pads can still yield an accurate padrow crossing point, such wide charge clusters will degrade the two track resolution. This is a significant effect primarily in the pad direction, which coincides with the bend plane. Vertical dip angles are much smaller and are not as important a consideration as the padrow crossing angle.

Each MTPC is rotated by 2.5° around its central $\hat{y}$ axis to reduce the padrow crossing angle (Figure 2.1). Three types of sectors are used in the MTPC with different pad sizes and shapes. Closest to the beam are the high resolution sectors (HR), which have the narrowest pads because a finer tracking resolution is needed due to the high particle density near the beam line. Next are the standard resolution (SR) sectors, which have slightly wider pads. The SR-prime sectors are farthest away from the beam and have angled pads to handle tracks at significant angles. A diagram of the sector configuration is shown in Figure 2.8. Table 2.1 lists the pad dimensions from each sector type, including the VTPC sectors. Note that the VTPC have a wide range of pad angles because of their location within the magnetic field and proximity to the target.

From Gaussian fits of clusters originating at beam height, the cluster sigmas in the pad (x) direction are 3.0, 3.7, and 3.4 mm for the HR, SR, and SR-prime sectors respectively. In the time direction, the sigmas are 3.0 mm for all three sector types because pad width does not affect diffusion in the time direction. Clusters in the SR sectors are the widest in the pad direction because the SR pads are not angled. As

a result, the average padrow crossing angle is greater in the SR sectors than in the other two sector types.

Electronics, Data Aquisition, and Raw Data Format

The two MTPCs require 105,264 channels of data readout. In total, over 182,000 TPC pads are read out for each event. The cost and complexity of so many channels can only be managed by minaturizing the readout electronics with VLSI technology into custom integrated circuits. The electronics design is described in [73] and a recent performance report can be found in [63].

The Front End Electronics (FEE) are directly mounted onto the TPC sector modules and consist of preamplifiers and shaper amplifiers (PASA) on one chip followed by switched capacitor arrays (SCA) and analog to digital converters (ADC) on another chip. Each chip contains 16 readout channels and each FEE card contains two sets of these chips. The MTPC HR sectors use 6 FEE boards per padrow while the SR and SR-prime sectors use 4 boards per padrow.

The preamplifier integrates the input with a gain of 50 mV/fC and then the shaper amplifier forms pulses with a FWHM of 0.24 μs. This width produces a signal width in the time direction comparable to the typical cluster pad width from the beam height. The analog output of the PASA is time sampled 512 times at 10 MHz and stored in a switched capacitor array. (The 0.1 μs timeslice size is actually smaller than necessary based on the shaper width.) The ADC digitizes the sampled data to a 9 bit precision. At this stage, the event size is over 100 MB.

The data are multiplexed by the Control and Transfer (CT) boards, which are also mounted on the TPC support frame to minimize the length and number of FEE connector cables. A total of 768 channels are combined and sent over a single optical fiber cable to VME Receiver boards. The Receivers are the first part of the data aquisition system (DAQ) [74] that processes, assembles, and records the data. Each Receiver handles 3072 channels from four CT boards with independent daughter boards. A total of 60 Receivers are used and are housed in 6 VME crates. The integration of the readout electronics means that only 240 data cables come from the detectors to the DAQ system.

For the typical 20 triggered events per 5 second spill, the DAQ has an additional 15 seconds to process and record the data until the next spill arrives. The VME Receiver daughter boards have digital signal processors running in parallel to reduce the noise level and compress the data through zero supression. A CAMAC based event builder takes the processed data and assembles it in one of 32 event buffers where the event waits to be recorded onto tape.

Because of the inherent noise of the readout electronics, every pad-timeslice pixel contains signal. This pedestal, typically around 10 counts, is subtracted using a constant determined from an event-averaged noise measurement for each pixel. Underflows are set to zero. After pedestal subtraction, the level of noise is typically 2 to 3 counts. To reduce data volume, a threshold of 5 counts is imposed. Much of the

data now consist of zeros from the empty space between tracks. A simple compression algorithm requiring adjacent signals above threshold is used to further reduce the event size by supressing the zeros. The data is stored with an 8 bit precision corresponding to a dynamic range of 0 to 255 counts. After all data processing, the typical event size of a central Pb+Pb collision is reduced by over a factor of 10 to around 8 MB.

In 1994, the Sony DIR-1000M tape drive was the only available device with a sufficiently high recording speed (16 MB/sec) to handle the NA49 data taking rate. The 10^6 events recorded each year presents a significant expense in terms of recording media. The Sony drive media stores up to 100 GB per tape (corresponding to around 100 minutes of uninterrupted running or on the order of 10^4 events) and is cost competitive with other media.

MTPC Performance

Near the beam line, the average track density in the MTPC can be as high as 1 particle per cm^2. Because of the divergence in track angle introduced by bending in the magnetic field, the track density decreases by 40% going from the front to rear face of the detector. An average two track resolution of 1 cm was achieved. The momentum resolution is estimated to be $\Delta p/p^2 = 3 \times 10^{-4}$ GeV^{-1}. From the residual distribution of cluster centroid positions relative to fitted tracks, the single track spatial resolution is 450 μm in the magnet bend plane ($\hat{x}$) and 350 μm out of the bend plane ($\hat{y}$).

2.3.2 Particle Identification from Ionization Measurement

Charged particles passing through material lose energy mainly through inelastic electromagnetic interactions with the atomic electrons. The energy loss goes into atomic excitation or ionization. The quantum mechanical calculation of mean energy loss per unit length of material dE/dx leads to the Bethe-Bloch formula, which is a function of the particle charge (z) and velocity ($\beta = v/c$) when the particle mass is much larger than the electron mass. The Bethe-Bloch formula takes the form

$$-\frac{dE}{dx} = C_1 \frac{z^2}{\beta^2} \left[\ln\left(\frac{C_2}{1-\beta^2} \right) - 2\beta^2 + \text{corrections} \right]. \tag{2.1}$$

The parameters C_1 and C_2 depend on the properties of the material. The correction terms limit the maximum energy loss at low and high particle energies. A further discussion of the principles of energy loss in materials can be found in several textbooks [72, 75, 76].

The ionization[2] created in a TPC can be measured to provide information on the

[2] Energy loss, energy deposition, and ionization will be used interchangably in the text as dE/dx.

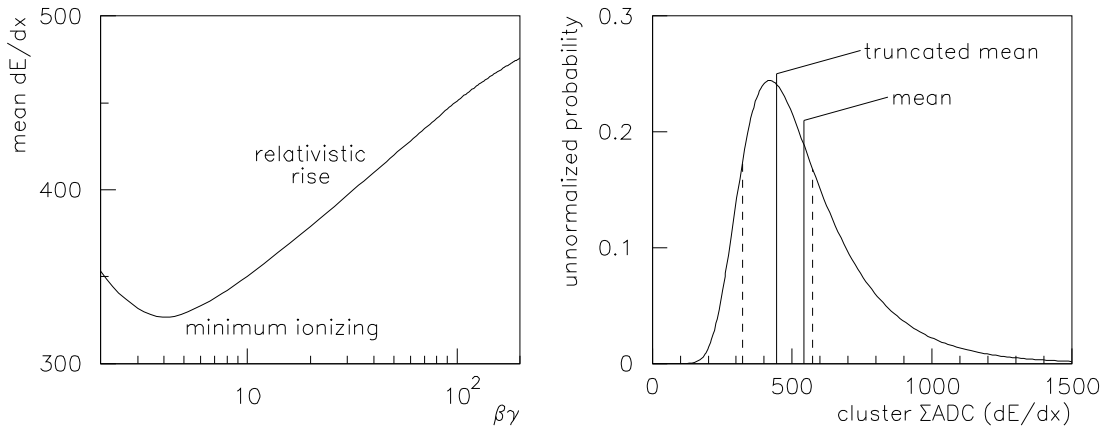

Figure 2.9: (Left) Bethe-Bloch curve of mean dE/dx as a function of $\beta\gamma$ for charge $q = 1$ particles. The typical particle velocities from A+A collisions at CERN-SPS energies fall along the section of the curve labelled as the relativistic rise, where $\langle dE/dx \rangle$ increases monotonically. (Right) An idealized probability curve of energy deposition by a charged particle passing through gas, as measured in total counts by the TPC readout electronics. The truncated mean value $\langle dE/dx \rangle$, calculated for the region defined by the dashed lines, is closer to the most probable dE/dx than the mean of the entire distribution.

particle mass. Because the energy loss of charged hadrons depends only on velocity, particles with the same momentum, but of different mass, will produce tracks with different amounts of ionization. An example of an energy loss curve as a function of $\beta\gamma$ ($\gamma = 1/\sqrt{1-\beta^2}$) is given in Figure 2.9.[3] At velocities lower than $0.95c$ ($\beta\gamma \sim 3$), energy loss is dominated by the $1/\beta^2$ term. Around $v \sim 0.95c$ the energy loss reaches a minimum ionizing point. Above this point is the relativistic rise region, where the energy loss increases monotonically with velocity.

Even at low momentum, an electron reaches a very high $\beta\gamma$ factor that is off the scale in Figure 2.9. Consequently, the typical energy loss of electrons is higher than that of any hadron in the relativistic rise region. Because of the low electron mass, radiative mechanisms of energy loss such as bremsstrahlung and Cherenkov light emission are also important.

The Bethe-Bloch formula predicts a precise dE/dx without consideration for the statistical nature of energy loss. While crossing several meters of a light material such as a gas, relativistic particles do not suffer enough collisions for the Central Limit Theorem to be applicable. In addition, the Bethe-Bloch prediction does not include the possibility that a single large momentum transfer can produce a fast δ (knock-on) electron. The statistical and dynamical fluctuations result in a variation in energy loss of over 20% of the mean measurement.

[3] The calibration and analysis of the dE/dx data from the MTPCs was the subject of the Ph.D. thesis of A. Mock [77], who provided the equation for the energy loss curve.

When the ionization of a single track is measured through many small individual samples, the distribution of these dE/dx samples follows a Landau probability distribution. Figure 2.9 shows an example of a parameterized dE/dx distribution from a single track. The tails of the distribution cause the mean dE/dx value to differ from the most probable energy loss as predicted by the Bethe-Bloch formula. In practice, a finite number of measured samples results in a mean that can suffer from large fluctuations.

A much more stable mean value can be extracted when the tails of the distribution are discarded before the mean is calculated. This truncated mean energy loss ($\langle dE/dx \rangle$) is also closer to the most probable dE/dx. In the MTPC, there can be up to 90 independent dE/dx samples from padrow charge clusters. Each padrow collects the ionization from 4 cm of particle flight. The dE/dx truncation employed in NA49 removes the lowest 10% and highest 35% of all samples. These cuts are illustrated as dashed lines on the parameterized energy loss distribution shown in Figure 2.9.

The Bethe-Bloch curve for the MTPC gas indicates that in the relativistic rise, there is a 4 to 5% separation relative to the mean energy loss between pions and kaons (and also kaons and protons) at the same momentum. The measured $\langle dE/dx \rangle$ has a resolution that depends on the number of samples, the type of gas used, and other experimental factors. From NA49 data of a large ensemble of tracks, the Gaussian distributed resolution for the MTPC Ar-CH_4-CO_2 mixture was found to be around 6% [78].

In order to identify individual particles by $\langle dE/dx \rangle$, the resolution must be much smaller than the difference in ideal energy loss between two particle types. Although this is not the case with the MTPC, there is enough information so that an ensemble of particles can be analyzed to provide particle identification at a statistical level. The technique used in this work to find net protons is discussed in Chapter 3.

2.4 Further Reading

An introduction to the basics of charge drift and diffusion in gases and the principles behind drift chambers and multiwire proportional chambers can be found in a CERN training lecture by Sauli [65]. Textbooks with material about TPCs include a monograph by Blum and Rolandi [72] and an general overview of experimental techniques by Leo [75].

The first high energy physics implentation of a TPC was by the PEP-4 experiment at SLAC [64, 79]. Experimental studies of the TPC performance were made by Fancher *et al.* [80, 81]. The ALEPH experiment [82] at the CERN-LEP is perhaps the most widely known current application of the TPC. Their "handbook" [83] is a primer of the design and operation of the detector systems as well as the offline data analysis. It gives a comprehensive review of the experiment.

For another heavy-ion application of the TPC, the STAR experiment [84] differs significantly from NA49 because it operates in the RHIC collider [85] environment,

where two Au beams at 100 GeV per nucleon intersect. The STAR TPC has symmetric coverage about midrapidity and measured particles have primarily transverse momentum in contrast to the dominant longitudinal momentum component seen in the fixed target setup of NA49.

Chapter 3

Data Analysis

3.1 Measurements

3.1.1 Net Protons and Baryon Stopping

For this work, net protons ($p-\bar{p}$) were measured with the MTPCs. By combining net proton data with measurements from other analyses and predictions from event models, an estimate of the net baryon rapidity distribution can be made. Additional particles that comprise baryons are the neutron, Λ, Σ, and their antiparticles. Heavier, multistrange baryons such as the Ξ and Ω are produced in much smaller quantities than the lighter baryons[1] and were not included.

The ratio of neutrons to protons in ^{208}Pb is 1.54:1. This ratio can change in the final state of a Pb+Pb collision because isospin can be redistributed from nucleons to other hadrons. The VENUS and RQMD models predict a final state net neutron to net proton ratio from central Pb+Pb collisions of approximately 1.07:1, independent of rapidity except near target and beam rapidities.[2] There the number should be closer to the initial ratio simply because spectator matter comes directly from the ^{208}Pb nucleus. The rapidity distribution of this ratio from RQMD is shown in Figure 3.1. The net neutron rapidity distribution was inferred from the measured net proton distribution as

$$n-\bar{n} = (1.07\pm0.05)(p-\bar{p}). \tag{3.1}$$

While neutral hyperons have been found through their weak decay into two detected charged particles,[3] $\Sigma^{\pm}$ decay to one charged and one neutral particle and are

[1] Preliminary measurements from central Pb+Pb collisions over a limited area in phase space show that the $(\Xi+\bar{\Xi}):(\Lambda+\bar{\Lambda})$ ratio is 0.13 [86] and $\Omega:\Xi$ is 0.2 [87]. Central S+S collisions result in $p:\Lambda$ close to three [29] .

[2] A neutron to proton ratio of 1.3±0.3 for spectator nucleons was measured with the NA49 Veto Calorimeter [88], which is close to the $n:p$ ratio of ^{208}Pb.

[3] Λ (plus Σ^0, which decays to Λ electromagnetically) production from central Pb+Pb collisions has been the subject of several NA49 Ph.D. dissertations [89, 90, 91].

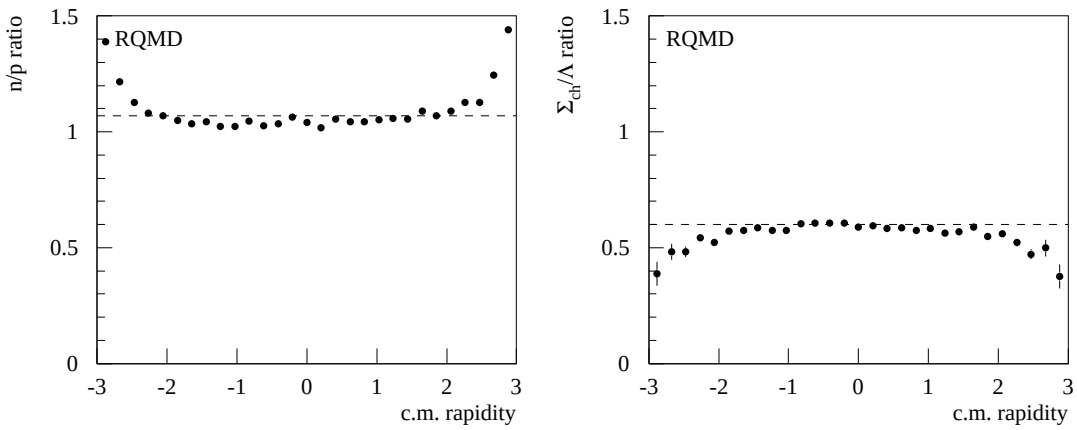

Figure 3.1: RQMD model predictions of the rapidity dependence of $(n-\bar{n})$:$(p-\bar{p})$ and $(\Sigma^{\pm}-\bar{\Sigma}^{\pm})$:$(\Lambda-\bar{\Lambda}+\Sigma^0-\bar{\Sigma}^0)$ from central Pb+Pb collisions. The dashed lines indicate the ratios used in Equation 3.3 to estimate net baryons from the net protons and net lambdas.

difficult to detect. In fact, there has not been a reported $\Sigma^{\pm}$ measurement from nucleus+nucleus collisions.[4]

An empirical formulation to extend the $Y^0 = \Lambda + \Sigma^0$ yield to include $\Sigma^{\pm}$ was given in a study of elementary hadron+hadron collision data by Wróblewski [93] as

$$\Sigma^+ + \Sigma^- = (0.6 \pm 0.1)(\Lambda + \Sigma^0). \tag{3.2}$$

Because the Σ is a different isospin state than the Λ, the Wróblewski factor may not be the same for nucleus+nucleus collisions as for proton+proton collisions. The RQMD and VENUS models, which account for isospin, also predict $(\Sigma^+ + \Sigma^-) : (\Lambda + \Sigma^0) \approx 0.6$. The rapidity dependence of this ratio from RQMD is shown in Figure 3.1.

From Equations 3.1 and 3.2, the net baryon rapidity distribution was estimated from the net proton and net Λ (including Σ^0) rapidity distributions as

$$B-\bar{B} \ = (2.07 \pm 0.05)\cdot(p-\bar{p}) + (1.6 \pm 0.1)\cdot(Y^0-\bar{Y}^0). \tag{3.3}$$

The only experiment that can measure Λ from Pb+Pb collisions over a large part of phase space is NA49. However, given the preliminary state of the net Λ measurement from NA49 analyses [94], the impact of using predictions of net Λ from models to estimate net baryons was also studied (Section 3.5.3).

Because rapidity distributions of particles with slightly different masses (m_p and m_Λ) are combined to form the net baryons, the resulting rapidity variable is not

[4] The WA97 experiment [87] at CERN specializes in measuring strange baryons, but has reported neither a Σ yield nor a ratio of Σ/Λ. For Au+Au collisions at the lower BNL-AGS energies, E810 [92] searches for H_0 dibaryons through a $\Sigma^- p$ decay channel, but has not reported a Σ yield.

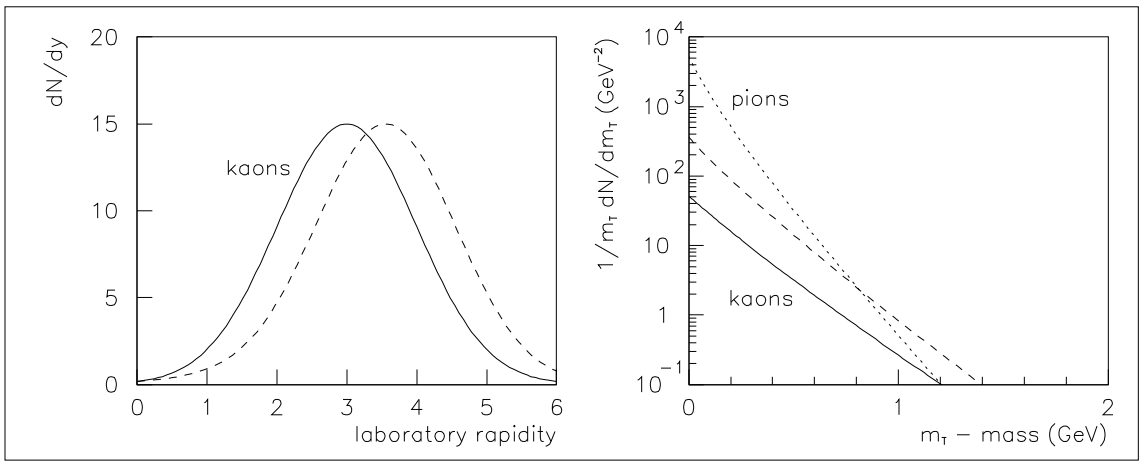

Figure 3.2: The use of a pion mass hypothesis to calculate rapidity and transverse mass will affect the h^- spectra. (Left) A kaon rapidity distribution centered at midrapidity is shifted from the solid line to the dashed line when the π mass is used to calculate rapidity. (Right) A negative charge hadron m_T spectrum will have a rise at high m_T because of the contribution from kaons. The solid line shows a K transverse mass distribution where $T = 235$ MeV. When the pion mass is used to create the m_T spectrum (dashed line), the distribution changes because the pion mass is smaller than the kaon mass. For comparison, shown as the solid line is a pion m_T distribution with ten times the yield and $T = 154$.

precisely defined. Another type of hybrid distribution could be created by recasting the Λ distribution in terms of rapidity calculated with a proton mass hypothesis, but the overall differences between these distributions will not be significant.

Transverse momentum distributions of net protons will also be presented. In a system with radial transverse flow, the shape of the p_T distribution at midrapidity is largely determined by the particle mass. Because the masses of the various baryons that contribute significantly to the net baryon spectrum are similar, no additional information will be gained from creating a net baryon p_T distribution.

3.1.2 Negative Charge Hadrons

As a gauge of the total particle production, negative charge (h^-) hadrons are better than positive charge hadrons (h^+) because participant protons are included with the h^+. The h^- are mostly pions, which have a low mass and are easily produced. Therefore, the rapidity calculation for the h^- will use the pion mass. Charged kaons and antiprotons are produced in much smaller numbers than pions. From central S+S collisions at CERN-SPS energies, the $K:\pi$ ratio is approximately $0.1:1$ [95] and the $\bar{p}:h^-$ ratio is $0.016:1$ [96].

The negative charge hadron y and p_T spectra are skewed by the contributions of K^- and $\bar{p}$. This is demonstrated in Figure 3.2 with parameterized phase space distributions of pions and kaons. A Gaussian K rapidity distribution centered at

midrapidity loses its Gaussian shape and is shifted forward when the π mass, which is less than a third of the K mass, is used to calculate rapidity from the laboratory momentum value. As a result, the h^- rapidity distribution will have slightly more yield in the forward half in rapidity than in the backward half.[5] A kaon transverse mass distribution with the form $1/m_T \cdot dN/dm_T \propto \exp(-\sqrt{p_T^2 + m^2}/T)$ (Equation A.12), where $T = 235$ MeV [97], is shown in Figure 3.2. When the m_T distribution is created using the pion mass, its shape changes because the pion mass is smaller than the kaon mass. Also shown for comparison is a pion m_T distribution with the same functional form as the kaons, but with ten times the yield and $T = 154$ MeV [97]. An h^- transverse distribution will be concave, with pions dominating the low p_T region and the heavier K^- and $\bar{p}$ creating a tail with a flat slope at higher p_T.

3.2 Data Taking

The data analyzed for this work were taken in the Fall of 1995 over a continuous two day span out of the total six week Pb beam operating period of the accelerator. The entire data set was taken using the central collision trigger described in Section 2.2 that selected events comprising the most central 5% of the total Pb+Pb inelastic collision cross section. 5×10^4 events were used for the $p-\bar{p}$ analysis and 8×10^3 events were used for the h^- analysis. The $p-\bar{p}$ measurement involved a differential analysis of particle energy losses in the TPCs and required higher statistics than the h^- analysis, which was basically a count of tracks in a single MTPC.

The vertex magnets were operated in the $STD+$ configuration, in which the magnetic dipole field points in the $-\hat{y}$ direction. (Positive charge particles are bent in the $+\hat{x}$ direction.) Some data taken at a later date with the $STD-$ configuration will also be examined to determine whether there are any systematic effects due to the magnet polarity.

3.3 TPC Track Analysis

3.3.1 Event Reconstruction

Only data from the MTPCs were used in this work. Located downstream of the magnets and outside of their fields, the MTPCs detect particles as straight line tracks. This characteristic greatly simplifies the pattern recognition task of the reconstruction software. The large volume of the MTPC translates to an excellent phase space coverage, and an important feature of the MTPCs is its particle identification capability through a measurement of energy loss in the detector gas. The MTPC event

[5] This only occurs with fixed target experiments, where momentum is not measured in the center of mass frame.

reconstruction software[6] finds tracks in the raw TPC data and makes a determination of particle momentum and charge. The truncated mean energy loss $\langle dE/dx \rangle$ values (Section 2.3.2) are calculated for study at a later stage in the analysis.

A significant challenge for pattern recognition in the TPC data is the high particle multiplicity from heavy-ion collisions. Despite the dispersion of charged particles by the magnetic field, there are regions in each TPC with a high track density. Ionization from adjacent tracks may merge together and potentially skew or obliterate part of the track. This is seen near the front MTPC faces and the regions near the beam gap between the left and right MTPC. A large number of δ electrons are created from interactions with the TPC gas that leave behind tracks that further increase the amount of charge within the detector volume. Reconstruction inefficiencies resulting from these effects are compensated by correction factors that are described in Section 3.3.3.

Cluster Finding

The raw MTPC data can be visualized as a three dimensional array in pad, time, and padrow space in which each pixel element is integrated charge in the form of ADC output from readout electronics. The TPC ionization spatially diffuses as the electrons are transported to the readout plane. As a result, the ionization created across any padrow will extend transversely over several pads and timeslices,[7] forming a charge cluster.

The two dimensional clusters are found with a search algorithm that operates in two separate one dimensional operations. First, continuous groupings of signal are found in the time dimension for one pad at a time. Clusters are formed from the signal peaks close in time at adjacent pads. If the cluster spans at least two pads, the centroid of the cluster is extracted by a two dimensional Gaussian fit of the cluster. Otherwise, the cluster is rejected. No minimum cluster size in the time direction is required because the response of the shaper amplifier guarantees that the cluster extends across at least four timeslices. The clusters can then be used as points to form particle tracks.

The energy loss dE/dx is proportional to the total charge signal contained within the cluster. The dE/dx calculation is the sum of pad-timeslice signals and does not utilize the fitted cluster shape. The typical maximum ADC value within a cluster is around 70 ± 30 while the total charge is around 600 ± 250. The signal loss due to the threshold cut of 5 counts depends on the drift length because diffusion causes clusters

[6] The MTPC reconstruction program (MTRAC) was developed by S. Bailey and P. Venable (University of Washington), and S. Schoenfelder and P. Seyboth (MPI Munich).

[7] Diffusion also results in some electrons moving between neighboring padrows. Because the ionization is created in a continuous line, it is assumed that this will result in an overall zero-sum effect.

to widen. On average, the threshold cut removes 5% of the signal per meter of drift, but no correction is made for the signal loss.

Electronic noise, adjoining δ electrons, or merged clusters can result in a distortion of the point position and charge. If a cluster contains an overflow signal (ADC=255), it is discarded. The only intervening action taken to recoup damaged clusters is to split the cluster into two when there are two distinct signal peaks. The charge is simply divided between two new clusters at the minimum between the peaks while the point positions are determined from a center-of-gravity calculation.

Track Finding

Points are linked to form particle tracks. Track finding begins with sorting the points into a three dimensional array where each element corresponds to a padrow and a box in a remapped transverse x and y space. In this new transverse space, target vertex tracks are parallel and points from a single track are within a common transverse box coordinate $(x \pm \Delta x, y \pm \Delta y)$. Track pattern recognition comes from following points across padrows. Points cannot be shared between two tracks. The track search occurs over several passes, in which the starting padrow, an upstream or downstream search direction, and the transverse box size are varied. A track is formed by fitting the points within a box to a line. Only those points close to the fitted track, typically within 5 mm, are retained and then the track is refitted.

Charge, Momentum, and Mass Determination

The charge of a target vertex particle is determined from the magnetic field direction and which MTPC the particle was found in. It was assumed that all target vertex tracks found in one MTPC are from particles with the the same charge sign. On rare occasion, a particle with large p_T (> 1 GeV) opposite to the magnetic field bend ends up in the wrong detector.

A primary vertex particle has a trajectory that is unique to its initial momentum vector and charge. An initial momentum estimate was made from interpolating a value from a table of momenta and corresponding trajectories calculated from Chebyshev polynomials. Particles with the wrong charge sign for the detector will not be given a momentum assignment. Around 60% of all reconstructed tracks were determined to be from the target. The momenta of these tracks were then refined by an iterative procedure that uses Runge-Kutta integration to retrace the particle trajectory back through the magnetic fields to the target position.

Particle mass identification comes from the measurement of energy loss in the TPC gas (Section 2.3.2). Tracks in a small momentum range have truncated mean energy loss $\langle dE/dx \rangle$ values that are grouped according to particle mass.

Before the $\langle dE/dx \rangle$ calculation was performed, the cluster charge data were corrected for losses that occur during drift. Electron attachment results in a small charge loss of at most 2%. The 5 ADC count threshold imposed by the data aquisition system

causes an additional loss of 5% per meter of drift. The total observed losses are much larger than the sum of these two factors and have a dependence on track density. In the regions of highest track density, losses approaching 20% have been seen. It is now believed that the time response of the readout electronics is the source of the track density dependence of charge loss. Also, it has been discovered that the coupling of the anode wires to the pad plane did not have sufficient capacitance, resulting in additional signal loss. When the data for this work was analyzed, charge loss with drift length was removed by an empirical correction that was determined from a fit of the cluster dE/dx (renormalized for track momentum) dependence on drift length. Transverse momentum determines the vertical coordinate of a cluster and does not affect the dE/dx value appreciably. The variation in charge loss for individual events was not addressed by this correction.

Other corrections to the charge cluster data include the few percent variation in signal gain between readout electronics cards and pad and wire plane sectors that remain after on-line calibrations. A track dip angle or padrow crossing angle θ increases the measured dE/dx by $\cos(\theta)$ because of the longer path length across each padrow and is easily corrected for.

Ultimately, the $\langle dE/dx \rangle$ resolution determines the degree to which particle species can be separated. For example, negative charge hadrons with $3.8 < y_\pi < 4.0$ and $0.2 < p_T < 0.25$ (corresponding to a momentum range of $5.5 < p < 7.8$ GeV) forms a $\langle dE/dx \rangle$ distribution with a single peak. The K^- and $\bar{p}$ are not distinguishable from π^- in the h^- distribution. A fit of this distribution to a single Gaussian function gives a relative sigma of 5%. In Section 3.4, the $\langle dE/dx \rangle$ analysis method used to extract net protons will be discussed.

3.3.2 Track Selection

Quality criteria are imposed on the set of tracks in order to reject those tracks that are poorly reconstructed. The basic track properties are the potential length and the track length. The potential length of a track is calculated by the reconstruction software as being the maximum possible number of points on a track after accounting for the uninstrumented gaps between readout sectors. The track length is from the simpler calculation of the number of padrows spanned from the most downstream track point to the most upstream point.

Track distributions of potential length and track length are shown in Figure 3.3. Note that the track length can be greater than the potential length. This stems from the intersector gaps running along the longitudinal direction. A track crossing from one column of sectors to another column will lose a few points in the uninstrumented gap. The track length distribution is sharply peaked at the maximum length of 90 padrows, in contrast to the distribution of actual track points. Unreconstructed clusters can occur at random, reducing the number of track points and broadening the track point distribution. A properly reconstructed track should be close in length

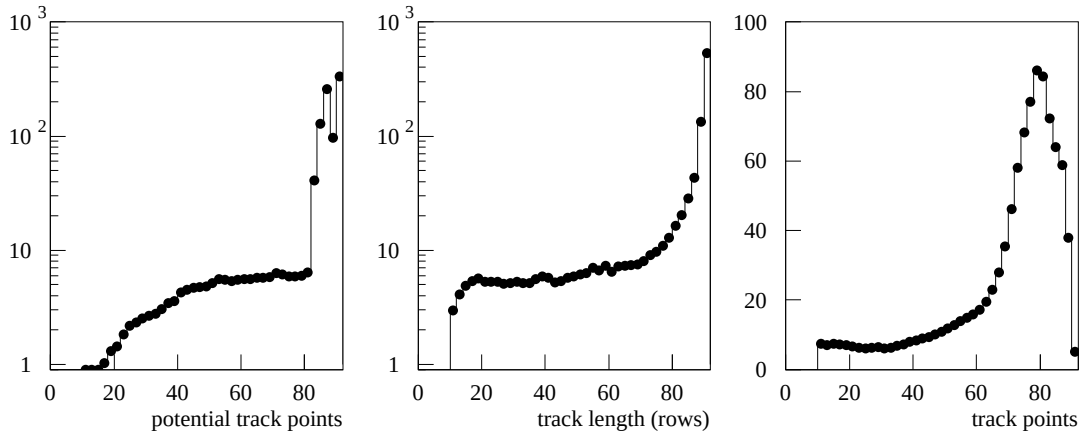

Figure 3.3: MTPC track distributions of potential number of points, track length (as defined by the number of padrows spanned from the first to last point), and actual number of points.

MTPC Track Quality Cuts	
	% remaining
target DCA: 3 cm	92
minimum length: $\geq$30 padrows	89
length to potential length ratio: 0.45	88
dE/dx points: 10	87

Table 3.1: The percentage of target vertex tracks remaining after imposing selection cuts. These numbers are nearly identical for both MTPCs. For tracks with 90 points, the maximum possible number, the truncated mean energy loss $\langle dE/dx \rangle$ is calculated from at most 50 dE/dx points.

to its potential length. In an extreme case, a track may be broken into two separate tracks and could be then counted twice. The length requirement cannot be too restrictive because in the region of high track density, especially near the front face of an MTPC, the upstream section of track may not be reconstructed.

Table 3.1 summarizes the various quality cuts imposed on tracks and the fraction of tracks remaining after each cut. To check the validity of the target vertex momentum assignment, the tracks were projected back upstream to the target starting along the fitted straight line trajectories in the MTPC. The paths within the magnetic field were determined using Runge-Kutta integration through the field map. A distance of closest approach (DCA) within 3 cm of the target vertex position was required in the transverse plane at the target z position. Most tracks had a DCA of less than 1 cm. The tracks that failed to pass this test also had a vertical vertex position beyond 3 cm from the target vertex and were likely from secondary processes. The

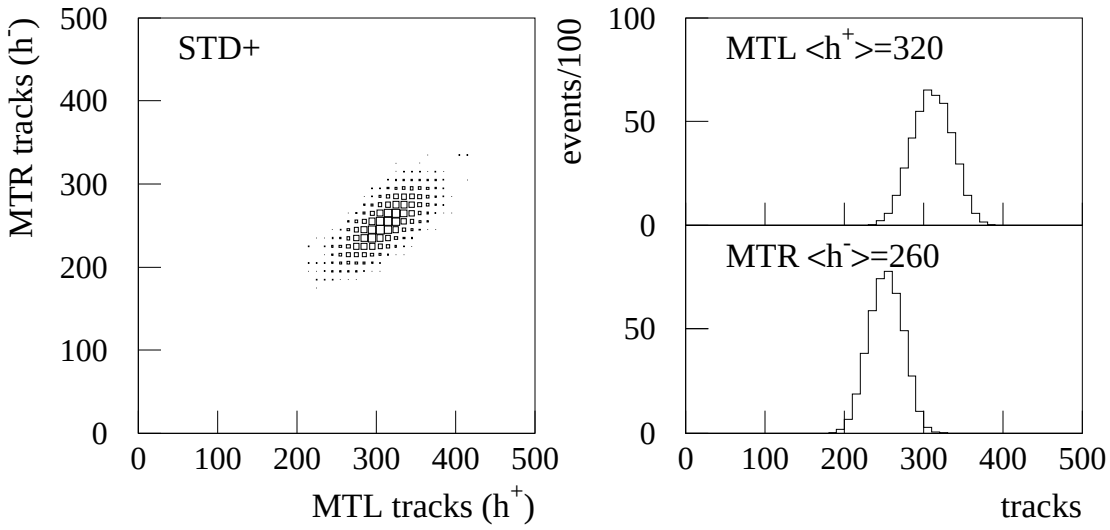

Figure 3.4: Target vertex track multiplicity per event detected with the MTPCs from central Pb+Pb collisions. The track quality cuts listed in Table 3.1 have been applied. The individual MTPC multiplicity distributions on the right are projections of the figure on the left.

next quality cuts involve the length of the track. The shortest tracks with a length of less than 30 padrows were removed. The length ratio is defined as the ratio of track length to potential track length. The minimum length ratio of 0.45 is equivalent to an effective length cut of 40 since most tracks have a length of around 90 padrows. This cut had a minor effect because the previous cut already removed most of these short tracks. Finally, the $\langle dE/dx \rangle$ had to be calculated from a minimum of 10 points. The $\langle dE/dx \rangle$ calculation (Section 2.3.2) excludes the highest 35% and lowest 10% of all dE/dx samples. For a track with 90 points, 50 points are used to determine $\langle dE/dx \rangle$.

The distribution of target vertex tracks per event in the MTPCs after all selection cuts is shown in Figure 3.4. More tracks are found in the Left MTPC, which measures positive charge particles, because of the net charge (+164) of the Pb+Pb system.

Although the central event trigger should select events with the highest possible track multiplicity, a very small fraction of events ($< 1\%$) have less TPC signal than the typical central event and a total of a hundred or fewer tracks. These events are the result from false triggers from a beam interaction between the MTPCs and the Veto calorimeter or a computational error during event reconstruction and are discarded.

3.3.3 Initial Corrections

Whenever tracks are removed from an event with the quality cuts described in this section, a measurement inefficiency occurs. Instrumental effects and high track density are other reasons for missing tracks and there are also sources of additional tracks

that are not from the primary Pb+Pb interaction. The effect from such losses and contributions is removed with correction factors calculated from event simulations. In the simulations, a model of the experimental apparatus is used to determine if particles can be detected. Simulated TPC data of tracks distributed according to the phase space distribution of negative charge hadrons are placed into real TPC data that acts as a realistic background. The entire embedded event is then reconstructed with the same software used by the normal data analysis. By comparing the simulation input to the reconstructed output, a quantifiable measure of the detector performance can be made. Appendix B contains a full account of the simulation techniques developed for this work.

Before the specific analyses to extract the $p-\bar{p}$ and h^- yields are performed, some preliminary corrections are applied to the data. These corrections are designed to compensate for the missing phase space coverage of the MTPCs and the loss of tracks due to detector response effects and the finite two track resolution. Additional corrections will be made to remove unwanted tracks that are not part of the intended measurement but remain in the analyzed data (Section 3.5).

Geometrical Acceptance

The strict definition of acceptance is whether or not a particle originating at the target vertex with a momentum vector $\vec{p}$ can be detected in the ideal case where the TPC charge environment is not a factor. A definition of what a detectable particle means must be made, such as the potential to create a TPC track with a minimum number of TPC points. When phase space is divided into very fine bins in (p_x, p_y, p_z) or some other space such as rapidity, transverse momentum, and transverse azimuthal angle ϕ, a precise map of acceptance can be made that sharply defines regions of complete acceptance and no acceptance.

In this work, the available computing time limited the statistics of the simulation and the phase space binning of acceptance had to be restricted to two kinematic variables, y and p_T. Consequently, the acceptance in this case has a fractional value. This poses a problem where the acceptance is changing rapidly, especially if the acceptance is going to zero. In those bins, the correction factors can introduce large uncertainties to the data.

The construction of a two dimensional acceptance correction requires that the inclusive p_T distributions be azimuthally symmetric. If a detector has acceptance limited to a small wedge in azimuth $\Delta\phi$, then the p_T dependence of the measured particle distribution must be the same for all azimuthal angles ϕ if the data are to be extrapolated to full phase space. The geometrical acceptance in y and p_T for protons and pions was shown in Figure 2.5. The azimuthal acceptance of pions as a function of p_T for several rapidity intervals was shown in Figure 2.6.

Tracking Inefficiency

While acceptance is in large part based on the geometrical properties of the detector, the overall event reconstruction performance also involves the physical response of the detector and the data analysis software. Inefficiencies result in a loss of accepted tracks that would otherwise be found in a perfect detector. The construction of the tracking inefficiency correction is simple in concept: it is the number of simulated particles that is accepted divided by the reconstructed yield. If only half of the simulated tracks are reconstructed, then the correction factor is 2.

Combined Correction

In practice, the acceptance and tracking inefficiency corrections are folded together into a single correction step because their definitions are not independent. The definition of acceptance as a minimum number of TPC points requires a calculation of the cluster reconstruction inefficiency. The combined correction is determined from the number of simulated tracks divided by the number of reconstructed tracks that are subject to the track quality criteria described in Section 3.3.2.

It is informative to see where acceptance falls away in phase space and how the tracking inefficiency changes with acceptance. Figure 3.5 shows the p_T dependence of acceptance and tracking efficiency (1−inefficiency) for protons in the Left MTPC for several intervals of rapidity. Both quantities are defined between 0 (no acceptance or zero efficiency) and 1 (100%) and the error bars are statistical from the calculation. Incorrectly reconstructed momenta may result in an efficiency greater than 1 in some bins. Broken tracks are unlikely with the track quality cuts used here. The tracking efficiency falls off where the acceptance drops, and at forward rapidities, where the track density is high. The scatter of the combined acceptance and inefficiency correction factors relative to a smooth fitted curve was used to estimate the systematic uncertainty of the correction.[8]

Not included in the estimate of tracking inefficiency is the effect from limited two track resolution because only single tracks were studied. If a simulated track was recovered with a $\langle dE/dx \rangle$ around twice the input value, then it was probably placed on top of an existing track. The relative number of the doubly ionizing tracks to singly ionizing tracks is a measure of the occupied space in the detector and was used to estimate the merged track losses. Figure 3.6 shows the fractional population of merged tracks as a function of rapidity. The number of measured singly ionizing tracks are increased by the correction factor to account for track merging.

Ghost tracks are a reconstruction artifact that are formed from unrelated clusters that appear to line up as a track. This situation is extremely rare except where the

[8] In hindsight, it would have been preferable to have smoothed the correction in y-p_T space and then assigned an error based on the scatter of original correction values relative to the smoothed values.

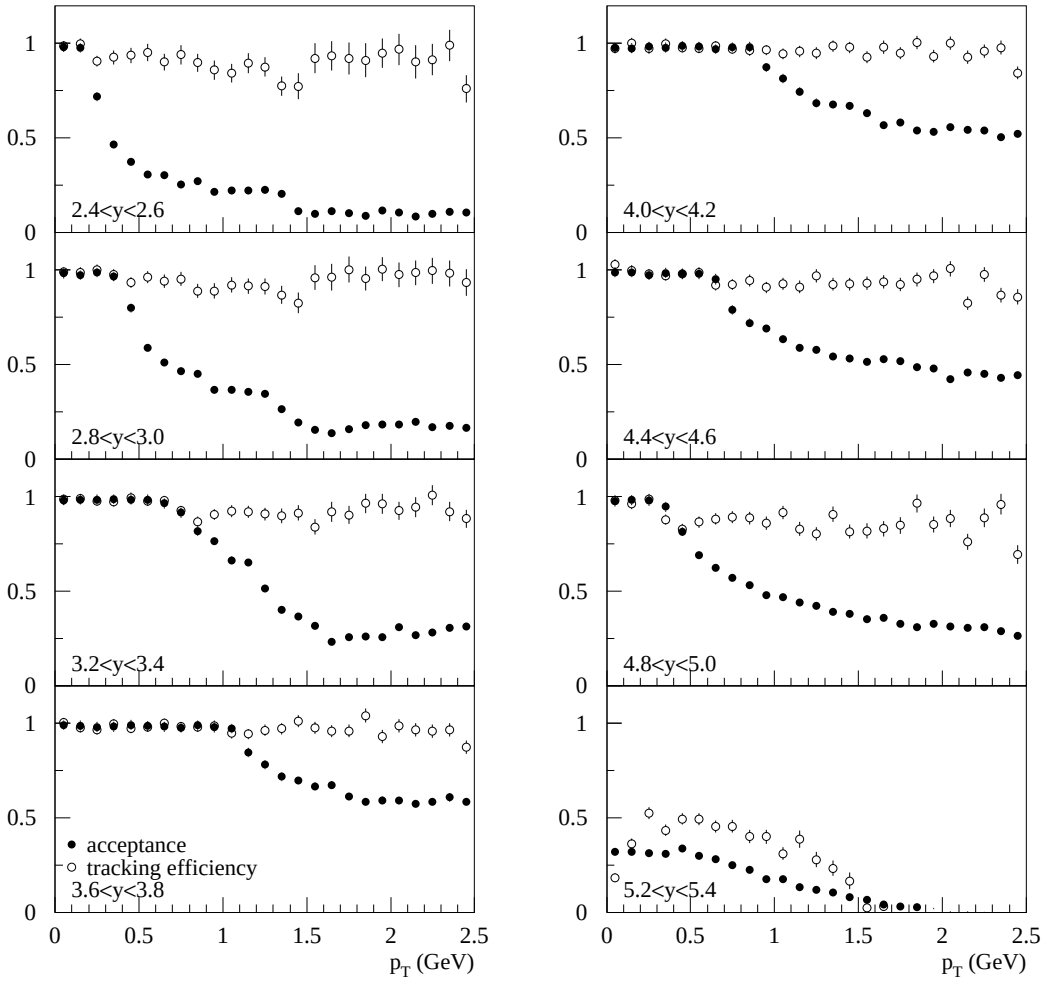

Figure 3.5: Left MTPC acceptance and tracking efficiency of protons for selected rapidity intervals. The tracking cuts are listed in Table 3.1. The combined correction factor for the data is 1/(acceptance×efficiency).

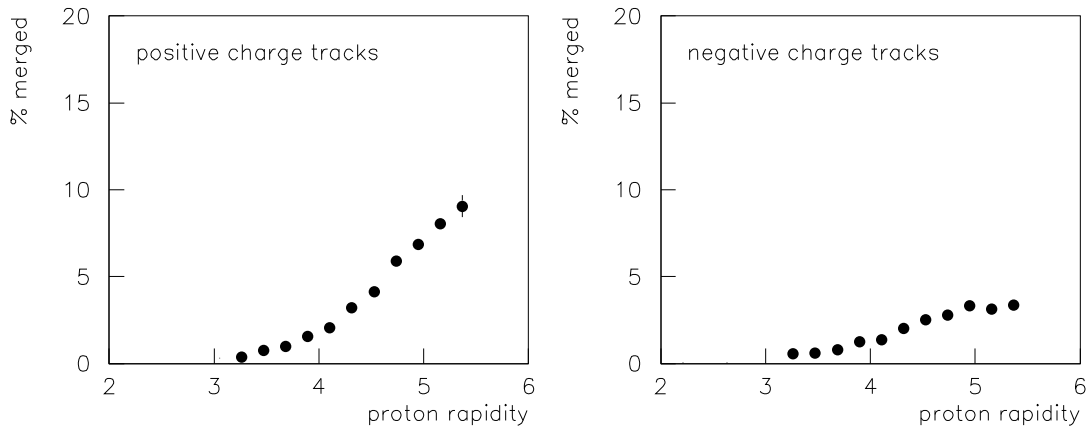

Figure 3.6: Percent of reconstructed tracks that are from two merged tracks as a function of proton rapidity. Note that at forward momenta, the protons in the positive charge tracks increase the track density and number of merged tracks.

track density is very high. This problem cannot become very large because points are not shared between tracks. Ghosts were factored into the secondary interaction background (Section 3.5), which turned out to be negligible.

3.4 Preliminary Particle Spectra

3.4.1 Net Protons

Net protons were found utilizing the $\langle dE/dx \rangle$ distribution of MTPC tracks. The track set was divided into phase space intervals with a width of 0.2 units of rapidity and 0.1 GeV in transverse momentum. Rapidity was calculated using the proton mass for all tracks. In each interval, a $\langle dE/dx \rangle$ distribution was created with a bin size of 2 ADC counts, which is 0.5% of the typical $\langle dE/dx \rangle$ value of 400 ADC counts. From the MTPC $\langle dE/dx \rangle$ study by Mock [77], there should be less than a $\sim \pm 1.5\%$ variation in proton $\langle dE/dx \rangle$ from the momentum range within any bin of this size.

The data were recorded during sequential eight hour periods. Because of atmospheric pressure changes, the average $\langle dE/dx \rangle$ from each data set varied run to run by as much as 5%. The track $\langle dE/dx \rangle$ were rescaled so that every data set had the same average $\langle dE/dx \rangle$ value. The positive and negative track data were rescaled separately.

Figure 3.7 shows the $\langle dE/dx \rangle$ spectrum of tracks in the range $2.8 < y < 3.0$ and $0.3 < p_T < 0.4$. The left shoulder of the h^+ distribution comes from p and K^+. The contribution from $\bar{p}$ and K^- to the h^- is small and is not prominent in the $\langle dE/dx \rangle$ distribution. After subtracting the h^- from the h^+ $\langle dE/dx \rangle$ distribution, the net protons are visible as a peak. The Pb+Pb system has a large net isospin and some of

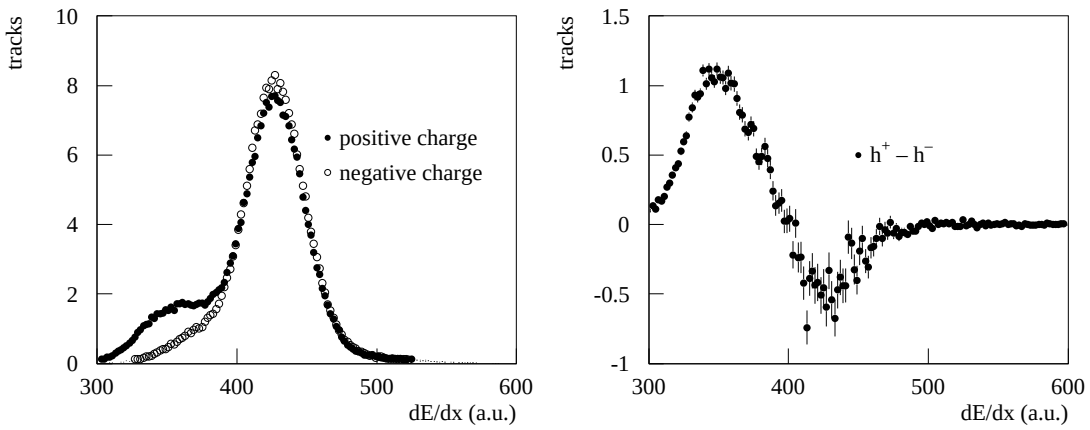

Figure 3.7: The left figure shows the individual dE/dx distributions for h^+ and h^- in the range $2.8 < y_p < 3.0$ and $0.3 < p_T < 0.4$ GeV/c. The difference $h^+ - h^-$ is shown on the right. The vertical scale is given in the number of tracks per 2 unit $\langle dE/dx \rangle$ bin. Errors are statistical.

the isospin is carried off in the final state by π^-.[9] This is why the $\pi^\pm$ peaks in Figure 3.7 are not identical and the $h^+ - h^-$ difference has a net pion peak with a negative amplitude.

The $h^+ - h^-$ distributions were simultaneously fit by two Gaussian functions to extract the net proton and net pion yields. The fitted $p - \bar{p}$ yield includes some fraction of the kaon difference $K^+ - K^-$ because the kaon $\langle dE/dx \rangle$ falls between the proton and pion $\langle dE/dx \rangle$. This residual content is corrected for at a later stage.

As was demonstrated in Figure 3.6, tracks with twice the typical hadronic $\langle dE/dx \rangle$ value form only a small fraction of all tracks except at forward rapidities. These doubly ionizing tracks are the result of two merged particle tracks and are counted as two protons or antiprotons in the analysis. This is a reasonable assumption at high rapidities, where the majority of measured charged particles should be protons.

An important systematic error in this analysis method can arise from mismatched energy loss amplitudes from the two MTPCs. To address this problem, the h^- $\langle dE/dx \rangle$ distribution was shifted so that its π^- peak is aligned with the π^+ peak of the h^+ distribution. The number of pions, resolution of the $\langle dE/dx \rangle$ measurement, and the finite $\langle dE/dx \rangle$ bin size limit the precision to which the two distributions can be matched. The uncertainty of the measured net proton yield was studied by systematically shifting the h^- distribution relative to the h^+ distribution before the $h^+ - h^-$ analysis was performed. A variation in yield up to 10% was observed.

Ideally, the $\langle dE/dx \rangle$ value should be a smooth, continuous function of total momentum. The $\langle dE/dx \rangle$ of net protons in every (y, p_T) bin is plotted as a function

[9] If all net isospin is found in charged pions, then $2 \times (126 - 82) = 88$ more π^- than π^+ will be produced.

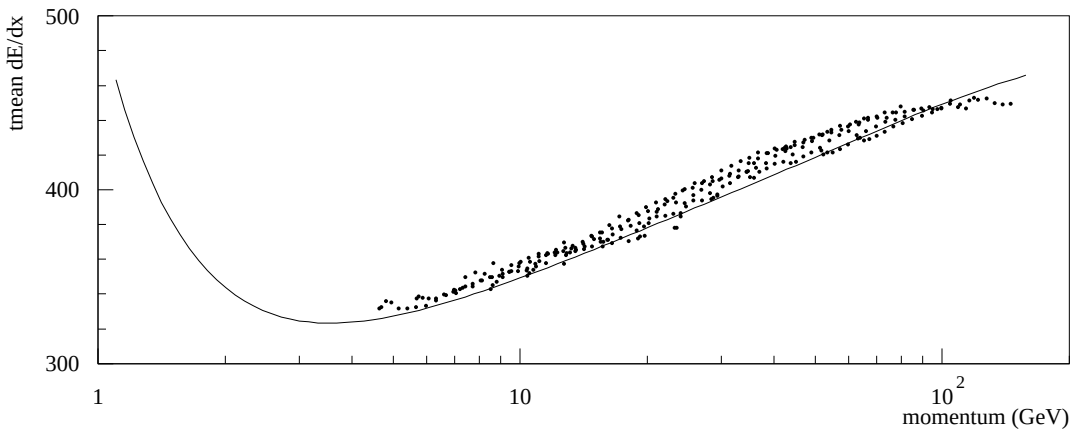

Figure 3.8: The fitted truncated mean dE/dx as a function of momentum for net protons. Each point corresponds to the momentum at the center of a (y, p_T) bin. The $\langle dE/dx \rangle$ curve is from a parameterization by Mock [77].

of total momentum in Figure 3.8. Different (y, p_T) bins overlap in total momentum. When there are two points with the same momentum value, the point at higher p_T also had a greater $\langle dE/dx \rangle$ value. This behavior is possibly due to residual $K^+ - K^-$ that shifts the fitted $\langle dE/dx \rangle$. However, the analysis method does not require a highly precise $\langle dE/dx \rangle$ resolution; the primary goal is to remove the contribution from pions. If the $\langle dE/dx \rangle$ behavior of the positive charge tracks and negative charge tracks are similar, satisfactory results can be achieved.

Because the $\langle dE/dx \rangle$ analysis method uses data from both the Left and Right MTPCs at the same time, a bias may be introduced when only one magnetic field setting is used. Figure 3.9 shows rapidity distributions of $h^+ - h^-$ from the $STD+$ and $STD-$ data sets.[10] The data shown are simply from the difference between all positive charge and negative charge tracks. No $\langle dE/dx \rangle$ information was used. The small difference seen between the two rapidity distributions can be attributed to a slight difference in the event trigger, and the data from the two field settings are consistent within this uncertainty.

3.4.2 Negative Charge Hadrons

The negative charge hadrons are found by counting tracks from a single MTPC. The phase space distribution was formed by sorting the track data into bins with a width of 0.2 units of rapidity and 0.1 GeV in transverse momentum. Rapidity was calculated

[10] This charge difference analysis [30], called "plus minus minus", has been used to measure net protons when particle identification is not possible. In the case of Pb+Pb collisions, the net isospin of the system results in more π^- than π^+ and makes this method dependent on a large pion correction.

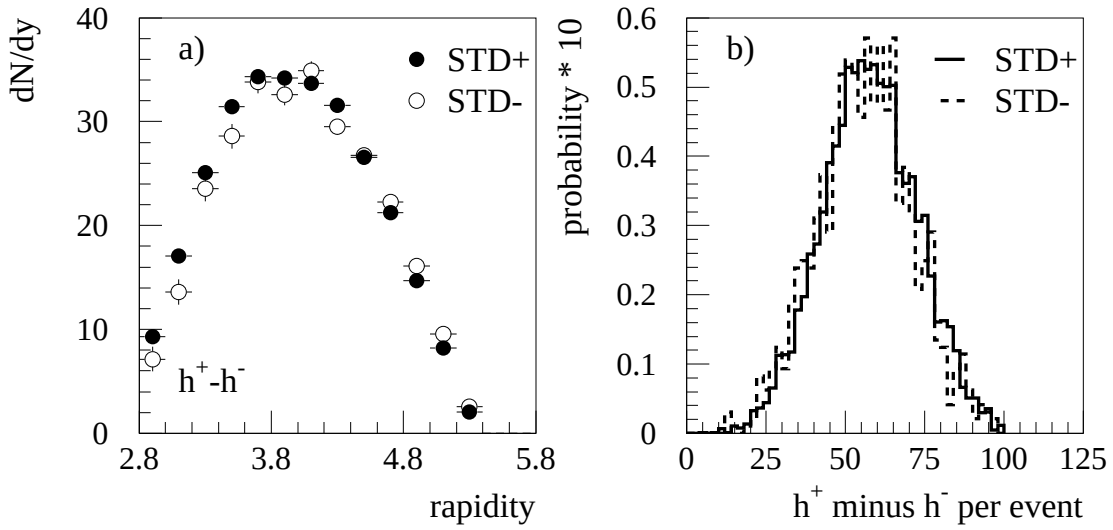

Figure 3.9: (Left) Uncorrected rapidity distributions, assuming a proton mass, of the difference between positive and negative charge particles from data taken with the $STD+$ and $STD-$ magnetic field settings. (Right) The yield of $h^+ - h^-$ per event. The distribution is renormalized to a total integral of 10, and each bin is two counts wide.

using the pion mass for all tracks.

Only those tracks with a right side p_T (azimuthal angle $|\phi| < 90°$, $\phi = 0 \equiv -\hat{x}$) were used because a higher level of background from secondary vertex tracks occurs with reconstructed wrong side p_T than right side p_T (Section 3.5). It was observed in the data that the electron content of right side tracks, identified by $\langle dE/dx \rangle$ value, was at most 1% in any (y, p_T) bin. A stricter right side definition of $|\phi| < 45°$ did not improve the data quality.

3.4.3 Rapidity Distributions

The preliminary rapidity distributions of $p - \bar{p}$ and h^-, corrected for acceptance and tracking inefficiency, are shown in Figure 3.10. For the extrapolation of h^- with right side p_T to full p_T azimuth, it is assumed that the right side and wrong side distributions are identical. The h^- yield drops off below $y \sim 3.8$ because the acceptance at low p_T steadily worsens in this region. (The pion acceptance is shown in Figure 2.5.) Net proton data extend down to zero p_T in the rapidity range $2.2 < y < 5.4$.

3.5 Background Corrections

The preliminary determination of net protons and negative hadrons contains background tracks from secondary verticies. In the case of the net protons, there is also

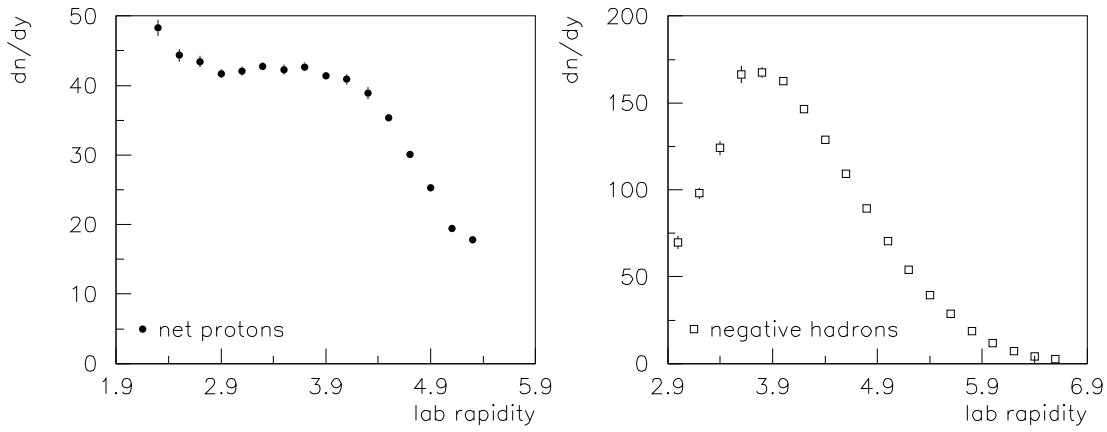

Figure 3.10: Preliminary particle spectra, corrected only for acceptance and tracking inefficiency. Statistical errors shown only. (Left) Net proton rapidity distribution. (Right) Negative charge hadron rapidity distribution. Below $y_\pi = 3.8$, the yield is limited by the complete absence of acceptance at low p_T.

a contribution from $K^+ - K^-$. The level of background is calculated with Monte Carlo simulations (Appendix B) using particle distributions from experimental measurements where available and event models otherwise. The background correction factors are scaled by the acceptance and tracking inefficiency corrections and then applied to the data to create the final particle spectra.

Particles from secondary interactions in detector material form one component of the background. Most electrons are not included in the data set because multiple scatterings in the TPC gas cause large deflections and the resulting crooked tracks are not reconstructed. Highly energetic electrons (> 1 GeV) have a higher $\langle dE/dx \rangle$ value than hadrons and can be rejected on this basis. Less than 1% of the h^- tracks appeared to be electrons. Simulations using events from the VENUS model indicated that the majority of MTPC tracks from hadronic background are reconstructed as non-target tracks. Restricting the selection of tracks in the h^- analysis to right side p_T reduced the background by over factor of two to less than 5% of the signal (Section 3.4.2). Most of the hadronic background in the $p-\bar{p}$ measurement appears at a $\langle dE/dx \rangle$ above that of a proton. Also included in the background are artificial ghost tracks formed from unrelated clusters in the regions of high track density . Because the secondary interaction background is relatively small compared to the particle distributions of interest, a very large number of simulated events is needed to produce a statistically stable estimate of the correction factors. No correction was applied to either the $p-\bar{p}$ or h^- data.

The dominant source of background is from strange hadrons that decay weakly to charged particles. A significant fraction of strange baryons and K^0_S decay within the 9 meters of flight path between the target and the MTPCs. A charged decay

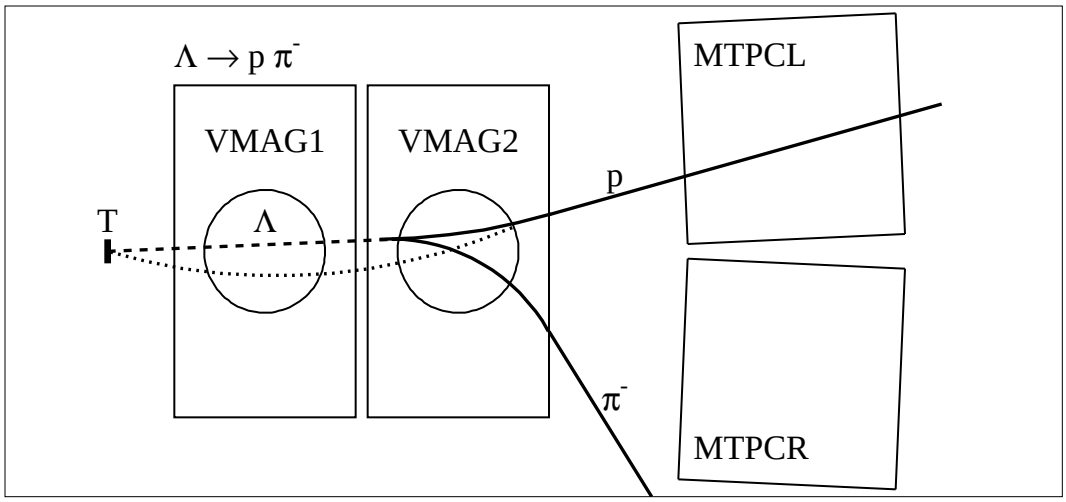

Figure 3.11: A proton from the decay of a Λ (dashed line) that is detected in an MTPC can appears to originate at the target (dotted line).

daughter that creates a TPC track can appear to originate at the target vertex. An illustration in the bend plane of a $\Lambda \rightarrow p\pi^-$ decay is shown in Figure 3.11. Because the proton is much heavier than the pion, the proton from Λ decay carries off most of the momentum. The pion is often emitted at a large angle and does not enter into an MTPC.

Multistrange baryons such as the Ξ and Ω can decay to a Λ. Their maximum contribution to the net protons can be estimated by the following argument. Based on the relative production at midrapidity of Ξ and Ω to Λ in central Pb+Pb collisions[11] and assuming that all multistrange baryons immediately decay to Λ, that all proton daughters from Λ are reconstructed as target vertex particles, and that there are an equal number of p and Λ, the number of protons from strange baryon decay increases by 7% over the number from primary Λs alone. The actual contribution from multistrange baryons will be much smaller than 7% because the lifetime of the multistrange baryons will displace the decay verticies farther downstream, decreasing the likelihood that the decay proton will be mistaken for a primary particle. No correction was calculated for this effect because the phase space distributions of multistrange baryons have not been fully measured.

Charged kaons are removed from the $p-\bar{p}$ data, but are a part of the h^- measurement and are not corrected for. A small fraction of charged kaons decay to pions before reaching the MTPC, but the change in direction between the kaon and pion is usually small enough so that the pion trajectory is indistinguishable from the trajec-

[11] See footnote 1 in this chapter.

tory that the kaon would have followed had it not decayed. A negligible number of additional kaons comes in the form of K^+K^- pairs from Φ meson decays.[12]

3.5.1 Corrections to Net Protons

The secondary vertex background correction is for the decay of net $\Lambda+\Sigma^0$ and $\Sigma^+-\bar{\Sigma}^-$. Σ^- decays to a neutron and π^- and is not a factor because reconstructed secondary pions are rejected by the $\langle dE/dx \rangle$ analysis.

The K^+-K^- correction was calculated from a simulated $\langle dE/dx \rangle$ distribution based on a parameterization of $\langle dE/dx \rangle$ as a function of velocity [77] and phase space distributions of p, $\bar{p}$, $K^{\pm}$, and $\pi^{\pm}$ from the RQMD model. For every (y_{proton}, p_T) bin, a $\langle dE/dx \rangle$ distribution of h^+-h^- was created from a Gaussian $\langle dE/dx \rangle$ distribution with a 6% relative width for each particle species. A procedure identical to the data analysis was performed and then the fitted $p-\bar{p}$ yield was compared to the input $p-\bar{p}$ yield to determine the contribution from K^+-K^-. In order to make the estimated correction independent of the input kaon distribution, the relative correction factors were calculated. The nominal correction was found to be $(75\pm14)\%$ of the K^+-K^- difference for all (y, p_T) bins. A further discussion on the corrections will be presented in Section 3.5.3.

3.5.2 Corrections to Negative Charge Hadrons

The primary source of background is from the decay of K^0_S to $\pi^+\pi^-$. Pions from strange baryon decay form a small fraction of the background because the heavier baryon daughter carries away most of the total momentum and the low momentum pions are swept away from the MTPC by the magnetic field. Strange baryons that can contribute decay daughters to the measured h^- include the Λ (decaying to π^-), $\bar{\Lambda}$ ($\bar{p}$), $\bar{\Sigma}^-$ ($\bar{p}, \pi^-$), and Σ^- (π^-). A further discussion on the corrections will be presented in Section 3.5.3.

3.5.3 Strangeness Corrections

Whenever possible, experimental data should be used for the calculation of the strangeness based corrections. For the h^- analysis, K^0_S have been measured with VTPC2 and MTPC [94]. Figure 3.12 shows the correction for K^0_S decay. Charged kaons have been measured with the MTPC[13] [99] and TOF [94]. The K^+-K^- distribution is shown in Figure 3.13 along with the distributions from the RQMD and

[12] There are about 6 Φ created per central Pb+Pb collision [98].

[13] The MTPC charged kaon analysis is based on finding the small fraction of kaons that decay into pions within the detector and does not use the $\langle dE/dx \rangle$ information from the tracks.

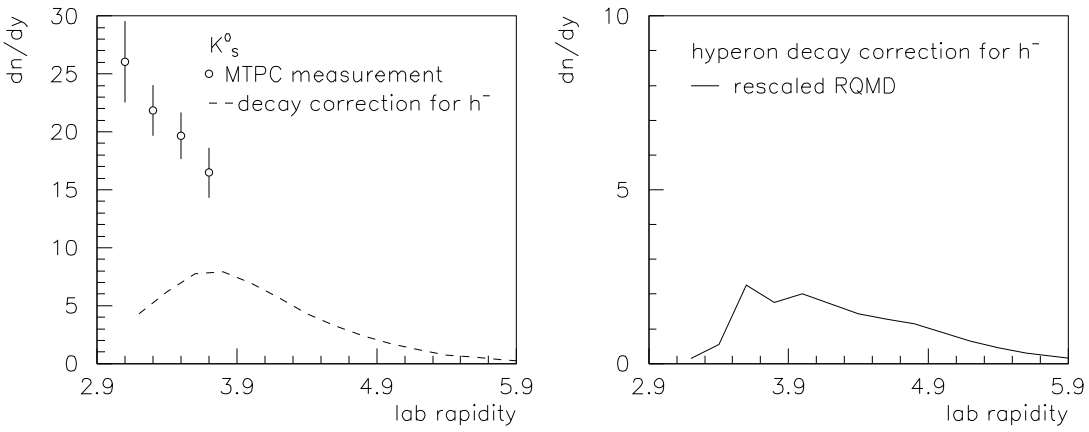

Figure 3.12: Background corrections for h^-. (Left) K^0_S rapidity distribution from central Pb+Pb collisions as measured with the NA49 MTPC and the resulting decay correction for h^- from a parameterization of the data. (Right) Hyperon decay corrections for h^- based on the RQMD model.

VENUS models for comparison. The data were parameterized by fitting the MTPC rapidity distribution to a Gaussian function and rescaling the distribution so that the midrapidity yield matched that from the TOF measurement. The widths of the fitted kaon distributions are $\sigma_{K^+} = 0.77$ and $\sigma_{K^-} = 0.85$. Figure 3.13 also shows the data-based correction for the net protons.

The NA49 lambda measurements from VTPC2 were made over the limited rapidity range of $2 < y < 3$ and are in a preliminary state [94]. The distribution has a sharp peak at midrapidity that is possibly the result of an underestimate of the reconstruction efficiency and feeddown from Ξ decaying to Λ. A fit of the data to a Gaussian function gives a sigma of 0.8. In contrast, the RQMD and VENUS models predict a wide and flat rapidity distribution. Figure 3.14 shows the net $\Lambda + \Sigma^0$ rapidity distributions from experimental data and event models. As was discussed in Section 3.1.1, both postive and negative charge Σ rapidity distribtions are assumed to be identical to the Λ distribution after scaling by a factor of 0.3. Given the uncertainties of the net Λ distribution, the systematic effects on the net proton and net baryon distributions from the variation of corrections based on data and models were studied.

The $K^+ - K^-$ and strange baryon decay corrections to the net proton data are related through the overall zero strangeness content the system. When an $s\bar{s}$ quark pair is formed, the s quark likely appears in a Λ while the $\bar{s}$ is found in a K^+ because the system is composed mainly of u and d quarks. Therefore $K^+ - K^-$ have a net strangeness $S > 0$ while net lambdas have $S < 0$.[14] The net strangeness of $K^+ - K^-$ and net lambdas do not cancel because other strange hadrons are produced.

[14] The s quark has strangeness $S = -1$

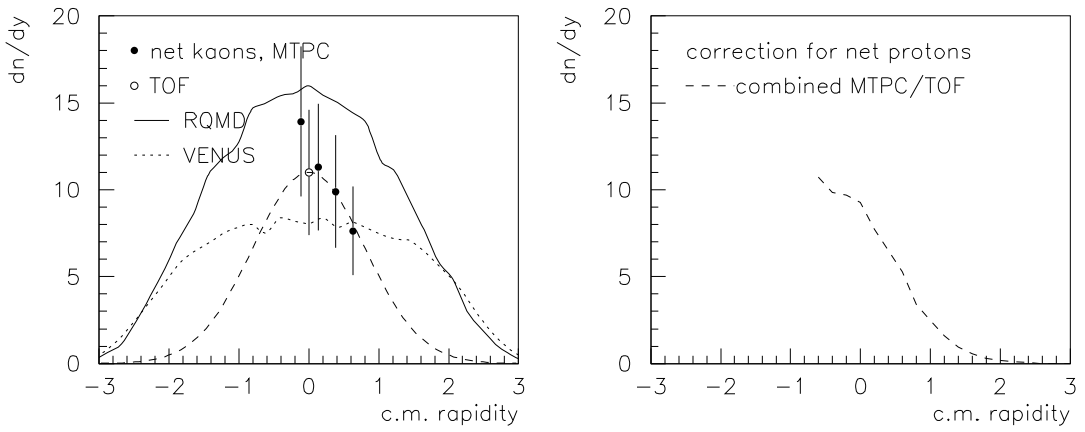

Figure 3.13: (Left) Net kaon $K^+ - K^-$ rapidity distributions from central Pb+Pb collisions, as measured with the NA49 MTPC and TOF, and from the RQMD and VENUS models. A Gaussian distribution fitted to the combined NA49 data is shown as a dashed line. (Right) The dashed line shows the derived $K^+ - K^-$ correction to the net proton distribution.

The balance of net strangeness carried by charged kaons and net strange hyperons $Y - \bar{Y}$ can be described with the ratio

$$R_s = \frac{K^+ - K^-}{Y - \bar{Y}}. \tag{3.4}$$

RQMD predicts a strangeness ratio of $R_s = 0.6$, while VENUS predicts $R_s = 0.67$. From NA49 data,[15] $R_s = 0.38$, which means that there are many more Λ and Σ in the data relative to kaons than what is predicted by either model. This presents a potential problem if the $K^+ - K^-$ correction is based on data while the strange baryon decay correction is based on a model.

RQMD and VENUS are able to reproduce the strange particle spectra from central S+S collisions at 200 GeV per nucleon and their predictions for the Pb+Pb system involve no new physics for the heavier system. Assuming that strangeness production does not change dramatically from S+S to Pb+Pb collisions beyond what is expected from wounded nucleon scaling, the R_s values from the models will be used as a standard rather than what is found in the preliminary NA49 measurements.

When R_s is calculated from the NA49 kaons and the RQMD net hyperons, the result is $R_s = 0.27$. If the VENUS net hyperons are used, $R_s = 0.47$. The hyperon yields from NA49 data, RQMD, and VENUS must all be rescaled so that the net strangeness carried by the hyperons is consistent with the net strangeness of $K^+ - K^-$. Otherwise, the hyperon decay corrections for $p - \bar{p}$ and h^- data will be too large to be consistent with the model predictions of strangeness conservation.

[15] The charged Σ are extrapolated from the measured Λ with Equation 3.2.

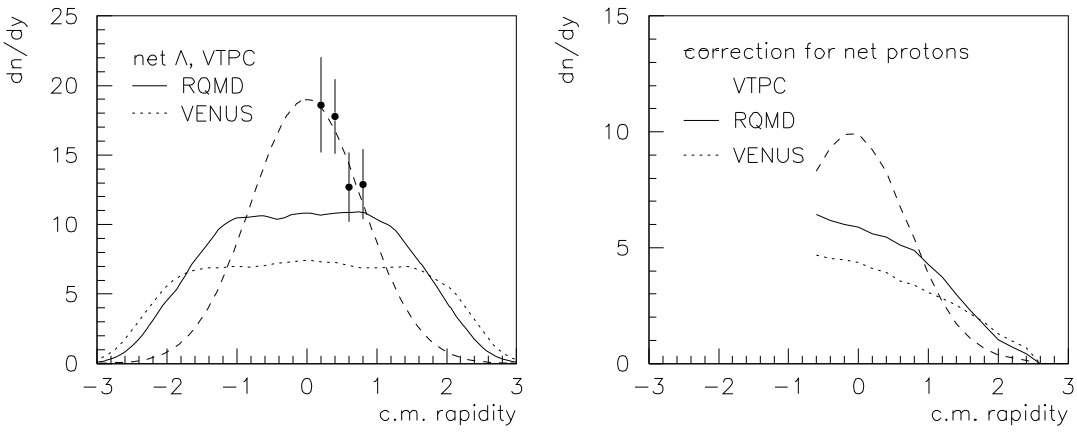

Figure 3.14: (Left) Net $\Lambda + \Sigma^0$ rapidity distributions from central Pb+Pb collisions, as measured with the NA49 VTPC2 and predictions from the RQMD and VENUS models. A fitted Gaussian distribution to the NA49 data is also shown. (Right) Net Λ correction to the net protons measurement for the three net Λ sources after rescaling for strangeness conservation.

R_s is fixed to a value of 0.635, which is between the RQMD and VENUS numbers. The hyperon rescaling factors are as follows: 0.60 for the NA49 data, 0.43 for RQMD, and 0.74 for VENUS. The $p-\bar{p}$ corrections are shown in Figure 3.14 and the h^- corrections are shown in Figure 3.12. Because the hyperon decay corrections for h^- are relatively small, only the RQMD-based calculations were used in the analysis.

3.5.4 Statistical and Systematic Errors

The statistical errors of the experimental data are determined from Poisson statistics because the tracks are counted inclusively and then event normalized. The $\langle dE/dx \rangle$ analysis method used to extract the net proton yield introduces a systematic error on the order of 10%.

The statistical errors of the correction factors for acceptance and tracking inefficiency, and for background particles are calculated in the same manner as the errors of the data distributions. The simulated tracks are counted inclusively and for a sufficiently large sample (> 100) in a phase space bin, a correction factor is determined.

When a parameterized phase space particle distribution is used to calculate data corrections, the uncertainties of the binned correction factors may be correlated in rapidity and transverse momentum. For example, the NA49 K^+-K^- rapidity distribution has an uncertainty in yield of nearly 25%. This uncertainty is propagated through to the final $d^2n/dydp_T$ and dn/dy spectra.

Chapter 4

Charged Particle Spectra

4.1 Introduction and Overview

Event-normalized, inclusive rapidity and transverse momentum distributions of net protons ($p-\bar{p}$), net baryons ($B-\bar{B}$), and negatively charged hadrons (h^-) from central Pb+Pb collisions at a beam energy of 158 GeV per nucleon will be presented and interpreted in the context of proton and baryon stopping, particle production, and transverse radial flow. A key aid to understanding the data will be the comparison of the results to data from central S+S collisions at 200 GeV per nucleon that have been reported by the CERN experiments NA35 [29, 30, 31, 32] and NA44 [97, 100]. These comparisons reveal slightly greater stopping and flow in the heavier system, along with new features in the transverse momentum spectra that will be described.

At CERN-SPS energies, baryon stopping increases from the light S+S system to the heavier Pb+Pb system. While the baryon population around midrapidity is larger in the Pb+Pb data, this does not have a major effect on the average energy loss per baryon, which is similar in both systems. The rapidity distributions of produced negative hadrons, adjusted for the number of participating nucleons in the collision, are nearly identical. While the negative charge hadrons do not represent all particle production, this observation is consistent with the comparable energy loss per participant in the two systems.

Rapidity distributions reflect the longitudial motion of the system. The increased baryon stopping seen in the Pb+Pb collisions may be accompanied by an increase of transverse momentum carried by the net baryons. Significant differences in the p_T spectra between the S+S and Pb+Pb systems can in fact be seen. While the mean transverse momentum $\langle p_T \rangle$ carried per proton increases with system size, the $\langle p_T \rangle$ of the lower mass negative hadrons appears to be independent of system size. It has been demonstrated elsewhere that the S+S p_T spectra are consistent with a conjecture that the average transverse radial flow velocity is the same for all particles [27, 51, 52]. The Pb+Pb data also exhibit the behavior of transverse radial flow. Furthermore, the magnitude of flow appears to be greater in the Pb+Pb system, which follows a systematic trend of increasing transverse radial flow with system size [97].

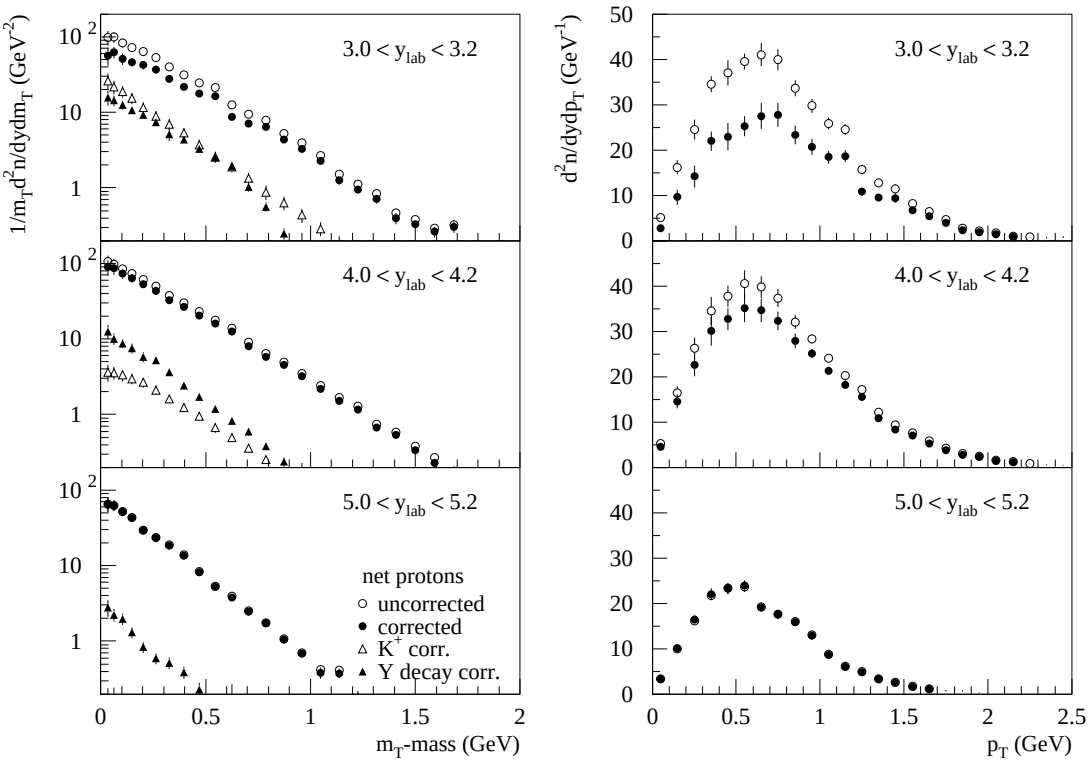

Figure 4.1: Net proton m_T (left) and p_T (right) spectra. Also shown are the uncorrected data and the corrections for $K^+ - K^-$ and $\Lambda + \Sigma$ decay.

The complete net proton, net baryon, and negative charge hadron data are presented in tables of numerical $d^2n/dydp_T$ and dn/dy values in Appendix C.

4.2 Particle Distributions

4.2.1 Net Protons and Net Baryons

Transverse Spectra

Net proton p_T and m_T spectra from selected rapidity intervals are shown in Figure 4.1. The systematic errors from the dE/dx analysis method and correction factors are included. Also shown in the figure are the uncorrected data and the corrections for $K^+ - K^-$ and $\Lambda + \Sigma$ decay, which become negligible with increasing rapidity.

Figure 4.2 shows the rapidity dependence of the mean transverse momentum $\langle p_T \rangle$. The decrease of $\langle p_T \rangle$ as rapidity increases is attributable to energy conservation. In hadron+hadron collisions, there is a kinematic limit imposed by the momenta of the colliding particles. Collective effects in nucleus+nucleus collisions may increase this

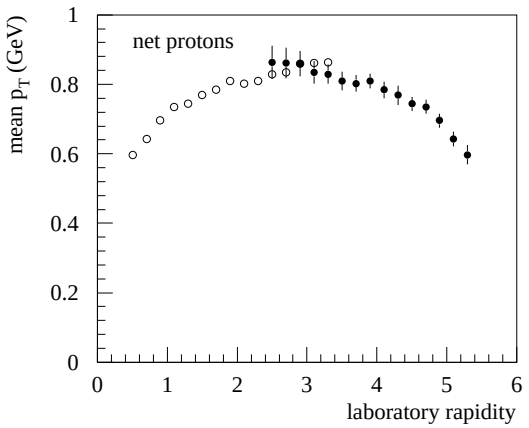

Figure 4.2: Net proton mean transverse momenta $\langle p_T \rangle$ are shown as solid circles. The open symbols are the data reflected about midrapidity $y_{lab} = 2.9$, and the error bars have been omitted.

limit. However, the $\langle p_T \rangle$ is non-zero at beam rapidity due to the Fermi momentum of projectile fragments. Although the data were analyzed only up to $p_T = 2.5$ GeV, an extrapolation of the p_T spectra to the nucleon+nucleon collision kinematic limit by fitting the p_T tail to Equation A.10 results in an increase of $\langle p_T \rangle$ by 2% at most, which is not significant. Below midrapidity, there is a slight systematic increase in $\langle p_T \rangle$ that is due to the relatively large corrections applied to the data.

Rapidity Spectra

Net protons are measured down to $p_T = 0$ and their rapidity distribution dn/dy can be determined by integrating the measured p_T data without extrapolation. The contribution to the yield from protons with $p_T > 2.5$ GeV is negligible. The net proton rapidity distribution is shown in Figure 4.3. The error bars include the estimated systematic errors from the $\langle dE/dx \rangle$ analysis method and the corrections for $K^+ - K^-$ and tracking inefficiency.

An uncertainty in the $p - \bar{p}$ data is from the $\Lambda - \bar{\Lambda}$ distribution used to estimate the hyperon decay correction. The symbols in Figure 4.3 show the data corrected with RQMD-based hyperons. The RQMD $\Lambda - \bar{\Lambda}$ rapidity distribution is shown as the solid line. The figure also includes the $\Lambda - \bar{\Lambda}$ distributions from the preliminary NA49 measurement and the VENUS model. The $p - \bar{p}$ distributions from corrections calculated using these alternative $\Lambda - \bar{\Lambda}$ are shown as a dashed line for VENUS and a dotted line for NA49. These lines connect dn/dy values and are not smoothed.

The effect on $B - \bar{B}$ from net lambdas is very small because the uncertainty of $p - \bar{p}$ from the correction for feeddown protons from $\Lambda - \bar{\Lambda}$ decay is balanced by the

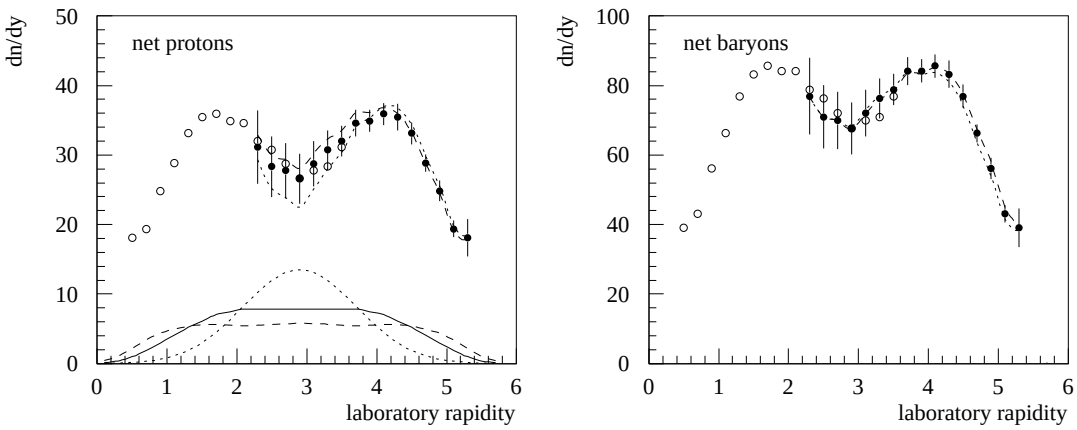

Figure 4.3: Net proton (left) and net baryon (right) rapidity distributions corrected for $\Lambda + \Sigma$ decay using the RQMD model. The open symbols are the data reflected about midrapidity without error bars. Net lambda distributions from NA49 (dotted line), RQMD (solid line), and VENUS (dashed line) are shown with the net protons. The lines drawn around the data points indicate the effect on the data when the strange baryon decay correction is based on NA49 data or VENUS.

subsequent addition of $\Lambda - \bar{\Lambda}$. This situation arises because the fraction of lambdas that decay and contribute to the measured protons is close to the $\Lambda \rightarrow p$ branching ratio (0.64), and the scaling factor used to extrapolate $\Lambda - \bar{\Lambda}$ to all $S = -1$ hyperons is 1.6. From the definition of the $B - \bar{B}$ estimate originally given in Section 3.1.1,

$$B - \bar{B} \ = (2.07 \pm 0.05)(p - \bar{p}) + (1.6 \pm 0.1)(\Lambda - \bar{\Lambda}), \tag{4.1}$$

and assuming that net Λ and net Σ^+ contribute according to their branching ratios to the measured, uncorrected net protons $p_m - \bar{p}_m$, then

$$B - \bar{B} \ \approx 2((p_m - \bar{p}_m) - 0.64(\Lambda - \bar{\Lambda}) - 0.54(\Sigma^+ - \bar{\Sigma}^-)) + 1.6(\Lambda - \bar{\Lambda}), \tag{4.2}$$

$$B - \bar{B} \ \approx 2((p_m - \bar{p}_m) - (0.64 + 0.54 \times 0.3)(\Lambda - \bar{\Lambda})) + 1.6(\Lambda - \bar{\Lambda}), \tag{4.3}$$

$$B - \bar{B} \ \approx 2(p_m - \bar{p}_m). \tag{4.4}$$

Equation 4.1 has been applied to particle distributions from the RQMD and VENUS models. For both models, the distributions of "true" and calculation-based net baryons are virtually indistinguishable.

Participant Number

Collision participants are defined as those initial nucleons that interact inelastically. Conversely, spectators are nucleons that survive intact either as individual nucleons or bound into heavier fragments. The final state net baryons away from beam or target rapidity can be counted to determine the number of participants. The symmetry

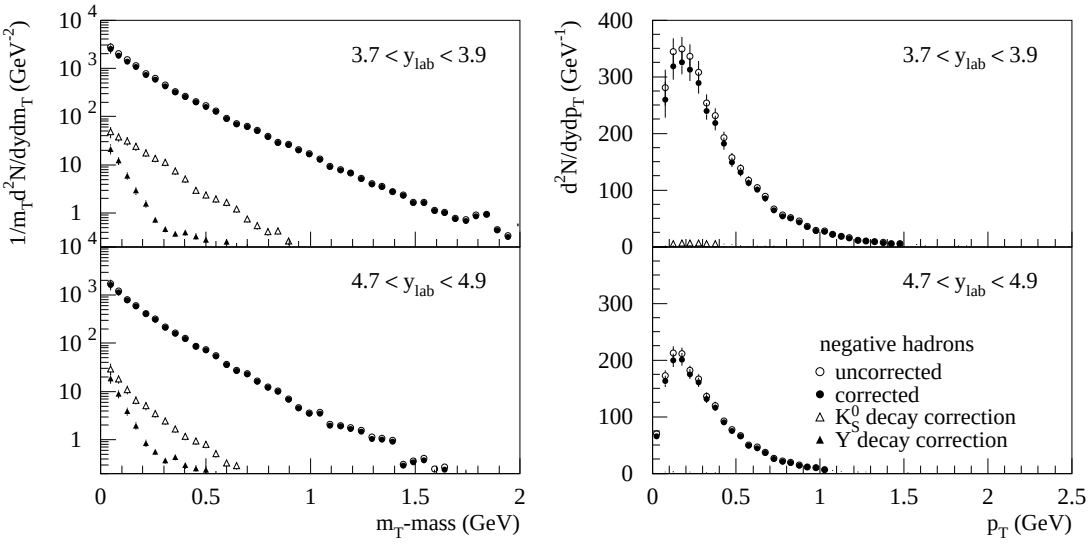

Figure 4.4: Negative hadron p_T and m_T spectra. Also shown are the uncorrected data and the various correction factors subtracted from the data.

of the system about midrapidity ($y_{lab} = 2.9$) allows the participant estimate to be based on twice the number of net baryons forward of midrapidity up to beam rapidity. Because of the MTPC acceptance limit at $y_{lab} = 5.4$, the number of participants is defined here to be the total net baryons within the rapidity range $0.4 < y_{lab} < 5.4$. This integral over this range yields a total number of participants of 352 ± 12. An NA49 Veto Calorimeter measurement of the spectator nucleons found 25 projectile spectators near zero degrees in the laboratory reference frame, which is essentially beam rapidity [88]. The calorimeter data were interpreted with a model-based simulation in order to eliminate the participant energy from both charged and neutral particles from the true spectators. The calorimeter result sets an upper limit of 358 participants, which is consistent with the number of net baryons given here.

4.2.2 Negatively Charged Hadrons

Transverse and Rapidity Spectra

Negative charged hadron p_T and m_T spectra from two rapidity intervals are shown in Figure 4.4. The uncorrected data and the two major background corrections from K^0_S and hyperon decay are included in the figure. Compared to the net proton data, the relative level of background found in h^- is much lower. The largest source of background comes from the decay of K^0_S to π^-, but this is no more than a 10% effect.

The yield is sharply peaked at low p_T, which has been attributed to the creation and subsequent decay of resonance particles. Baryonic resonances, such as the Δ, can

decay to a nucleon and a low p_T pion. The production of short lived ρ and ω mesons also contribute pions at low p_T.

Below $y_{lab} = 3.7$, the low p_T acceptance quickly vanishes (Figure 2.5). Because the bulk of the yield appears at low p_T, an h^- yield cannot be determined at these rapidities. Above $y_{lab} = 3.7$, p_T spectra extend down to $p_T = 0$ and were integrated without extrapolation to give the rapidity distribution dn/dy shown in Figure 4.5. The h^- $\langle p_T \rangle$ are also shown the figure. As is the case with the net protons, $\langle p_T \rangle$ decreases with increasing rapidity because of kinematic constraints.

The total h^- yield cannot be determined from this data because of the acceptance cutoff. Data taken with a weaker magnetic field to provide midrapidity acceptance have been analyzed separately [101]. In Section 4.3.3, this additional h^- data will be combined with the results from this analysis to complete the h^- rapidity distribution forward of midrapidity.

4.3 Stopping and Particle Production

Proton stopping depends strongly on the amount of nuclear matter involved in the collision. This is illustrated in Figure 4.6, where the net protons from Pb+Pb are shown with the net protons from central S+S collisions at 200 GeV/nucleon [29] and proton+proton collisions at 400 GeV/nucleon [34]. All data are shown in the center-of-mass frame so that midrapidity coincides for all systems. The $p + p$ and S+S data are scaled to match the measured yield of net protons from Pb+Pb. The $p + p$ data exhibit a fast, exponential-like decrease in yield away from beam and target rapidities that demonstrates a uniform distribution in Feynman-x of the final state leading proton [102]. On the other hand, a central nucleus+nucleus collision results in a substantial fraction of the net protons near midrapidity. This can be directly attributed to an increased stopping power due to multiple collisions in nuclear matter compared to a single proton target [42]. A comparison of net baryon rapidity distributions from Pb+Pb and S+S is shown in Figure 4.7. A similar degree of stopping is seen in both the net proton and net baryon data.

4.3.1 Numerical Characterization of Stopping

The mean rapidity shift Δy of projectile baryons from beam rapidity is one numerical gauge of stopping. For this calculation, projectiles are defined as those baryons forward of midrapidity. The meaning of Δy is limited because projectile and target baryons can be shifted across midrapidity. Another measure of stopping is the root-mean-square (RMS) of the entire rapidity distribution. The data forward of midrapidity are reflected around $y_{cm} = 0$ to provide a symmetric rapidity distribution for the RMS calculation. The Δy and RMS of the Pb+Pb and S+S net baryon rapidity distributions are given in Table 4.1. Both measures confirm that more stopping occurs in Pb+Pb than in S+S.

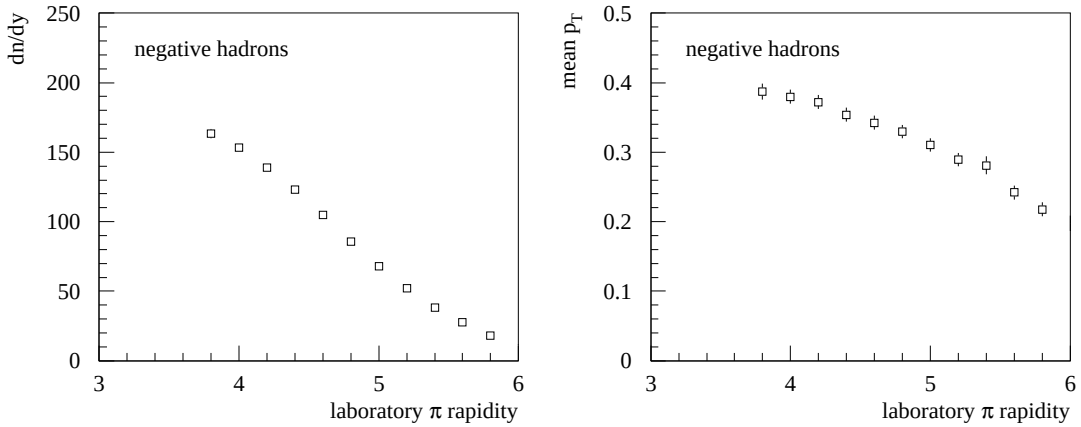

Figure 4.5: The negative charged hadron rapidity distributions of yield dn/dy (left) and mean transverse momentum $\langle p_T \rangle$ (right).

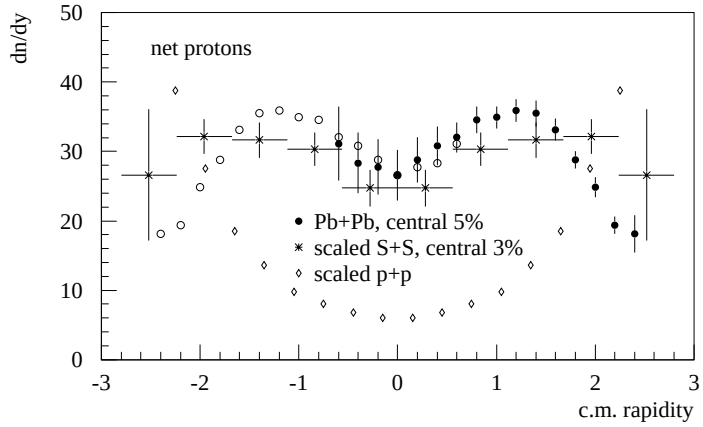

Figure 4.6: Net proton rapidity distributions from central Pb+Pb collisions, central S+S at 200 GeV per nucleon, and proton+proton at 400 GeV per nucleon. The S+S and $p+p$ data are scaled to match the number of measured net protons from Pb+Pb.

	S+S		Pb+Pb	
	$p-\bar{p}$	$B-\bar{B}$	$p-\bar{p}$	$B-\bar{B}$
Δy	-1.58 ± 0.24	-1.63 ± 0.20	-1.73 ± 0.05	-1.75 ± 0.05
RMS	1.61 ± 0.24	1.56 ± 0.20	1.35 ± 0.05	1.32 ± 0.05

Table 4.1: Mean projectile rapidity shift Δy (relative to y_{beam}) and rapidity distribution RMS widths of net protons and net baryons from S+S and Pb+Pb.

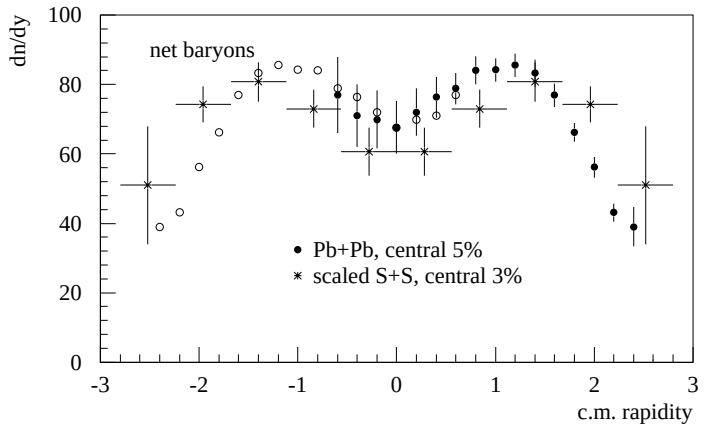

Figure 4.7: Rapidity distributions of net baryons from central Pb+Pb collisions and central S+S collisions at 200 GeV per nucleon. The S+S data are scaled to match the number of participant net baryons from Pb+Pb.

4.3.2 Energy Loss

In terms of participant baryon energy loss, the difference between Pb+Pb and S+S cannot be measured precisely because the participants lose a large fraction of their energy with only a shift of one unit of rapidity.[1] The lack of proton acceptance in the MTPCs over the last 0.4 units of rapidity up to y_{beam} means that a crucial piece of information to account for the energy of the system is missing. Within $-2.5 < y_{cm} < 2.5$ the energy is calculated with the formula

$$E = \langle m_T \rangle \cosh(y). \tag{4.5}$$

The net baryons from Pb+Pb retain approximately 30% of the initial energy, while for S+S the number is 35%. The *c.m.* energy $\sqrt{s}$ of S+S is about 10% higher than that in Pb+Pb and so the total participant energy loss is roughly the same in both systems at around 6 GeV per nucleon.

The similar energy loss per participant in the two systems does not necessarily imply that particle production will also be similar, particularly at midrapidity. The higher baryon population at midrapidity in Pb+Pb compared to S+S does not markedly change the participant energy loss, but can result in an increase in particle production because pions have a relatively small mass. In addition, the transverse momentum of produced particles may be affected.

[1] At constant p_T, a change of rapidity from 6 to 5 corresponds to an energy loss of 63%.

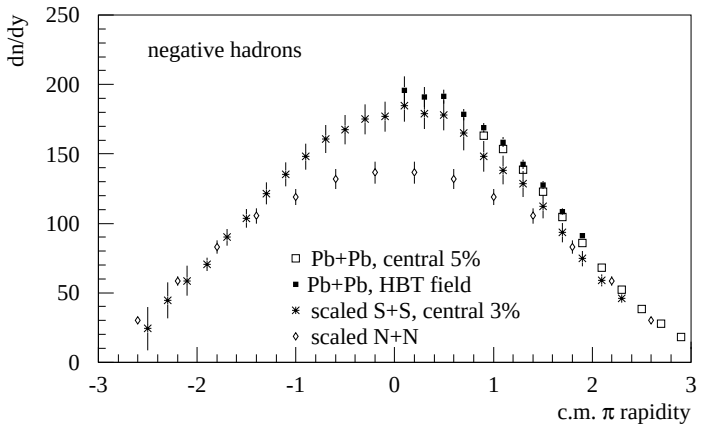

Figure 4.8: Rapidity distributions of h^- from Pb+Pb, central S+S at 200 GeV per nucleon, and isoscalar N+N at 200 GeV per nucleon. The S+S and N+N data are scaled to account for the differences in beam energy (see text) and participant net baryons.

4.3.3 Particle Production

Due to the lack of low p_T acceptance of pions at $y < 3.7$, it is neccessary to augment the h^- data with additional data taken with a half-strength magnetic field (called the HBT magnet setting), which gives the MTPCs midrapidity acceptance of pions [16, 101]. The STD and HBT h^- rapidity distributions are shown in Figure 4.8. Also shown are h^- distributions from central S+S collisions [29] and isoscalar N+N collisions at 200 GeV per nucleon [103] that are scaled to the number of participants in Pb+Pb. The isoscalar N+N data were created by applying symmetry and conservation rules to a compilation of existing $p + p$ and $p + n$ data. To account for the energy dependence of the mean number of produced particles, which has a leading term $\ln(s)$ for proton+proton collisions [36], the S+S and N+N data were scaled down by 4%. The S+S and N+N data were then scaled up by the ratio of the number of participants in Pb+Pb to the participants in the lighter systems.

An estimate of the total h^- yield is made by extrapolating the data from $y_{cm} > 0$ to full phase space. While the π^- rapidity distribution is symmetric about midrapidity, the h^- distribution is asymmetric mainly because of K^- (Section 3.1.2). Because the pion mass is used to calculate rapidity for the h^-, the kaon contribution will be shifted forward in rapidity. The h^- yield is not twice the integrated rapidity density dn/dy forward of midrapidity because the kaons are overcounted in this case. (There are relatively few $\bar{p}$ compared to π^-. The effect of overcounting $\bar{p}$ will be neglected.)

The NA49 measurement of kaons [99] (which was used as the basis of a correction in the $p-\bar{p}$ analysis) can be transformed into a rapidity distribution in terms of pion rapidity. After subtracting the K^- from the h^-, the result is almost entirely π^-.

The full phase space yield of π^- is twice the h^- minus K^- yield forward of (pion) midrapidity. The total kaon yield is added back in to give the full h^- yield:

$$N_{h^-} = 2\times(N_{h^-,y_\pi>0} - N_{K^-,y_\pi>0}) + N_{K^-}. \tag{4.6}$$

This results in an estimate of 700±30 negative charge hadrons.

In terms of h^- per participant pair, Pb+Pb yields 4.0±0.2, while the yields are lower for S+S at 3.6±0.2 and for N+N at 3.2±0.1. The enhanced particle production from nucleus+nucleus collisions beyond N+N collisions scaled for participant number is likely due to hadronic cascading within nuclear matter. The FRITIOF model, which is based on a superposition of N+N collisions, is able to reproduce the S+S h^- data well [30, 32]. However, FRITIOF predicts very few baryons at midrapidity and therefore it appears that the number of h^- is not very sensitive to stopping beyond the initial rapidity shift of one to two units by the participants.

The approximately 10% difference in h^- yield per participant from S+S to Pb+Pb is in part due to the final state distribution of isospin. If the isospin in Pb+Pb is carried entirely by pions (which means that there is an equal number of protons and neutrons), then there will be 12% more π^- than π^+ assuming that there are 650 π^- produced. It is likely that more π^- are produced per participant from collisions of neutron rich ^{208}Pb nuclei than from collisions of isospin symmetric ^{32}S. An exact accounting of isospin is not possible because neutrons are not measured and the region of rapidity near the beam is not covered by the MTPCs.

While the scaling of h^- production from S+S to Pb+Pb by the number of participant baryons may be due to the similar average energy loss per participant in the two systems, the result is also consistent with the Wounded Nucleon Model (WNM), orginally proposed by Białas *et al.* [104], that describes proton+nucleus data in terms of a superposition of nucleon+nucleon collisions. The mean number of produced particles does not depend on the number of scatterings $\bar{\nu}$ that the projectile nucleon suffers, but rather on the number of wounded, or struck, nucleons $\bar{\nu} - 1$. Simple experimental evidence supporting the WNM was found by the AFS experiment at the CERN ISR based on measurements of particle multiplicity [105] and transverse energy [106] production from collisions of protons, deuterons, and alpha particles. Because such light systems were involved, only a few possible combinations of scatters or wounded nucleons are possible, and therefore the two scenarios were distinguishable.

Data from collisions of protons with heavy nuclei support the multiple scattering picture [35]. The number of scatters and consequently produced particles increases with nuclear thickness, or $A^{1/3}$. However, the definition of the collision centrality is not well defined in this case and a convolution of the data to predict the A+A result is not a straightforward task.

The negative hadrons constitute only one part of all produced particles. There are roughly equal numbers of π^+, π^-, and π^0, but effects such as isospin conservation can slightly change the relative proportions of these particles. More importantly, there are other produced hadrons such as K^0_S, K^+, and strange baryons. It follows that the total energy carried by produced particles cannot be determined solely from the h^-.

4.4 Transverse Radial Flow

Given the increased baryon stopping in Pb+Pb compared to S+S and the similarity of the h^- rapidity distributions from the two systems, there should be noticable differences between their transverse momentum distributions. It has been pointed out that p_T distributions from heavy-ion collisions are consistent with the presence of transverse radial flow [27, 51]. If the system expands transversely with a common velocity profile for all particles, regardless of mass, there will be a systematic increase of the average p_T of each particle species with increasing mass. This effect is best observed around midrapidity, where longitudinal motion is minimized. Hadron+hadron interactions do not exhibit such behavior, which is consistent with the absence of collective effects in such a small system. While all midrapidity particles from proton+proton collisions have nearly the same $\langle p_T \rangle$, the $\langle p_T \rangle$ of kaons and protons from central S+S collisions have been shown to be larger and the value for pions remains unchanged [97]. When the system grows in size to Pb+Pb, this effect is even more pronounced and can be taken as evidence that the flow velocity increases with system size.

It has been common practice to fit p_T spectra with the exponential function given in Equation A.10:

$$\frac{1}{p_T}\frac{dN}{dp_T} = C \exp\left(-m_T/T\right). \tag{4.7}$$

A p_T distribtution that does not globally follow an exponential can be fit locally over a limited range in p_T (or equivalently m_T). The exponential function is an approximation to the Boltzmann thermal model [45], where T is the temperature of the system and is called the inverse slope parameter, or simply slope. (However, there is no definitive evidence that the system is equilibrated.) If transverse radial flow is present, then T is an effective temperature that is offset from the freezeout temperature by a factor that depends on the particle mass and flow velocity. As with $\langle p_T \rangle$, the slope should also increase with particle mass. The slope, rather than $\langle p_T \rangle$, has been used by the NA44 experiment to characterize their transverse mass spectra [107]. The p_T range over which the NA49 data have been fit to extract slope parameters was limited to match the NA44 phase space acceptance.

4.4.1 System Size Dependence

Table 4.2 is a compilation of $p-\bar{p}$ and h^- $\langle p_T \rangle$ at midrapidity from Pb+Pb, S+S, and p+S. The p+S data are meant to be representative of a very light system with little or no collective behavior. The nucleus+nucleus data show that the $\langle p_T \rangle$ values have a particle mass dependence. The midrapidity net proton slopes are given in Table 4.3 and have a system size dependence parallel to that of $\langle p_T \rangle$.

net protons			
system	experiment	y_{cm} interval	mean p_T (GeV)
Pb+Pb	NA49	$0.1 < y < 0.3$	0.835 ± 0.031
S+S	NA35	$-2.8 < y < 0$	0.622 ± 0.026
negative charge hadrons			
system	experiment	y_{cm} interval	mean p_T (GeV)
Pb+Pb	NA49	$0.2 < y < 0.4$	0.394 ± 0.011
p+S	NA35	$-1.0 < y < 0$	0.363 ± 0.008
S+S	NA35	$-1.0 < y < 0$	0.377 ± 0.004

Table 4.2: Mean p_T of net protons and negative hadrons near midrapidity from central Pb+Pb collisions at 158 GeV/N, central S+S collisions at 200 GeV/N, and p+S collisions at 200 GeV.

net protons				
system	experiment	y_{cm} interval	T (MeV)	p_T fit range (GeV)
Pb+Pb	NA49	$0.1 < y < 0.3$	308 ± 15	$0 < p_T < 1.5$
Pb+Pb	NA44	$-0.2 < y < 0$	289 ± 7	$0 < p_T < 1.5$
S+S	NA35	$-2.8 < y < 0$	235 ± 9	$0 < p_T < 2$
S+S	NA44	$-0.2 < y < 0$	208 ± 8	$0 < p_T < 1.5$

Table 4.3: Fitted inverse slope parameter T of net protons near midrapidity from various colliding systems.

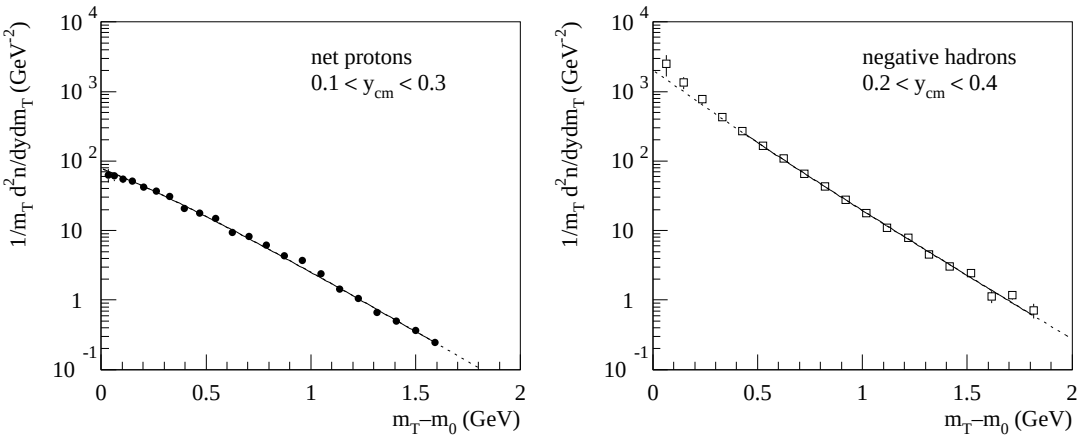

Figure 4.9: Net proton and negative hadron m_T spectra near midrapidity fit to the Chapman-Heinz model with a fixed transverse flow velocity $\beta = 0.55$. The data are fitted over the $m_T - m_0$ intervals indicated by the solid lines. The freezeout temperatures are $T = 118 \pm 5$ MeV for $p-\bar{p}$ and $T = 126 \pm 2$ MeV for h^-.

4.4.2 Multiple Scattering

The midrapidity net proton m_T distribution shown in Figure 4.9 reveals that the net protons do not follow the exponential form given in Equation A.12 beyond the limit ($p_T = 1.5$ GeV, $m_T = 0.8$ GeV) used to determine the slope given in Table 4.3. This convex shape of $p-\bar{p}$ has not been seen before from nucleus+nucleus data at CERN-SPS energies. As was mentioned previously, the concave shape of h^- is expected and is due to the production and subsequent decay of resonances to pions at low p_T. At higher p_T, the combination of π^-, K^-, and $\bar{p}$ result in a locally flatter distribution (Section 3.1.2).

Chapman and Heinz have developed a model of an expanding hadronic source that incorporates a freezeout temperature T and flow velocity β [28]. This model has been used to fit NA49 data of deuterons taken with the TOF detectors and h^- from the Vertex TPCs [55]. At a flow velocity of $\beta = 0.55$, a freezeout temperature of $T = 120 \pm 12$ MeV was determined for the deuterons and h^-. The $p-\bar{p}$ and h^- midrapidity data from the analysis presented here were fit using the Chapman-Heinz parameterization with a fixed flow velocity at $\beta = 0.55$ to give temperatures consistent with [55] at $T = 118 \pm 10$ MeV for $p-\bar{p}$ and $T = 126 \pm 10$ MeV for h^-. Figure 4.9 shows the m_T spectra at midrapidity along with fitted curves from the model. The low m_T region was omitted from the fit of h^- because of the rise in yield due to resonances, which are not included in the model.

Alternatively, the convex shape of the net proton m_T distribution at midrapidity can be attributed to hadronic rescattering. Neglecting any kinematic freezeout correlations between momentum and emission time, particles with higher m_T can lose a significant amount of momentum through collisions with other particles, which are

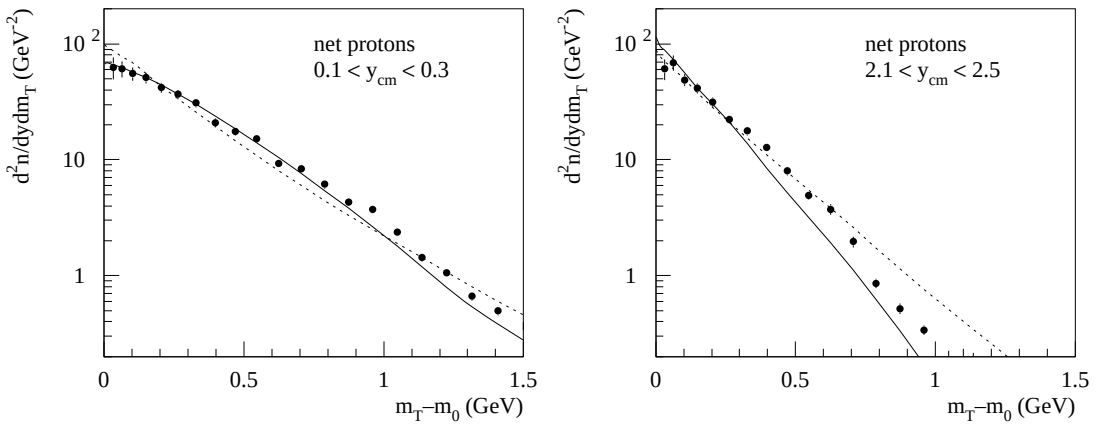

Figure 4.10: Comparison of net proton m_T spectra with RQMD (solid line) and VENUS (dotted). The model predictions are scaled to the data yield. RQMD has a greater degree of hadronic rescattering near midrapidity, which will transport particles to higher m_T.

predominantly pions at a lower m_T. Multiple scattering results in lower m_T particles gaining m_T while the higher m_T particles lose m_T. Figure 4.10 shows m_T spectra of $p-\bar{p}$ from two rapidity intervals, one near midrapidity and the other close to beam rapidity. For comparison, the predictions of two models, RQMD and VENUS, are included. These models were chosen because the average number of collisions that a particle suffers in RQMD is greater than than that in VENUS. At midrapidity, RQMD gives a distribution with a curved shape similar to that of the data, while VENUS produces a nearly exponential distribution. If the rescattering option in RQMD is disabled, then the m_T spectrum becomes exponential and resembles, in shape, the VENUS distribution [108]. For rapidities $2.1 < y_{cm} < 2.5$, the data and predictions are closer to a pure exponential. There, the net protons have a large longitudinal velocity component and a much smaller effect from rescattering is seen.

4.5 Model Predictions of Stopping

For reference, a comparison of proton and baryon stopping between the NA49 data and predictions from the RQMD and VENUS models was made. Proton stopping is shown in Figure 4.11. The hyperon decay corrections to the data are based on the model that used for the comparison. Figure 4.12 shows the net baryon rapidity distribution from the models and the data. Because the variation of the net baryon distribution from the different possible hyperon distributions is small, the data points in the figure are taken from Figure 4.7. The number of proton and baryon participants integrated yields in the rapidity range $-2.5 < y < 2.5$ are listed in Table 4.4.

	net protons	net baryons
data	148±5	352±12
RQMD	131	356
VENUS	136	336

Table 4.4: Participant protons and baryons from NA49 data, RQMD, and VENUS.

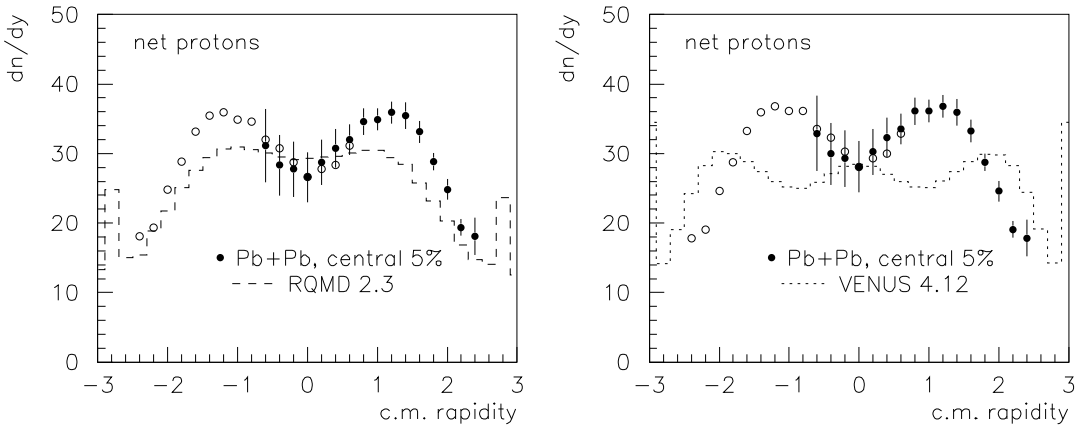

Figure 4.11: Net proton rapidity distributions from central Pb+Pb collisions, the RQMD model (left), and the VENUS model (right). Corrections are based upon the corresponding model.

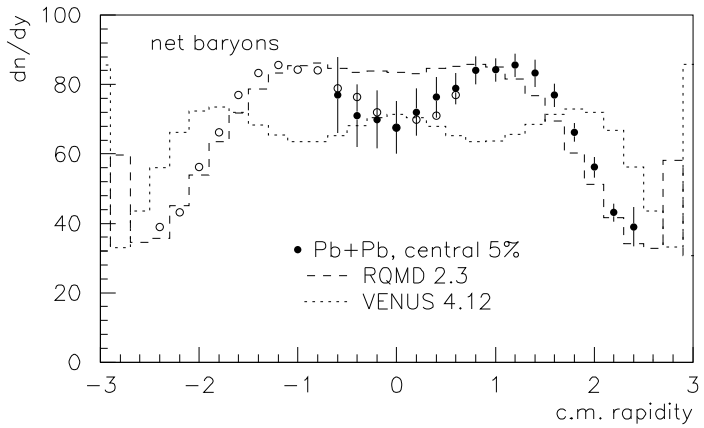

Figure 4.12: Net baryon rapidity distributions from central Pb+Pb collisions, the RQMD model, and the VENUS model. The Pb+Pb data were created using hyperon distributions from RQMD.

4.6 Summary

At CERN-SPS energies, baryon stopping, as shown by the rapidity distribution of final state net baryons, increases from central S+S collisions to central Pb+Pb collisions. The total yield and rapidity density of negative charge hadrons scale with the number of participating nucleons and show a modest enhancement relative to nucleon+nucleon collisions. At midrapidity, the mean transverse momentum of net protons from Pb+Pb is substantially greater than that from S+S, while the $\langle p_T \rangle$ of negative charge hadrons from the two systems are nearly identical. The $\langle p_T \rangle$ dependence on particle mass is consistent with the existence of a transverse flow velocity. The transverse radial flow grows in strength with increasing system size. The data presented here are consistent with an expanding system with a temperature around 120 MeV and a flow velocity of $0.55c$. From a study of event models, hadronic rescattering appears to play an important role in determining the shape of the net proton midrapidity p_T distribution.

Appendix A

Kinematic Variables and Phase Space Distributions

A.1 Kinematic Variables

From the three-momentum(p_x, p_y, p_z)[1] and mass of a particle, the scalar kinematic variables transverse momentum p_T, transverse mass m_T, and rapidity y can be derived.

In the laboratory reference frame of a fixed target experiment, only the projectile particle has momentum before the collision. For this reason, the laboratory coordinate system has the longitudinal direction ($\hat{z}$) coincident with the beam direction. Therefore, longitudinal momentum p_L is the momentum component p_z along the beam axis. Orthogonal to p_L is transverse momentum p_T, which is defined as

$$p_T = \sqrt{p_x^2 + p_y^2}. \tag{A.1}$$

Because the system initially carries only longitudinal momentum, the transverse momentum carried by a particle in the final state is a result of the interaction. Transverse mass m_T incorporates the particle mass m and is defined as

$$m_T = \sqrt{p_T^2 + m^2}. \tag{A.2}$$

Rapidity y is strongly dependent on longitunal momentum p_L and is defined as

$$y = \frac{1}{2} \ln \frac{E + p_L}{E - p_L} = \frac{1}{2} \ln \frac{1 + v_L}{1 - v_L}. \tag{A.3}$$

The rapidity coordinate of a particle in one reference frame can be transformed to the coordinate in another frame by a "boost" of the relative rapidity difference of the two frames. The shape of a rapidity distribution dN/dy is Lorentz-invariant, or independent of reference frame.

[1] For convenience, the speed of light c will be taken as 1 so that momentum, mass, and other related quantities are expressed in units of energy.

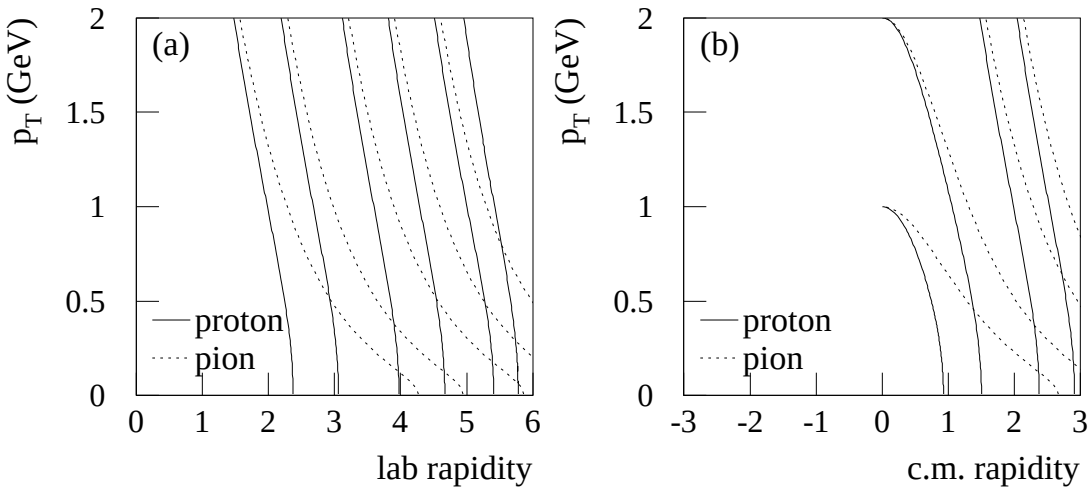

Figure A.1: Contours of constant total momentum in (y, p_T) space for pions and protons in the laboratory frame (left) and the center-of-mass frame (right). The laboratory momenta, from left to right, are 5, 10, 25, 50, 100, and (beam) 158 GeV. The $c.m.$ momenta are 1, 2, 5, and (beam) 8.6 GeV.

A.1.1 Relationship Between Momentum and Rapidity

A ^{208}Pb beam nucleus from the CERN-SPS at 158 GeV per nucleon corresponds to a laboratory rapidity of $y_{lab} = 5.82$. The target Pb nucleus is at rest at $y_{lab} = 0$. Midrapidity, or the rapidity of the center-of-mass, is therefore at $y_{lab} = 2.91$. Because of the invariant shape of rapidity distributions and the symmetry of the Pb+Pb system, the final state particle rapidity distributions are symmetric about midrapidity in any reference frame.

Figure A.1 shows the relationship between y, p_T, and total momentum with a diagram of y (calculated for protons and pions) and p_T for contours of constant total momentum. At a fixed momentum, the rapidity of a pion will always be greater than the rapidity of a proton because the pion mass is less than the proton mass. The contours at 158 GeV (laboratory frame) and 8.6 GeV (center-of-mass frame) indicates the kinematic limit for an idealized two-body elastic nucleon-nucleon scattering. Note that as the rapidity increases, a fixed rapidity interval corresponds to a larger interval of total momentum because of the logarithmic definition of rapidity.

If a fixed mass hypothesis is used to calculate rapidity, then the resulting rapidity value may not be correct. Figure A.2 shows the correct rapidity of pions, kaons, and protons for calculated rapidities of 3, 4, and 5 based on the assumption of the pion mass or the proton mass. If all particles are treated as pions, as is the case for the negative charge hadrons h^-, then the kaons and protons at the calculated rapidity are from a lower rapidity. The resulting h^- rapidity distribution will be skewed slightly

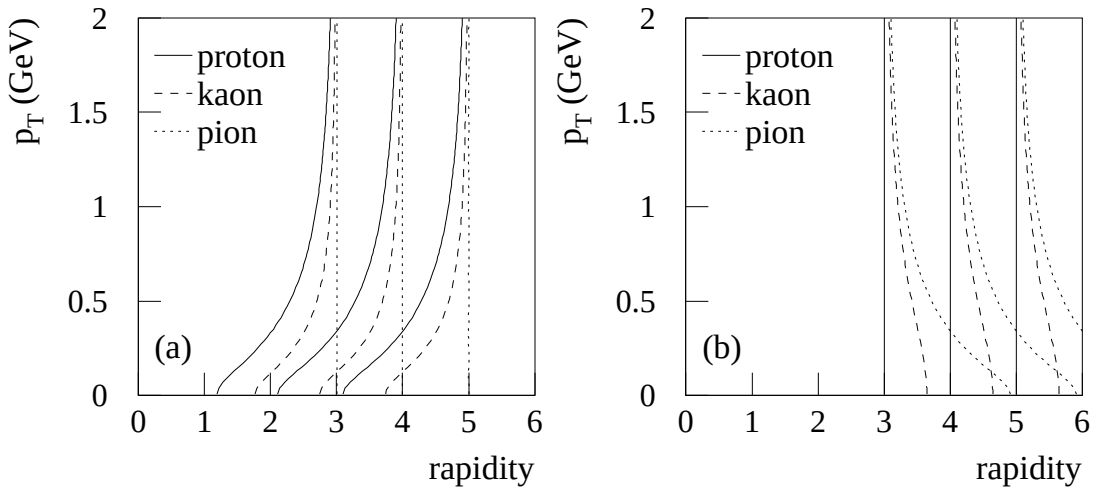

Figure A.2: A pion, kaon, or proton with an assigned rapidity of 3, 4, or 5 based on the assumption of the pion mass (left) or proton mass (right) has an actual rapidity indicated by the lines.

forward of (pion) midrapidity.

A.2 Transverse Momentum Distributions

Transverse momentum distributions of particles from high energy proton+proton, proton+nucleus, and nucleus+nucleus collisions have been observed to approximately follow the shape of an exponential in transverse mass [109, 110]. The physics of nucleus+nucleus collisions can modify this distribution, but an exponential $\exp(-m_T)$ is a convenient parameterization to use for simulations or other calculations.

Such a prediction of the final state rapidity distributions cannot be made as in the case for the transverse distributions because the system may be strongly expanding in the longitudinal direction. At high beam energies, the large initial longitudinal momentum of the system is carried through into the final state. An extreme view of longitudinal behavior is Bjorken's model of a boost-invariant system (Section 1.4.3), where at any rapidity near the center-of-mass, matter is longitudinally expanding away in both directions.

An invariant phase space cross-section takes the form

$$E\frac{d^3N}{dp^3} \propto \exp(-E/T) \tag{A.4}$$

where E is energy and T is what is called the inverse slope parameter[2]. With the

[2] The typical inverse slope parameter is in the range of a few hundred MeV for most

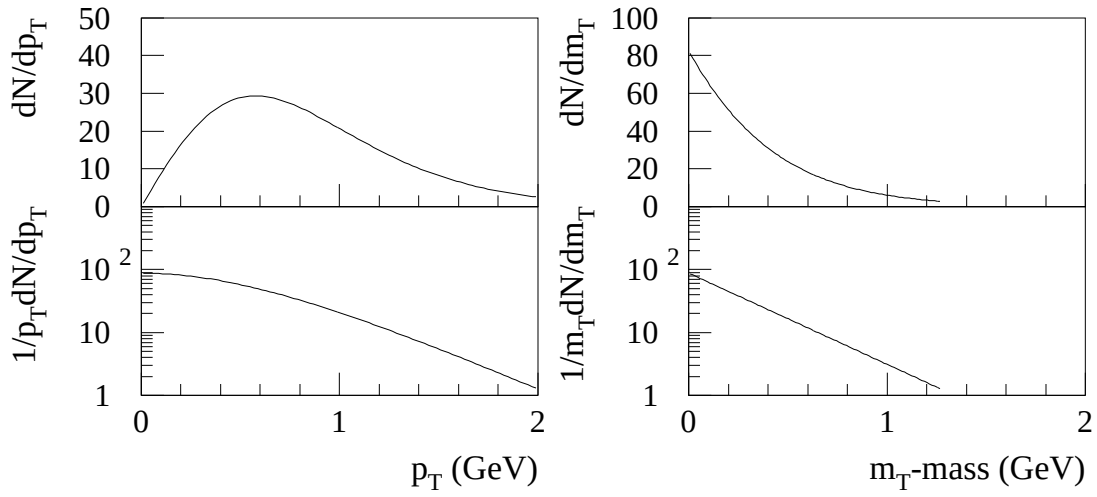

Figure A.3: Example (left) p_T and (right) m_T proton distributions from Equations A.10 and A.12 with an inverse slope parameter $T = 300$ MeV and normalization constant $C = 2000$.

following relationships between y, p_L, and energy E

$$E = m_T \cosh y \tag{A.5}$$

$$p_L = m_T \sinh y, \tag{A.6}$$

then

$$\frac{d^2N}{dp_x dp_y} \propto \frac{dN}{2\pi p_T dp_T} \tag{A.7}$$

$$\frac{dN}{dp_z} \propto \frac{1}{m_T \cosh y} \frac{dN}{dy} \tag{A.8}$$

and Equation A.4 becomes

$$\frac{1}{p_T} \frac{d^2N}{dy dp_T} \propto \exp\left(-m_T \cosh y / T\right). \tag{A.9}$$

At midrapidity, the p_T distribution is

$$\frac{1}{p_T} \frac{dN}{dp_T} = C \exp\left(-m_T/T\right), \tag{A.10}$$

where C is a normalization constant. Using the relationship

$$\frac{dm_T}{dp_T} = \frac{p_T}{m_T}, \tag{A.11}$$

hadrons from particle collisions at CERN-SPS energies.

another way to show transverse data is in terms of m_T:

$$\frac{1}{m_T}\frac{dN}{dm_T} = C\exp\left(-m_T/T\right). \tag{A.12}$$

Plots of the functions given in Equations A.10 and A.12 are shown in Figure A.3. The parameters used were $C = 2000$, $T = 300$ MeV, and the proton mass. When Equation A.12 is plotted with a logarithmic abscissa, the result is close to a straight line down to $m_T = m$, the particle mass (p_T=0). This makes $1/m_T dN/dm_T$ an attractive variable to display a transverse spectrum. However, the bulk of the yield is at low p_T and when the m_T variable is used, the low p_T region is compressed into a small range in m_T.

Appendix B

Simulations and Corrections

B.1 Introduction

In Chapter 3, corrections to the data for track reconstruction inefficiencies and background tracks were described without going into detail about how these corrections were calculated. Simulations of the experiment were developed to estimate the correction factors through a controlled study of the behavior of processes that affect the measured data. The components of the simulation, from computer software to analysis techniques, will be discussed in the following sections.

B.2 Simulation Programs

The TPC simulation is composed of several computer programs, each of which performs a specific task, that are run sequentially to form a chain that is shown as a flowchart in Figure B.1. These programs include both established, previously written software and newly written software created specifically to suit the experiment.

The input to the simulation chain is in essence a list of particles at the target vertex. Additional details on the input are given in Section B.3. The transport of particles through the experimental apparatus is handled by the GEANT detector simulation package [111]. GEANT calculates the TPC track trajectories and generates idealized TPC points with corresponding energy loss values. A specialized MTPC response simulator MTSIM uses the GEANT output to create TPC data in the raw experimental data format. If the simulated event consists of only a few tracks, an actual experimental event can be superimposed on top of the simulation with MTEMBED to provide a realistic background so that embedded event appears to the reconstruction software as being practially identical to the experimental data.

The event is reconstructed with MTRAC, the MTPC track reconstruction program (Section 3.3). MTRAC is operated in a manner identical to that of the experimental event reconstruction and the performance of the reconstruction program should be the same in both cases. The reconstructed data, in the form of TPC points and tracks,

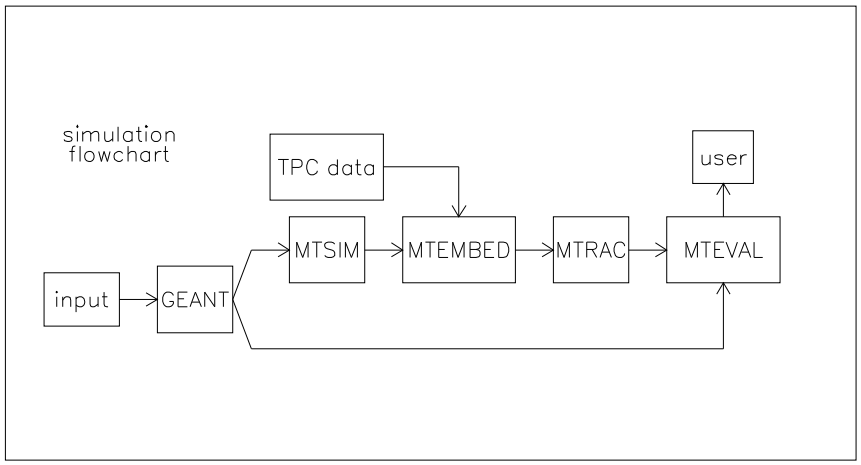

Figure B.1: A flowchart of the simulation process. See the text for descriptions of the programs GEANT, MTSIM, MTEMBED, and MTEVAL. The MTPC track reconstruction program MTRAC was described in Section 3.3. A discussion on the simulation input can be found in Section B.3.

are compared to the GEANT output with an evaluation tool called MTEVAL. The user can then examine the simulation results to create the corrections.

In the case that the number of simulated tracks is on the order of 10% of the average track multiplicity from experimental data and that the simulation involves embedding, the entire simulation chain runs in under one minute per event. Track reconstruction takes up about half of the running time.

Most TPC-based experiments have implemented similar methods creating and studying simulations. Two heavy-ion experiments whose simulations are similar in concept to NA49 but differ in detail are EOS [112] and STAR [113].

B.2.1 GEANT and GNA49

The CERN-developed GEANT software [111] simulates the transport of particles through a detector apparatus. GEANT is designed to be modified by the user to model the physical layout of an experiment. The event is defined by a list of particles at the target vertex and their initial momentum vectors. Interactions with detector materials, decay of unstable particles, and production of secondary particles are all accounted for with Monte Carlo techniques. The NA49 GEANT (GNA49) models nearly every component of the NA49 apparatus, from the large aluminum support frame from which the gas box is suspended down to the thin mylar strips of the TPC field cages. The magnetic field is based on the same map used by the reconstruction software.

A GNA49 TPC track is composed of idealized points along the particle trajectory. For each padrow crossing of a track, the point coordinate is calculated in the transverse plane located at the middle of the padrow. Most particles are energetic enough to

cross a padrow gas volume without being transversely deflected more than a few millimeters by multiple scattering.

A special case is the δ electron, which leaves behind a crooked trail of ionization due to its low momentum and light mass. To accurately describe these electron tracks, GNA49 creates one point for every 3 mm of path length because the δ can travel a considerable transverse distance within a single padrow.

TPC ionization drift and readout are not handled by GNA49. Instead, the simulation of the TPC response and creation of raw readout data is performed by a dedicated program that uses the GNA49 output. The output of GNA49 consists of data arrays representing particles, interaction verticies where one particle branches off to other particles, and the TPC points. These arrays contain relevant information such as the particle type and momentum, TPC point coordinates, and indicies for cross referencing. Indicies are necessary to provide a record of the relationship between the different data such as a particle and the TPC points that it generates.

B.2.2 TPC Simulation: MTSIM

The Main TPC simulation program, MTSIM, reads in the GNA49 output and creates data in the form of digitized output of the TPC electronics. The same reconstruction software used to analyze the experimental data can therefore be used for the simulated data as well. MTSIM takes the GNA49 TPC points and produces charge cluster data based on the properties of the TPC gas and readout electronics. The signal threshold cuts and compression algorithm of the data aquisition system are then applied to complete the simulation.

Particle Energy Loss

The charged particle energy loss in the TPC gas can be modelled in either GNA49 or MTSIM. Energy loss determines the amplitude of a charge cluster distribution, which is used by the track reconstruction program to calculate the truncated mean energy loss $\langle dE/dx \rangle$ of a track that is needed for particle identification purposes (Section 2.3.2).

For each TPC point, GNA49 provides a calculation of energy loss dE/dx in electron volts based on the composition of the TPC gas. The energy loss value associated with a TPC point may be lower than the actual total energy loss by the particle as it crosses the padrow because δ electrons may carry away some of the energy. The point-by-point dE/dx fluctuations are modeled according to Landau-Vavilov theory.

Alternatively, MTSIM can incorporate a user defined parameterization of an idealized dE/dx distribution as a function of momentum. The point-by-point dE/dx fluctuations for a single track are based on the Moyal distribution [115], which is a good approximation of the Landau distribution.

The dE/dx values are adjusted for effects such as charge loss during drift and the dependence of measured energy loss on the track path length. These effects were

modelled after the behavior observed in the experimental data that is discussed in Section 3.3.1.

While the GNA49 based energy loss calculation was acceptable for the simulations used in this work, it may be desirable in the future to model the energy loss within MTSIM. A better understanding of how the TPC performs along with more accurate detector calibrations can reveal new details to incorporate into the dE/dx model.

Charge Cluster Formation

MTSIM forms charge clusters from the GNA49 TPC point data and a Gaussian parameterization of the cluster shape called a pad response function [72, 71, 116]. It has been observed in TPC data that the pad readout response to a point charge source is distributed as a Gaussian because of the finite pad size and the capacitive coupling of the anode wires and the pad plane[1] [80]. Any TPC pad readout has a response that forms an intrinsic minimum cluster width. Charge clusters from particle tracks will also spatially diffuse before readout during transport through the TPC gas by the electric drift field. Taking these two factors into account, the basic pad response function describes the sigma of a Gaussian cluster as

$$\sigma^2 = \sigma_0^2 + \lambda\sigma_{diff}^2. \tag{B.1}$$

The intrinsic width is σ_0 and the diffusion term is composed of the drift length λ to the pad plane and the constant σ_{diff}. A list of the pad response function parameters are given in Table B.1.

There are separate response functions for the pad and time dimensions. The intrinsic signal width in the time direction is determined by the shaper amplifier. The shaper response rises quickly and then falls off exponentially, undershooting the baseline by 5% of the integrated signal over 1 μs before returning to zero, but a Gaussian response was assumed for the simulations performed for this analysis. The intrinsic spatial width in the time direction is the product of the drift velocity (around 2.4 cm/μs) and the shaper width.

A track that crosses a padrow at a non-perpendicular angle cannot be modelled completely with the pad response function of Equation B.1 because the resulting clusters are flatter than a Gaussian. Instead of creating a single cluster from a GNA49 TPC point, the track path within the padrow volume is sampled several times. By breaking the padrow crossing into several points and creating subclusters at each new point, the desired cluster shape can be achieved. For MTPC tracks with crossing angles up to 60° relative to the perpendicular, no more than 10 samples are ever needed. In most cases, only one or two samples suffice. The number of samples taken is based on the transverse path length across a padrow divided by the full width of the pad response (twice the pad response function).

[1] The point charge source was an electron gun close enough to the readout region such that diffusion was not important.

parameter	pad	time
σ_0	1.8, 2.3, 2.4 mm	0.084 μs
σ_{diff}	270 μm/$\sqrt{\text{cm}}$	300 μm/$\sqrt{\text{cm}}$

Table B.1: Typical parameters used by the pad response functions of MTSIM. The intrinsic width σ_0 in the pad direction is given for the HR, SR, and SR-prime sectors. In time direction, σ_0 is the shaper amplifier response width.

Because the cluster shape is Gaussian, the charge signal in a pad-timeslice pixel can be calculated with the error function, which is a special case of the incomplete gamma function. After all clusters are formed within a padrow, the data, which are in floating point format, are digitized. The overflow limit of 255 ADC counts and the minimum threshold cut of 5 counts are imposed, and zero suppression (Section 2.3.1) is performed.

Each parameter used in MTSIM has an associated uncertainty that is used to vary the parameter for each cluster calculation. For example, clusters that have drifted the same distance will show a variation in width because of the stochastic nature of diffusion. The mean drift constant σ_{diff} is slightly modified for each cluster by introducing an additional term σ_{var} multiplied by a random deviate G taken from a Gaussian distribution with $\sigma_G = 1$:

$$\sigma_{diff,new} = \sigma_{diff,mean} + G\sigma_{var}. \tag{B.2}$$

Diffusion can also displace the cluster centroid. The length scale of this shift is much smaller than the cluster size, on the order of 100 microns. The equation governing this behavior is called the pad resolution function:

$$\sigma^2_{reso} = \sigma^2_{0,reso} + \frac{\lambda}{N_e}\sigma^2_{diff}. \tag{B.3}$$

The intrinsic resolution $\sigma_{0,reso}$ is determined from experimental data and is around 300 μm in the pad direction and 150 μm in the time direction. The drift length λ and diffusion constant σ_{diff} are the same as the parameters used in the pad response function. N_e is the number of electrons in the charge cluster and is a function of the gas properties and particle momentum. A minimum ionizing particle in the Ar-CH_4-CO_2 gas mixture at atmospheric pressure in the MTPCs will create 80 electrons per cm of path length. The pad resolution width is used to dither the GNA49 point positions before clusters are formed. These factors are needed to reproduce the typical spatial scatter of points, or residual, from a fitted track of several hundred microns that is seen in the data.

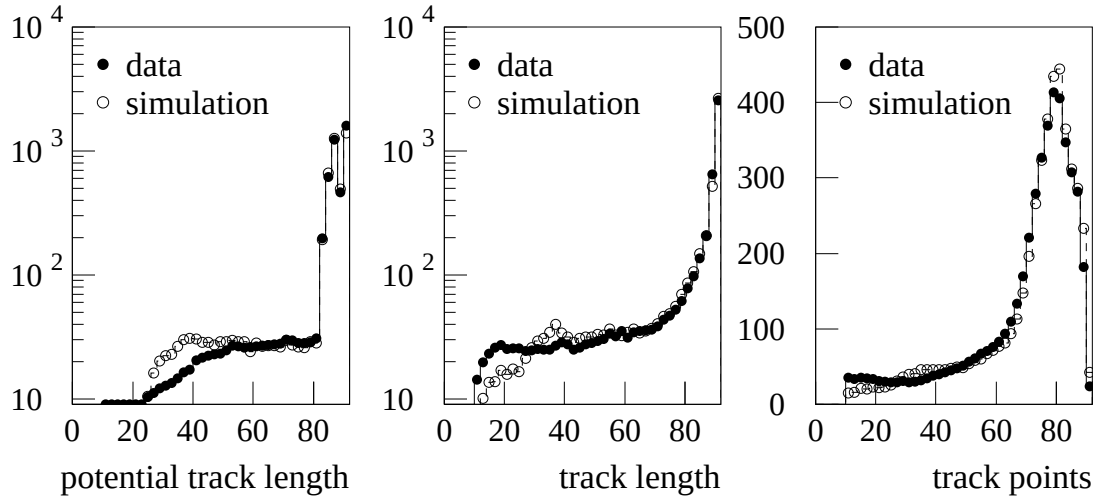

Figure B.2: A comparison of TPC track properties from simulations and data. See text for descriptions of the potential track length, track length, and track points.

Comparison to Data

Figure B.2 shows a comparison of tracks from simulation and experimental data. From the distribution of the potential track length, it is apparent that the phase space distribution of simulated tracks is not identical to that of the data because the simulation input is a phase space distribution of pions that is Gaussian in rapidity and an exponential in p_T (Equation A.10) with a slope of $T = 140$ MeV. However, the main difference is seen below the minimum track length cut of 30 points that is imposed on the data.

Potential track length is the number of points that can appear on a track based on its trajectory and the location of the MTPC readout sectors. Track length is defined as the number of padrows between the first and last point on the track and can differ from the potential length because of the gaps between sectors. The track points quantity refers to the number of points associated with the track. The distribution of track points shows that the simulation accurately reproduces the level of point losses seen in the data that is due to cluster reconstruction software inefficiencies and detector effects such as diffusion and multiple scattering.

Finally, it is instructive to examine the relative momentum resolution $\Delta p/p$ of reconstructed tracks. This quantity cannot be determined from data and is estimated from simulations. The reconstructed momenta from a large sample of tracks at a fixed momentum forms a Gaussian distribution and its width provides an estimate of momentum resolution. Figure B.3 shows the relative momentum resolution $\Delta p/p$ as a function of momentum in the laboratory frame. The resolution width is as small as 0.3% for $p < 10\text{GeV}/c$ and increases linearly with $\log(p)$.

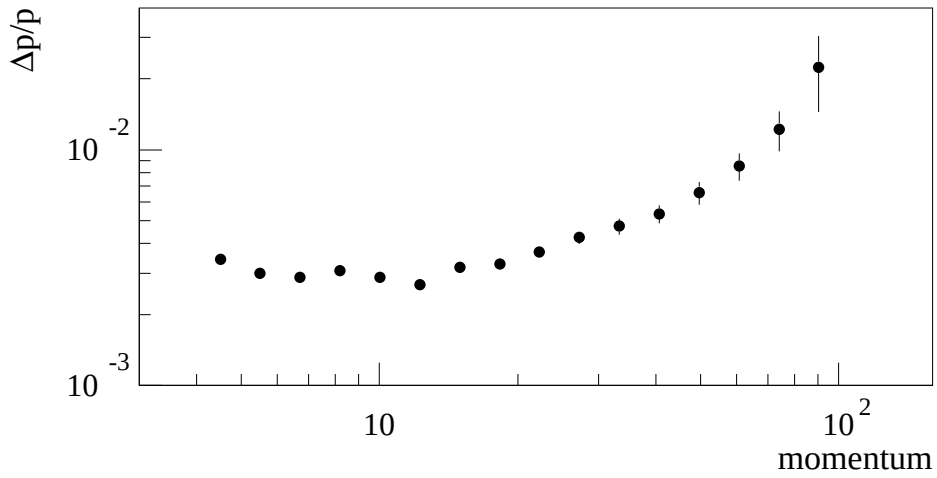

Figure B.3: Momentum dependence of the MTPC momentum resolution $\Delta p/p$ from a simulation.

B.2.3 Track Embedding: MTEMBED

It was noted in Section 3.3.3 that high track density adversely impacts the reconstruction efficiency. When a large amount of ionization is created in a TPC, it is difficult for the reconstruction software to find every good track because of crossed tracks and cluster merging. Hadronic tracks are not the only source of signal in the MTPCs; in addition, there are other sources of signal such as δ electron tracks and noise from the readout electronics.

Neither GNA49 nor MTSIM simulates the electronic noise that is seen in the experimental data. To accurately assess the influence of the experimental environment on track reconstruction, simulated data from MTSIM is superimposed onto an actual experimental Pb+Pb collision event. The number of simulated tracks in each event must comprise a small fraction of the number of tracks in the experimental event. Otherwise, the TPC charge environment would be unrealistic.

MTEMBED is the program that embeds the simulated data from MTSIM into experimental event data. Track embedding is a simple process of adding together ADC signals in each pad-timeslice pixel from both data sets. The maximum possible signal of 255 ADC counts is imposed on the combined data and then the embedded event is compressed. A shortcoming of this method is that the 5 ADC count threshold of the data aquisition system had already been imposed upon both the simulated and experimental data before the embedding process occurs. As a result, the edges of some simulated charge clusters may be slightly cropped.

B.2.4 Simulation Evaluation: MTEVAL

The TPC readout data from MTSIM does not have the information relating particles with tracks and points that exists in the GNA49 output. After an event is reconstructed by MTRAC, it is impossible to distinguish simulated tracks from background tracks. The program MTEVAL was written to match the GNA49 data to the reconstructed data. The user then evaluates the quality of reconstruction from the matching information.

The matching procedure starts with point matching, which is based on the spatial proximity of the GNA49 point to the reconstructed MTRAC point. Then the track information associated with each point is compiled to make a list of possible matches between tracks. Specialized data arrays are used by MTEVAL to record the point and track matches, which may not necessarily be one-to-one. Technical details on how MTEVAL operates is given in the two following sections.

Data Matching

Point matching is performed for one padrow at a time. A two dimensional array is used as a reference table for the reconstructed points. The array elements represent the pad-timeslice pixels of the padrow and if a point falls within a pixel, then the array element content is an index corresponding to the point. No more than one point can be reconstructed within a single pad-timeslice coordinate because charge clusters typically have widths of several pads and timeslices. MTEVAL loops over the GNA49 points in the padrow, converting the point coordinates from physical space to integer pad and timeslice values. A search is made in the array over a user defined range around each GNA49 point, usually the equivalent of around 5 mm, and a match is recorded for every reconstructed point within the search area.

After point matching, the GNA49 tracks are matched to the MTRAC tracks. For each GNA49 track, a list is compiled of the reconstructed tracks that have points matched with the GNA49 track points. Usually the majority of point matches leads to a single reconstructed track. Some simulated points may be matched to a reconstructed point that does not belong to any track. The important quantities to note when judging the quality of a match are the total number of points on the GNA49 track that are matched and the number of point matches that the GNA49 and MTRAC tracks have in common. The number of padrows between the farthest upstream matched point and farthest downstream matched point indicates the total length of the matched segment.

In general, it is best to reject outright any embedded track that has merged with other GNA49 tracks because a reconstruction bias may be introduced unless the phase space distribution of merged tracks in the simulation is identical to that in the data. It is also possible that an embedded simulated track will be placed on top of an existing track in the experimental event. This is acceptable if the simulated tracks are randomly selected in phase space and many events are studied, so that

the probability of making this kind of merged track is the same as the probability of finding merged tracks in the data.

Matching Structures

The technical details of how the matching information is stored is given in this section. MTEVAL was written in the C programming language. The TPC data are stored in structures for individual points and tracks. These structures are essentially arrays containing entries for information such as the point coordinate. At its simplest, a match is recorded by writing down two index numbers pointing to the two matched data objects. It would be wasteful to reserve space in the point structures for a match pointer because this entry is used only for simulations.

MTEVAL has its own proprietary structures that serve as placeholders for pointers that record the data matching information. A simplified example of the matching structures is given below:

```
struct gna49_env {
 gna49_point_t *point_p;
 match_point_t *match_p;
} gna49_env_t;

struct mtrac_env {
 mtrac_point_t *point_p;
 match_point_t *match_p;
} mtrac_env_t;

struct match_point {
 gna49_env_t *gna49_p;
 mtrac_env_t *mtrac_p;
 match_point_t *next_gp;
 match_point_t *next_mp;
} match_point_t;
```

The standard point data structures from GNA49 and MTRAC are hidden by the `gna49_env` and `mtrac_env` "envelope" structures. The user examines the MTEVAL output through the envelopes; the pointers `point_p` are used to access the point data, which are referred to here by the type defintions `gna49_point_t` and `mtrac_point_t`. When a GNA49 point and MTRAC point are matched, a `match_point` structure is used to connect the `gna49_env` and `mtrac_env` structures.

Although most match cases are one to one correspondences, the two pointers `next_gp` and `next_mp` in the `match_point` structure are needed to give MTEVAL the ability to handle every possible matching scenario. The functionality of the matching structures are best demonstrated with an example.

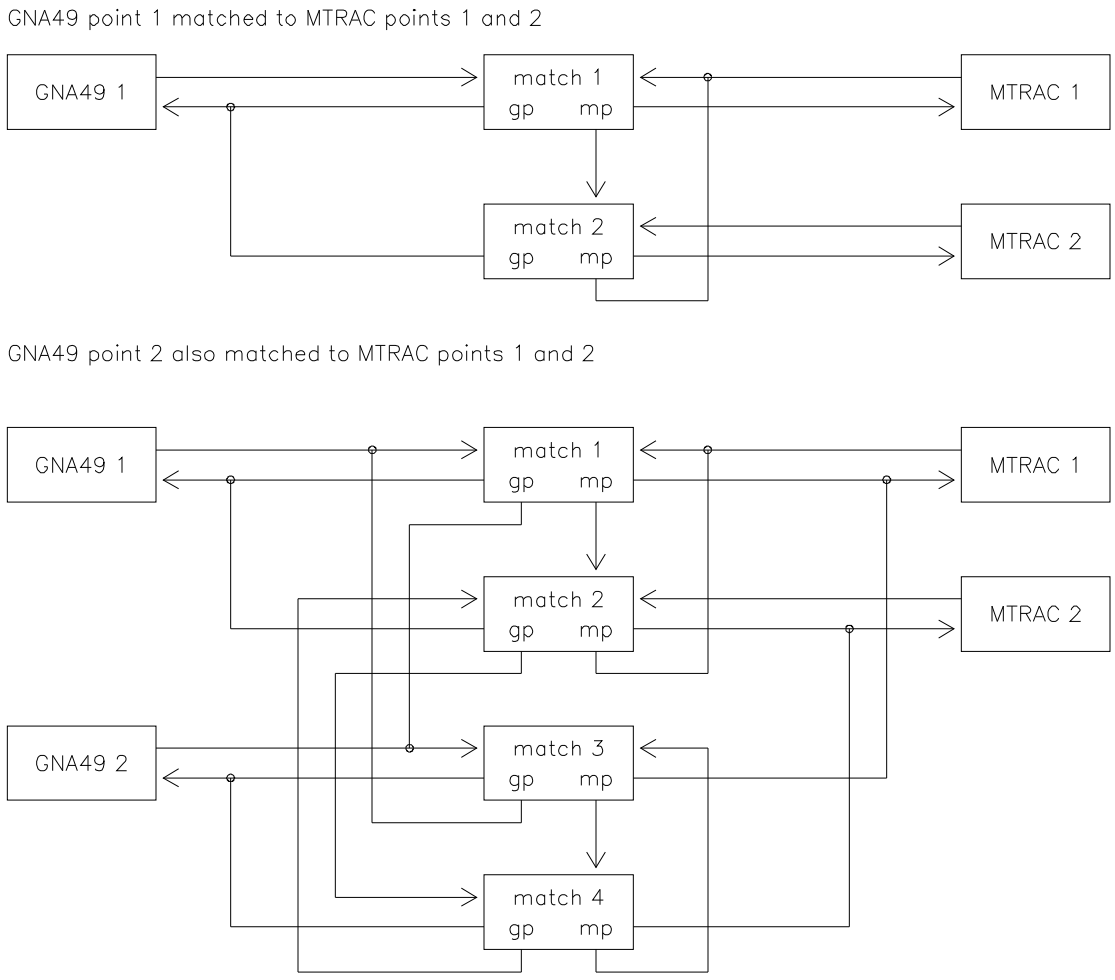

Figure B.4: An illustration of two GNA49 points matched to two MTRAC points. First, GNA49 point 1 is matched to MTRAC point 1, and then MTRAC point 2. Then GNA49 point 2 is matched to the two MTRAC points as well. See the text for a description of the boxes, which represent MTEVAL structures, and the arrows, which are pointers.

If two GNA49 points and two MTRAC points fall within the search area, then a complicated arrangement of pointers results. Suppose that at first the GNA49 point `gna49_point(1)` is matched to two MTRAC points `mtrac_point`. An illustration of the links between the structures is shown at the top of Figure B.4. The boxes represent the three types of MTEVAL structures described above. The arrows indicate which structure the pointers are directed towards. The envelopes only have their `match_p` pointers shown. The arrows from the left and right sides of `match_point` are for the `gna49_p` and `mtrac_p` pointers, while the arrows from the bottom labelled as gp and mp represent the `next_mp` and `next_gp` pointers.

The first match is recorded with `match_point(1)`, which connects `gna49_env(1)` and `mtrac_env(1)`. The other match is indicated by the `match_point(1).next_mp` pointer that leads to `match_point(2)`. This structure, like `match_point(1)`, points to `gna49_env(1)`, but it records the match with `mtrac_env(2)`. Because there is no entry for `match_point(1).next_gp`, `mtrac_env(1)` is matched to only one GNA49 point. The same is true for `mtrac_env(2)`.

After the `gna49_point(2)` is matched to the two MTRAC points, the arrangement of MTEVAL structures and pointers becomes quite complicated, as is shown at the bottom of Figure B.4. Only a few features will be described here. As before, the `gna49_env(1).match_p` pointer leads to `match_point(1)`. But now `match_point(1).next_gp` can be followed to `match_point(3)`. This indicates that another GNA49 point, `gna49_env(2)`, is also matched to `mtrac_env(1)`.

B.3 Simulation Input

An entire event from a model such as RQMD or VENUS can be processed through the simulation chain all at once to provide an estimate of the hadronic background, but this is not an efficient use of computation time. Because physically accurate phase space distributions of particles fall off exponentially at p_T above 1 GeV, many events have to be simulated so that the statistical flucutations at high p_T are small.

Another shortcoming of purely model based events is the background of electronic noise and δ electrons may be underestimated. The embedding procedure described in Section B.2.3 circumvents this problem, but if the embedded tracks are selected from a realistic phase space distribution, a lack of statistics at high p_T will occur.

If the simulated tracks are drawn from a flat phase space distribution, the simulation result will have the same statistical weight at all rapidity and transverse momentum. The result can then be reweighted to reflect a realistic particle distribution. All simulations performed for this work used this method.

The reweighting factors are calculated by first counting the particles from the simulation input in phase space bins. The reweighting factor in each bin is the number of input particles divided by the integrated yield of the physical phase space distribution. A reconstructed track is counted with the reweighting factor for the particle that produced the track. In the case of Λ decay, the detected proton will

be weighted according to its parent Λ momentum, not its reconstructed momentum. Assuming that the statistical error of the simulation can be estimated using the central limit theorem, the total number of reconstructed tracks must also be counted.

B.4 Corrections to the Data

This section contains additional details about the corrections to the TPC data for the track reconstruction inefficiencies and hadronic background first described in Sections 3.3.3 and 3.5. All corrections were calculated from embedded event simulations. The simulated tracks were taken from a flat distribution in phase space and then the simulation results were reweighted by the method described in Section B.3 so that the correction factors are based on realistic particle distributions. The simulated tracks embedded into a single event should not substantially alter the character of the event. The number of tracks per event in each MTPC, including those tracks not from the target, rarely exceeds five hundred. An increase in track multiplicity by 10% to 15% from embedded tracks does not affect the event reconstruction.

The estimated correction errors were based on a Poisson statistical distribution because the simulated events were studied as an ensemble. Correction factors were calculated only for those phase space bins with at least 100 counted tracks before event renormalization. Given that the typical correction factor is only a few counts per event, binomial distributed errors are in principle appropriate, but the method by which the corrections are calculated allows for the use of Poisson statistics. In the case of the decay background corrections, the uncertainty of the simulation input distribution was propagated to the correction factors.

B.4.1 Acceptance and Tracking Inefficiency

Fifty proton and fifty antiproton tracks distributed evenly across the MTPC phase space acceptance were embedded per event for the for the acceptance and tracking inefficiency correction. The same embedded events were used in the correction calculations for both protons and pions. Particle rapidity was determined from the laboratory momentum of the simulated protons and a fixed mass hypothesis.

The simulated data phase space distributions were reweighted to match the proton and pion distributions from RQMD central Pb+Pb collision events. The correction factors are not sensitive to slight variations of the p_T distribution shape. Identical corrections at midrapidity were calculated from proton p_T slope parameters of 260, 280, and 300 MeV.

B.4.2 Particles From Weak Decays

The only background correction used in the net proton analysis was for the decay of hyperons ($\Lambda, \Sigma^{\pm}$) to protons and antiprotons. The negative charge hadron mea-

surement required a correction for π^- from K^0_S decay as well as h^- from hyperon decay. These corrections are calculated for strange particle phase space distributions from a variety of sources. When the simulation input comes from an event model, it is completely described in phase space by a discretely binned distribution. NA49 measurements cover a limited range in phase space and are extrapolated to all phase space with a parameterized Gaussian function in rapidity and the p_T distribution is described by a single p_T slope parameter that is independent of rapidity.

A shortcut was taken to calculate the charged Σ decay correction. To reduce computation time, simulated Λ events were reused. The distributions of reconstructed protons and pions from lambda decay were substituted for the protons and pions from sigma decay. In addition to changing the simulation input distribution from lambdas to sigmas, the simulation results had to be rescaled to because the branching ratio of $\Lambda \to p\pi^-$ (64%) is different than $\Sigma^+ \to p\pi^0$ (52%). The procedure is not exactly correct because the mean life of Λ is $c\tau \sim 7.89$ cm while $c\tau \sim 2.4 - 4.4$ cm for a charged Σ. Also, $\Sigma^\pm$ has a slightly higher mass than the Λ, and this will somewhat affect the decay kinematics. Most Λ and Σ decay within a few centimeters of the target and nearly every proton daughter from Λ decay is measured and reconstructed as a target vertex particle. Because of the shorter lifetime of the Σ, the Σ decay correction calculated from the Λ simulations will be underestimated, but only by a small amount that will be neglected.

Appendix C

Charged Particle Spectra Data Tables

Tables C.1 through C.10 contain the $d^2n/dydp_T$ and dn/dy values of the net proton, net baryon, and negative charge hadron data. All hyperon decay corrections were based on predictions from the RQMD model. The extrapolation from net protons to net baryons also utilized the RQMD hyperons.

The quoted errors include both statistical and systematic errors from the measurement and correction factors. The $K^+ - K^-$ correction to the net protons introduces a correlated error in both rapidity and transverse momentum that is not listed separately.

$p_T \pm 0.05$ GeV/c	$2.2 < y < 2.4$	$2.4 < y < 2.6$	$2.6 < y < 2.8$	$2.8 < y < 3.0$
0.05	2.22±0.54	2.42±0.52	3.12±0.48	2.44±0.53
0.15	4.96±1.43	8.27±1.46	7.96±1.19	8.38±1.58
0.25	15.3±4.2	13.7±2.7	12.4±1.9	13.0±1.6
0.35	19.1±5.4	16.6±3.1	18.3±2.6	17.4±3.2
0.45	19.5±4.3	18.4±3.7	20.8±4.3	21.0±2.3
0.55	26.6±4.9	25.8±4.2	22.8±3.5	23.0±2.5
0.65	25.6±4.8	26.0±3.7	24.2±3.4	23.8±2.5
0.75	25.1±4.4	29.4±3.7	23.6±2.7	22.4±2.2
0.85	28.0±4.1	21.4±2.7	25.7±3.1	19.1±2.0
0.95	21.3±3.2	25.7±3.5	20.9±2.4	23.8±2.2
1.05	20.8±3.3	21.1±3.7	22.4±3.5	18.4±1.7
1.15	22.8±3.2	15.0±1.9	19.1±1.9	16.5±1.7
1.25	21.2±3.3	13.5±1.6	13.7±1.7	13.6±1.4
1.35	18.9±2.8	12.8±1.5	10.3±1.2	11.4±1.4
1.45	11.9±2.1	10.1±1.2	8.18±0.99	7.38±1.26
1.55	6.48±1.09	6.18±0.77	7.26±0.86	6.78±0.79
1.65	5.31±0.87	3.41±0.44	4.46±0.49	6.16±0.68
1.75	4.75±0.73	3.80±0.51	3.78±0.43	2.93±0.39
1.85	2.68±0.41	2.97±0.42	2.37±0.27	2.96±0.30
1.95	3.01±0.45	1.76±0.21	1.77±0.20	1.49±0.17
2.05	1.73±0.44	1.52±0.18	1.67±0.19	1.38±0.15
2.15	2.02±0.35	1.63±0.34	0.71±0.09	0.98±0.10
2.25	0.67±0.15	0.86±0.12	0.95±0.12	0.85±0.13
2.35	0.78±0.14	0.55±0.08	0.59±0.07	0.59±0.07
2.45	0.71±0.14	0.46±0.09	0.55±0.09	0.39±0.07

Table C.1: Net proton $d^2n/dydp_T$ from the rapidity range $2.2 < y < 3.0$.

$p_T \pm 0.05$ GeV/c	$3.0 < y < 3.2$	$3.2 < y < 3.4$	$3.4 < y < 3.6$	$3.6 < y < 3.8$	$3.8 < y < 4.0$
0.05	2.80±0.48	3.03±0.38	3.46±0.38	3.72±0.71	3.81±0.69
0.15	9.62±1.68	10.5±1.1	11.4±1.0	11.8±2.1	11.1±1.4
0.25	14.2±2.4	17.3±1.6	18.5±3.0	21.9±2.8	20.4±1.5
0.35	22.0±2.2	20.8±1.8	24.7±3.2	27.5±1.8	27.7±1.6
0.45	23.0±3.1	26.9±2.0	28.4±2.9	30.7±1.9	30.0±1.7
0.55	25.3±2.2	30.9±2.1	30.9±3.0	32.2±2.7	34.0±1.7
0.65	27.5±2.9	27.4±1.8	31.4±2.5	31.5±2.3	33.1±2.1
0.75	27.8±2.6	27.2±2.2	28.3±2.0	31.5±2.0	32.6±1.8
0.85	23.3±2.1	29.1±2.0	25.1±1.6	28.0±1.6	28.9±1.5
0.95	20.6±1.8	19.0±2.2	22.7±1.3	24.7±1.3	24.5±1.2
1.05	18.4±1.4	18.6±1.6	19.6±1.0	21.7±1.1	21.5±1.1
1.15	18.7±1.3	16.0±1.2	16.6±1.0	19.1±1.0	18.3±0.9
1.25	10.9±0.9	12.5±1.1	14.3±0.8	15.4±0.8	15.2±0.8
1.35	9.57±0.80	12.8±0.9	10.9±0.6	12.2±1.0	11.6±0.6
1.45	9.32±1.02	8.45±0.81	8.41±0.51	9.02±0.57	9.77±0.50
1.55	6.78±0.64	6.64±0.62	7.37±0.42	7.11±0.46	7.43±0.37
1.65	5.40±0.51	6.87±0.57	5.16±0.32	5.27±0.36	4.84±0.36
1.75	3.95±0.39	4.33±0.39	3.50±0.21	3.59±0.33	4.27±0.29
1.85	2.31±0.28	3.01±0.24	2.35±0.23	2.60±0.20	2.86±0.23
1.95	1.84±0.19	2.26±0.19	2.38±0.16	1.96±0.13	2.23±0.18
2.05	1.46±0.18	1.25±0.11	1.91±0.12	1.38±0.08	1.71±0.15
2.15	0.85±0.14	1.28±0.10	1.01±0.07	1.06±0.07	1.15±0.11
2.25	0.75±0.09	0.91±0.08	0.74±0.06	0.69±0.05	0.89±0.10
2.35	0.62±0.10	0.54±0.05	0.72±0.06	0.59±0.05	0.63±0.08
2.45	0.74±0.12	0.46±0.05	0.38±0.04	0.44±0.03	0.55±0.10

Table C.2: Net proton $d^2n/dydp_T$ from the rapidity range $3.0 < y < 4.0$.

$p_T \pm 0.05$ GeV/c	$4.0 < y < 4.2$	$4.2 < y < 4.4$	$4.4 < y < 4.6$	$4.6 < y < 4.8$	$4.8 < y < 5.0$
0.05	4.52±0.62	4.50±0.91	4.74±1.01	3.72±0.31	3.45±0.34
0.15	14.6±1.6	14.2±2.1	15.2±1.7	10.8±0.8	11.5±0.9
0.25	22.6±2.5	22.9±3.8	22.1±2.0	20.0±1.2	17.4±1.0
0.35	30.1±3.2	30.7±5.3	27.4±2.2	23.7±1.2	23.4±1.3
0.45	32.7±2.4	34.6±3.6	32.6±2.1	29.0±1.6	28.7±1.5
0.55	35.1±3.0	35.0±3.1	32.7±1.5	29.1±1.4	28.9±1.4
0.65	34.6±2.6	32.4±2.5	32.7±1.6	31.5±1.4	27.3±1.4
0.75	32.2±2.1	32.2±1.5	31.5±1.5	29.7±1.3	23.0±1.3
0.85	27.9±1.6	29.0±1.4	29.1±1.2	25.7±1.2	19.9±1.0
0.95	25.1±1.1	24.8±1.2	24.0±1.1	21.7±1.1	16.9±0.9
1.05	21.3±1.0	23.0±1.0	20.2±0.9	16.8±0.8	12.1±0.6
1.15	18.2±0.9	17.2±0.8	16.5±0.7	12.8±0.6	10.1±0.6
1.25	15.6±0.9	13.8±0.6	11.5±0.5	9.64±0.47	7.92±0.44
1.35	10.9±0.60	11.0±0.5	9.00±0.48	6.68±0.35	5.01±0.27
1.45	8.40±0.39	8.06±0.38	6.58±0.34	4.98±0.25	3.84±0.23
1.55	7.01±0.37	6.12±0.31	4.73±0.25	3.67±0.21	2.83±0.18
1.65	5.26±0.28	4.30±0.24	3.14±0.20	2.75±0.15	1.65±0.13
1.75	3.83±0.27	3.50±0.17	2.24±0.15	1.71±0.11	1.34±0.10
1.85	2.79±0.22	2.27±0.13	1.65±0.13	1.22±0.11	0.75±0.08
1.95	2.29±0.15	1.66±0.09	1.19±0.10	1.01±0.12	0.65±0.09
2.05	1.37±0.10	1.12±0.07	0.80±0.07	0.74±0.06	0.47±0.09
2.15	1.15±0.09	0.92±0.06	0.65±0.11	0.48±0.04	0.48±0.06
2.25	0.76±0.07	0.54±0.05	0.42±0.03	0.26±0.06	0.24±0.09
2.35	0.54±0.05	0.44±0.05	0.38±0.04	0.26±0.04	0.18±0.07
2.45	0.39±0.05	0.49±0.08	0.30±0.04	0.35±0.03	0.36±0.05

Table C.3: Net proton $d^2n/dydp_T$ from the rapidity range $4.0 < y < 5.0$.

$p_T \pm 0.05$ GeV/c	$5.0 < y < 5.2$	$5.2 < y < 5.4$
0.05	3.38±0.24	4.13±0.64
0.15	10.0±0.7	10.8±1.0
0.25	16.4±1.0	14.1±1.1
0.35	22.1±1.3	26.1±2.0
0.45	23.3±1.2	20.6±1.5
0.55	23.9±1.3	21.7±1.6
0.65	19.1±0.9	21.9±1.7
0.75	17.6±0.9	15.9±1.3
0.85	15.8±0.9	14.3±1.3
0.95	12.9±0.7	11.4±1.2
1.05	8.60±0.54	8.23±1.04
1.15	6.00±0.39	5.36±0.71
1.25	4.74±0.35	4.62±0.78
1.35	3.32±0.23	1.97±0.47
1.45	2.51±0.21	0
1.55	1.62±0.16	0
1.65	1.13±0.10	0
1.75	0.67±0.11	0
1.85	0.69±0.10	0
1.95	0.35±0.05	0
2.05	0	0
2.15	0	0
2.25	0	0
2.35	0	0
2.45	0	0

Table C.4: Net proton $d^2n/dydp_T$ from the rapidity range $5.0 < y < 5.4$.

rapidity	net proton dn/dy	net baryon dn/dy
$2.2 < y < 2.4$	31.1±5.3	76.9±11.0
$2.4 < y < 2.6$	28.3±4.4	71.0±9.0
$2.6 < y < 2.8$	27.8±4.0	69.9±8.3
$2.8 < y < 3.0$	26.6±3.7	67.6±7.5
$3.0 < y < 3.2$	28.8±3.3	72.1±6.7
$3.2 < y < 3.4$	30.8±2.8	76.3±5.8
$3.4 < y < 3.6$	32.0±2.2	78.8±4.5
$3.6 < y < 3.8$	34.6±1.9	84.1±4.0
$3.8 < y < 4.0$	34.9±1.6	84.2±3.3
$4.0 < y < 4.2$	35.9±1.6	85.6±3.4
$4.2 < y < 4.4$	35.5±1.9	83.3±4.0
$4.4 < y < 4.6$	33.1±1.6	76.9±3.3
$4.6 < y < 4.8$	28.8±1.3	66.2±2.6
$4.8 < y < 5.0$	24.8±1.5	56.1±3.0
$5.0 < y < 5.2$	19.4±1.2	43.1±2.5
$5.2 < y < 5.4$	18.1±2.7	39.0±5.6

Table C.5: Rapidity densities dn/dy of net protons and net baryons.

$p_T \pm 0.025$ (GeV/c)	$3.7 < y < 3.9$	$3.9 < y < 4.1$	$4.1 < y < 4.3$	$4.3 < y < 4.5$
0.025	0	97.5±7.1	95.2±6.0	90.1±5.5
0.075	260±32	233±14	224±13	206±12
0.125	319±24	321±19	274±16	255±15
0.175	325±21	309±17	286±16	277±16
0.225	313±21	305±18	275±16	249±14
0.275	289±19	255±14	254±15	228±13
0.325	239±15	240±14	220±12	193±11
0.375	219±13	204±11	180±10	164±8
0.425	182±11	184±10	155±9	136±7
0.475	149±8.5	143±7.8	128±7	116±6
0.525	132±7.8	122±6.6	115±6	91.9±5.2
0.575	113±6.8	105±5.5	96.7±4.7	75.3±4.2
0.625	100±5.9	86.6±4.6	79.1±4.0	68.1±3.9
0.675	85.5±5.3	73.0±3.6	68.3±3.6	59.5±3.2
0.725	64.1±3.7	62.5±2.9	50.9±2.7	44.6±2.5
0.775	53.5±3.0	51.5±2.4	47.0±2.6	38.6±2.1
0.825	49.7±2.9	47.4±2.4	38.0±2.2	32.3±1.8
0.875	43.7±2.4	35.1±1.8	30.9±1.7	20.6±1.1
0.925	35.3±1.9	33.7±1.7	27.2±1.5	20.9±1.2
0.975	27.3±1.4	27.1±1.5	23.1±1.3	18.8±1.1
1.025	26.7±1.4	21.8±1.2	18.6±1.0	5.30±0.30
1.075	21.5±1.1	18.8±1.0	15.9±0.94	12.3±0.67
1.125	18.3±0.92	14.1±0.77	12.8±0.72	9.35±0.52
1.175	15.2±0.77	13.8±0.80	11.3±0.63	8.01±0.43
1.225	11.1±0.56	9.79±0.54	8.13±0.47	7.78±0.45
1.275	9.77±0.49	9.38±0.51	7.70±0.44	5.39±0.30
1.325	8.86±0.43	6.27±0.35	7.04±0.39	4.56±0.24
1.375	7.04±0.35	6.80±0.39	4.90±0.27	3.23±0.18
1.425	5.59±0.27	4.41±0.26	3.66±0.21	2.91±0.17
1.475	5.12±0.26	4.36±0.24	2.67±0.14	2.64±0.16
1.525	4.18±0.22	3.84±0.21	2.86±0.16	2.16±0.12
1.575	3.63±0.18	2.15±0.12	2.76±0.15	1.66±0.10
1.625	2.67±0.14	2.95±0.15	1.69±0.10	1.27±0.08
1.675	2.70±0.15	2.24±0.12	1.48±0.08	1.06±0.06
1.725	1.88±0.11	1.82±0.11	1.11±0.07	0.88±0.06
1.775	1.80±0.10	1.51±0.08	1.09±0.06	0.92±0.05
1.825	1.38±0.08	1.11±0.06	1.32±0.08	0.88±0.06
1.875	1.30±0.08	1.21±0.07	1.25±0.08	0.49±0.03
1.925	1.63±0.10	1.20±0.07	0.70±0.04	0.58±0.03
1.975	1.84±0.10	0.48±0.03	0.41±0.03	0.36±0.02
2.025	0.88±0.05	0.69±0.04	0.45±0.03	0.23±0.02
2.075	0.66±0.04	0.75±0.04	0.43±0.03	0.65±0.04
2.125	1.21±0.08	0.41±0.02	0.53±0.03	0.49±0.03
2.175	0.48±0.03	0.57±0.03	0.35±0.02	0.27±0.02
2.225	1.00±0.06	0.51±0.03	0.17±0.04	0.36±0.02
2.275	0.61±0.04	0.44±0.03	0.42±0.02	0.42±0.02
2.325	0.86±0.05	0.55±0.03	0.35±0.02	0.24±0.03
2.375	0.66±0.04	0.50±0.03	0.31±0.02	0.16±0.01
2.425	0.47±0.02	0.21±0.01	0.29±0.02	0.12±0.01
2.475	0.46±0.03	0.50±0.03	0.27±0.02	0.17±0.01

Table C.6: Negative charge hadron $d^2n/dydp_T$ from the rapidity interval $3.7 < y < 4.5$.

$p_T \pm 0.025$ (GeV/c)	$4.5 < y < 4.7$	$4.7 < y < 4.9$	$4.9 < y < 5.1$	$5.1 < y < 5.3$
0.025	76.9±4.8	65.9±3.8	59.4±3.4	48.9±3.0
0.075	192±11	163±9	133±9	109±6
0.125	221±12	200±12	178±10	137±7
0.175	252±14	201±11	164±8	139±8
0.225	209±11	175±8	152±8	120±7
0.275	196±10	161±8	131±8	97.3±5.3
0.325	157±8	132±8	100±6	87.0±4.8
0.375	145±8	116±7	84.0±4.7	65.6±3.7
0.425	108±6	90.5±4.9	68.3±3.7	50.8±2.7
0.475	96.5±5.4	75.1±4.2	57.2±3.2	41.1±2.2
0.525	75.2±4.2	65.1±3.6	50.2±2.8	31.4±1.7
0.575	66.8±4.0	48.9±2.7	33.7±1.9	25.1±1.4
0.625	53.0±3.0	44.8±2.4	31.7±1.7	21.7±1.2
0.675	44.8±2.6	36.2±2.0	25.0±1.4	14.5±0.80
0.725	38.8±2.2	25.6±1.4	18.7±1.0	11.2±0.62
0.775	27.9±1.5	20.9±1.1	14.5±0.84	8.77±0.49
0.825	22.9±1.2	18.7±1.1	12.3±0.70	7.87±0.42
0.875	20.2±1.2	14.2±0.78	7.91±0.47	4.82±0.27
0.925	16.3±0.9	11.2±0.63	7.90±0.46	5.71±0.33
0.975	13.5±0.8	9.62±0.54	6.42±0.36	3.17±0.19
1.025	10.6±0.6	6.83±0.37	3.11±0.18	2.93±0.17
1.075	7.73±0.44	4.80±0.27	4.43±0.26	1.89±0.12
1.125	7.17±0.42	3.89±0.21	3.32±0.19	1.71±0.11
1.175	5.74±0.32	4.14±0.24	2.69±0.17	0.91±0.07
1.225	4.50±0.26	2.43±0.14	1.69±0.10	0.71±0.05
1.275	3.82±0.21	2.40±0.13	1.56±0.09	0.12±0.01
1.325	3.07±0.18	2.23±0.13	0.62±0.04	0.61±0.043
1.375	2.83±0.16	2.05±0.12	1.21±0.08	0.65±0.057
1.425	1.37±0.08	1.50±0.09	0.72±0.05	0.10±0.008
1.475	1.53±0.10	1.46±0.09	0.73±0.05	0.29±0.027
1.525	1.59±0.09	1.40±0.09	0.49±0.03	0.01±0.001
1.575	1.41±0.08	0.46±0.03	0.82±0.05	0.21±0.020
1.625	1.04±0.06	0.55±0.03	0.51±0.04	0.41±0.035
1.675	0.96±0.06	0.62±0.04	0.44±0.04	0.001±0.001
1.725	0.81±0.05	0.39±0.03	0.61±0.04	0.22±0.023
1.775	0.38±0.03	0.43±0.03	0.10±0.01	0.064±0.006
1.825	0.55±0.03	0.26±0.02	0.31±0.02	0.052±0.001
1.875	0.27±0.02	0.37±0.03	0.04±0.01	0.045±0.004
1.925	0.53±0.04	0.24±0.02	0.18±0.01	0.48±0.055
1.975	0.36±0.02	0.17±0.01	0.03±0.003	0.005±0.001
2.025	0.43±0.03	0.17±0.01	0.05±0.004	0.017±0.002
2.075	0.19±0.02	0.36±0.03	0.03±0.003	0.001±0.001
2.125	0.32±0.02	0.13±0.01	0.08±0.007	0.043±0.009
2.175	0.18±0.01	0.20±0.02	0.11±0.01	
2.225	0.29±0.02	0.22±0.03	0.01±0.001	
2.275	0.13±0.01	0.07±0.01	0.39±0.035	
2.325	0.28±0.02	0.10±0.01	0.24±0.02	
2.375	0.15±0.01	0.18±0.01	0.10±0.012	
2.425	0.11±0.01	0.07±0.01	0.01±0.001	
2.475	0.10±0.01	0.20±0.01	0.05±0.004	

Table C.7: Negative charge hadron $d^2n/dydp_T$ from the rapidity interval $4.5 < y < 5.3$.

$p_T \pm 0.025$ (GeV/c)	$5.3 < y < 5.5$	$5.5 < y < 5.7$	$5.7 < y < 5.9$	$5.9 < y < 6.1$
0.025	37.1±2.0	32.3±2.0	22.5±1.4	17.1±1.03
0.075	88.0±4.5	69.7±4.0	56.1±3.1	37.8±2.20
0.125	113±6.6	94.0±5.5	63.9±3.6	44.7±2.43
0.175	107±5.7	81.5±4.5	57.3±3.26	38.5±2.13
0.225	93.1±5.2	67.4±3.8	42.4±2.33	26.6±1.49
0.275	67.8±3.8	52.1±2.9	32.5±1.79	19.0±1.05
0.325	59.3±3.3	40.2±2.2	26.5±1.57	14.9±0.91
0.375	42.4±2.3	27.0±1.5	17.7±0.98	9.39±0.52
0.425	37.8±2.2	24.9±1.3	13.8±0.76	7.92±0.52
0.475	28.3±1.5	17.5±1.1	10.6±0.61	4.70±0.34
0.525	20.5±1.1	11.8±0.69	6.90±0.44	3.01±0.30
0.575	18.5±1.0	9.22±0.53	4.66±0.33	2.23±0.47
0.625	13.1±0.74	7.63±0.44	3.42±0.27	2.39±1.07
0.675	8.17±0.44	4.74±0.28	1.12±0.12	
0.725	6.68±0.40	4.48±0.28	0.83±0.11	
0.775	4.89±0.29	3.09±0.24	1.76±0.32	
0.825	3.56±0.22	1.13±0.08	0.40±0.14	
0.875	3.75±0.24	0.92±0.08		
0.925	1.37±0.09	0.48±0.05		
0.975	2.01±0.14	0.87±0.13		
1.025	1.54±0.12	0.23±0.03		
1.075	1.66±0.13	0.46±0.11		
1.125	0.13±0.01			
1.175	0.54±0.05			
1.225	0.18±0.03			
1.275	0.03±0.01			
1.325	0.28±0.03			
1.375	0.44±0.05			
1.425	0.18±0.03			
1.475	0.96±0.15			

Table C.8: Negative charge hadron $d^2n/dydp_T$ from the rapidity interval $5.3 < y < 6.1$.

$p_T \pm 0.025$ (GeV/c)	$6.1 < y < 6.3$	$6.3 < y < 6.5$	$6.5 < y < 6.7$	$6.7 < y < 6.9$
0.025	12.4±0.80	7.83±0.50	5.98±0.38	3.95±0.27
0.075	28.6±1.63	18.6±1.1	11.5±0.66	6.56±0.40
0.125	32.5±1.87	19.6±1.1	10.9±0.62	5.06±0.35
0.175	22.9±1.31	14.4±0.79	7.29±0.46	3.23±0.49
0.225	16.5±0.94	9.26±0.52	7.32±0.71	
0.275	12.4±0.73	5.15±0.37	10.8±7.6	
0.325	7.79±0.49	3.06±0.44		
0.375	4.37±0.33			
0.425	3.93±0.66			
0.475	1.48±0.71			

Table C.9: Negative charge hadron $d^2n/dydp_T$ from the rapidity interval $6.1 < y < 6.9$.

rapidity	$STD\ dn/dy$	$HBT\ dn/dy$
$2.9 < y < 3.1$		196±10
$3.1 < y < 3.3$		191±7
$3.3 < y < 3.5$		191±5
$3.5 < y < 3.7$		178±4
$3.7 < y < 3.9$	163±3	167±3
$2.9 < y < 3.1$	153±3	159±4
$3.1 < y < 3.3$	139±2	143±3
$3.3 < y < 3.5$	123±2	128±3
$3.5 < y < 3.7$	105±2	108±3
$3.7 < y < 3.9$	85.6±1.4	90.9±2
$2.9 < y < 3.1$	68.0±1.1	
$3.1 < y < 3.3$	52.0±0.9	
$3.3 < y < 3.5$	38.3±0.7	
$3.5 < y < 3.7$	27.6±0.5	
$3.7 < y < 3.9$	18.1±0.4	
$2.9 < y < 3.1$	11.4±0.2	
$3.1 < y < 3.3$	7.14±0.17	
$3.3 < y < 3.5$	3.91±0.10	
$3.5 < y < 3.7$	2.70±0.04	
$3.7 < y < 3.9$	0.95±0.04	

Table C.10: Negative charge hadron rapidity density dn/dy from STD (this analysis) and HBT [101] magnet setting data.

Bibliography

[1] J.I. Friedman and H.W. Kendall, Ann. Rev. Nucl. Sci. **22**, 203 (1972).

[2] J.B. Kogut, Rev. Mod. Phys. **55**, 775 (1983).

[3] H. Meyer-Ortmanns, Rev. Mod. Phys. **68**, 473 (1996).

[4] F.R. Brown, H. Chen, N.H. Christ, Z. Dong, R.D. Mawhinney, W. Schaffer, and A. Vaccarino, Phys. Rev. D **46**, 5655 (1992).

[5] L. van Hove, Phys. Lett. **118B**, 138 (1982).

[6] S. Weinberg, *The First Three Minutes*, Basic Books, N.Y. (1977).

[7] N.K. Glendenning, S. Pei, and F. Weber, Phys. Rev. Lett. **79**, 1603 (1997).

[8] T. Matsui, Nucl. Phys. **A638**, 19 (1998).

[9] W. Reisdorf and H.G. Ritter, Ann. Rev. Nucl. Part. Sci. **47**, 663 (1997).

[10] H. Appelshäuser *et al.*, Phys. Rev. Lett. **80**, 4136 (1998).

[11] *Proceedings of Quark Matter '97*, Nucl. Phys. **A638** (1998).

[12] *Proceedings of Quark Matter '96*, Nucl. Phys. **A610** (1996).

[13] *Proceedings of Quark Matter '95*, Nucl. Phys. **A590** (1995).

[14] U. Heinz and B. Jacak, CERN-TH-99-26 (1999).

[15] H. Satz, *LHC Workshop Proccedings*, 188 (1990).

[16] H. Appelshäuser *et al.*, Phys. Rev. Lett. **82**, 2471 (1999).

[17] L. Ahle *et al.*, Nucl. Phys. A **610**, 139c (1996)

[18] B. Müller, Nucl. Phys. **A544** 95 (1992).

[19] J. Rafelski and B. Müller, Phys. Rev. Lett. **48**, 1066 (1982).

[20] J. Rafelski and B. Müller, Phys. Rev. Lett. **56**, 2324 (1986).

[21] G. Odyniec, Nucl. Phys. **A638** 135 (1998).

[22] L. Ramello, Nucl. Phys. **A638** 261 (1998).

[23] S. Pratt, Nucl. Phys. **A638** 125 (1998).

[24] I. Tserruya, Nucl. Phys. **A638** 365 (1998).

[25] M. Gaździcki, A. Leonidov, and G. Roland, Eur. Phys. J. C **6** 365 (1999).

[26] B. Wyslouch *et al.*, Nucl. Phys. **A638** 147 (1998).

[27] K.S. Lee, U. Heinz, and E. Schnedermann, Z. Phys. C **48**, 525 (1990).

[28] S. Chapman, P. Scotto, and U. Heinz, Heavy Ion Physics **1**, 1 (1995).

[29] T. Alber *et al.*, Eur. Phys. J. **C2**, 643 (1998).

[30] J. Bächler *et al.*, Phys. Rev. Lett. **72**, 1419 (1994)

[31] T. Alber *et al.*, Z. Phys. C **64**, 195 (1994).

[32] L.P. Teitelbaum, Ph.D. Thesis, University of California (1992); LBL Report 32812 (1992).

[33] D. Barton *et al.*, Phys. Rev. D **27**, 2580 (1983).

[34] M. Aguilar-Benitez *et al.*, Z. Phys. C **50**, 405 (1991).

[35] W. Busza and R. Ledoux, Ann. Rev. Nucl. Part. Sci. **38**, 119 (1988).

[36] C. Geich-Gimbel, Int. J. Mod. Phys. **A4**, 1527 (1989).

[37] C. DeMarzo *et al.*, Phys. Rev. D **26**, 1019 (1982).

[38] C. DeMarzo *et al.*, Phys. Rev. D **29**, 2476 (1984).

[39] D.H. Brick *et al.*, Phys. Rev. D **39**, 2484 (1989).

[40] D.H. Brick *et al.*, Phys. Rev. D **41**, 765 (1990).

[41] A. Białas and W. Czyż, Phys. Lett. B **51**, 179 (1974).

[42] W. Busza and A. Goldhaber, Phys. Lett. **139B**, 235 (1984).

[43] L.D. Landau, Ivz. Akad. Nauk. Ser. Phys. **17**, 51 (1953).

[44] T. Wienold, EOS Collaboration, private communication.

[45] J. Stachel and P. Braun-Munzinger, Phys. Lett. **B216**, 1 (1989).

[46] J. Stachel and P. Braun-Munzinger, Nucl. Phys. A **498**, 577 (1989).

[47] B. Andersson, G. Gustafson, and H. Pi, Z. Phys. C **57**, 485 (1993).

[48] K. Werner, Phys. Rep. **232**, 87 (1993).

[49] H. Sorge, Phys. Rev. C **52**, 3291 (1995).

[50] A. Capella *et al.*, Phys. Rep. **236**, 225 (1994).

[51] E. Schnedermann, J. Sollfrank, and U. Heinz, Phys. Rev. C **48**, 2462 (1993).

[52] E. Schnedermann and U. Heinz, Phys. Rev. C **50**, 1675 (1994).

[53] S. Chapman and J.R. Nix, report LA-UR-96-0782 (1996).

[54] B. Schlei, report LA-UR-97-2162 (1997).

[55] T. Alber *et al.* (NA49 Collaboration), Eur. Phys. J. **C2**, 643 (1998).

[56] J.D. Bjorken, Phys. Rev. D **27**, 140 (1983).

[57] S.A. Bass, M. Gyulassy, H. Stöcker, and W. Greiner, hep-ph/9810281 (1998).

[58] G.C. Rossi and G. Veneziano, Nucl. Phys. **B123**, 507 (1977)

[59] D. Kharzeev, Phys. Lett. **B378**, 238 (1996).

[60] A. Capella, B.Z. Kopeliovich, Phys. Lett. **B381**, 325 (1996)

[61] M. Gyulassy, V.T. Pop, and S.E. Vance, Heavy Ion Physics **5**, 299 (1997).

[62] A. Capella and C.A. Salgado, hep-ph/9903414 (1999).

[63] T. Alber *et al.*, Nucl. Instr. Meth. A **430**, 210 (1999).

[64] A.R. Clark *et al.*, PEP-PROPOSAL-004, (1976).

[65] F. Sauli, CERN Report 77-09.

[66] S. Margetis *et al.*, Phys. Rev. Lett. **75**, 3814 (1995)

[67] S. Margetis, private communication.

[68] I. Huang, Ph.D. Thesis, University of California, Davis (1997)

[69] S. Wenig *et al.*, Nucl. Instr. Meth. A **409**, 100 (1998).

[70] T. Alber, Diploma Thesis, Technische Universität München (1992).

[71] T. Alber *et al.*, Nucl. Instr. and Meth. **A349**, 56 (1994)

[72] W. Blum and L. Rolandi, *Particle Detection with Drift Chambers*, Springer Verlag (1994).

[73] F. Bieser *et al.*, Nucl. Instr. Meth. A **385**, 535 (1997).

[74] W. Rauch *et al.*, IEEE Trans. Nucl. Sci. **41** 30 (1994).

[75] W. Leo, *Techniques for Nuclear and Particle Physics Experiments*, Springer Verlag (1994).

[76] W. Allison and P. Wright, *Experimental Techniques in High Energy Physics*, ed. T. Ferbel, Addison-Wesley (1987).

[77] A. Mock, Ph.D. Thesis, Max-Planck-Institut für Physik, München, Germany (1997)

[78] B. Lasiuk *et al.*, Nucl. Instr. Meth. A **409**, 402 (1998).

[79] J. Marx, PEP Conference, Stanford (1976).

[80] D.L. Fancher and A.C. Schaffer, IEEE Trans. Nucl. Sci., **NS-26**, 150 (1979)

[81] D.L. Fancher *et al.*, Nucl. Instr. Meth. **161**, 383 (1979)

[82] D. Decamp *et al.*, Nucl. Instr. Meth. A **294**, 121 (1990).

[83] *The ALEPH Handbook Vols. 1 and 2*, CERN (1995, 1997).

[84] H. Wieman *et al.*, Nucl. Phys. **A638**, 559 (1998).

[85] *Conceptual Design Of The Relativisitic Heavy Ion Collider*, BNL-52195-mc (1989).

[86] S. Margetis *et al.*, to appear in *Proceedings of Strange Quark Matter 1998.*

[87] I. Králik *et al.*, Nucl. Phys. **A638**, 115 (1998).

[88] H. Appelshaeuser *et al.*, Eur. Phys. J. **A2**, 383 (1998).

[89] C. Bormann, Ph.D. Thesis, Fachbereich Physik der Universität, Frankfurt, Germany (1998).

[90] J. Grebieszkow, Ph.D. Thesis, University of Warsaw, Warsaw, Poland (1999).

[91] T. Yates, Ph.D. Thesis, Birmingham University, Birmingham, England (1998).

[92] S.E. Eiseman *et al.*, Nucl. Phys. **A590**, 477 (1995).

[93] A. Wróblewski, Acta Phys. Pol. B **16**, 379 (1985).

[94] C. Bormann *et al.*, J. Phys. G **23**, 1817 (1997).

[95] M. Gaździcki and D. Rörich, Z. Phys. C **71**, 55 (1996).

[96] J. Günther *et al.*, Phys. Lett. B **366**, 56 (1996).

[97] I.G. Bearden *et al.*, Phys. Rev. Lett. **78**, 2080 (1997).

[98] F. Pülhofer *et al.*, Nucl. Phys. **A638**, 431 (1998).

[99] G. Cooper *et al.*, Advances in Nuclear Dynamics 3, 123 (1997).

[100] I.G. Bearden *et al.*, Nucl. Phys. A **610**, 175 (1996).

[101] P. Seyboth, MPI Munich, private communication.

[102] A.E. Brenner *et al.*, Phys. Rev. **D26**, 1497 (1982).

[103] M. Gázdzicki and O. Hansen, Nucl. Phys. **A528**, 754 (1991).

[104] A. Białas, M. Błeszyński, and W. Czyż, Nucl. Phys. B **111**, 461 (1976).

[105] T Åkesson *et al.*, Phys. Lett. **119B**, 464 (1982).

[106] T Åkesson *et al.*, Phys. Lett. **B231**, 359 (1989).

[107] H. Beker *et al.*, Phys. Lett. **B302**, 510 (1993).

[108] N. Xu, LBNL, private communication.

[109] J.W. Cronin *et al.*, Phys. Rev. **D11**, 3105 (1975).

[110] J. Simon-Gillo, Nucl. Phys. A**566**, 175 (1994).

[111] GEANT, Detector Description and Simulation Tool, CERN Program Library Long Writeup W5013

[112] EOS Collaboration, simulation documentation.

[113] R. Bossingham *et al.*, STAR Offline Simulations and Analysis Software Design (STAR Note 0281).

[114] P. Jacobs, NA49 Note.

[115] J.E. Moyal, Phil. Mag. **46**, 263 (1955)

[116] P. Jones and G. Rai, STAR Notes 33 and 34.